UC Santa Barbara

UC Santa Barbara Electronic Theses and Dissertations

Title

Cooperative Orders in Complex Oxide Heterostructures

Permalink

https://escholarship.org/uc/item/28f1n9gq

Author

Ahadi, Kaveh

Publication Date

2019

Peer reviewed|Thesis/dissertation

eScholarship.org Powered by the California Digital Library
University of California

UNIVERSITY OF CALIFORNIA

Santa Barbara

Cooperative Orders in Complex Oxide Heterostructures

A dissertation submitted in partial satisfaction of the

requirements for the degree of

Doctor of Philosophy

in

Materials

by

Kaveh Ahadi

Committee in charge:

Professor Susanne Stemmer, Chair

Professor Leon Balents

Professor Stephen D. Wilson

Professor John W. Harter

December 2019

The dissertation of Kaveh Ahadi is approved.

Leon Balents

John W. Harter

Stephen D. Wilson

Susanne Stemmer, Committee Chair

November 2019

Cooperative Orders in Complex Oxide Heterostructures

Copyright © 2019

by

Kaveh Ahadi

Daher ist die Aufgabe nicht sowohl, zu sehen was noch keiner gesehen hat, als bei dem was jeder sieht, zu denken was noch keiner gedacht hat.

—Arthur Schopenhauer

Research is to see what everybody else has seen, and to think what nobody else has thought.

—Albert Szent-györgi

Acknowledgements

I would like to extend my appreciation and gratitude to the many people who have helped me see what everybody else has seen and think of what nobody else has thought. First, I would like to thank my advisor Susanne for the guidance, instruction, and support throughout my PhD program. Her passion for science and research has been inspirational. Additionally, she has taught me how to think, write and ask questions like a scientist. I would also like to extend my gratitude to the members of my doctoral committee: John Harter, Stephen Wilson, and Leon Balents. Their scientific insight during examinations and meetings has been immensely helpful in shaping the work in this thesis.

Collaboration with Stephen Wilson and his student Zach Porter greatly added to our understanding of the nature of magnetism in the $EuTiO_3$. Collaboration with John Harter and his students Ryan Russel and Noah Ratcliff and David Hsieh and his post doc Alon Ron helped elucidating the nature of the ferroelectricity in doped $SrTiO_3$. I also would like to extend my gratitude towards James Rondinelli and his student Xuezeng Lu and Anderson Janotti and his post doc Zhigang Gui for DFT calculations of the band structure of $EuTiO_3$. Their theoretical insight helped shedding light on topologically nontrivial nature of band structure in doped $EuTiO_3$.

In no particular order, I am also thankful for discussions with B. Jalan, J. LeBeau, R. Need, H. Hwang, J. Zaanen, G. Lonzarich, K. Behnia, D. Maslov, C. Rischau, N. Awdhesh, M. Navarro, B. Shklovskii, H. Fu, H. Nair, D. Muller, J. Analytis, R. Averitt, G. Khalsa, J. Levy, J. Allen, N. Spaldin, and R. Seshadri.

I want to extend my gratitude to past and present members of Stemmer group for their support and friendship: Patrick, Santosh, Timo, Nick, Manik, Hanbyeol, Pouya, Tyler, Omor, Luca, Yuntian, Billy, Wangzhou, Raj, Gift, Brandon, Alex, Evan, Chris, Omor, Evgeny, Jack, Honggyu, David, and Salva. I would like to acknowledge Patrick for close collaboration on the correlated oxide projects, Evgeny for metal-insulator transition studies, Luca, Yuntian, Timo and Hanbyeol for superconductivity research, Omor for device fabrication and analysis, and Salva and Honggyu for microscopy efforts.

I would like to thank the MBE lab. engineers, John English and Kurt Olsson, for their technical helps and invaluable aid in the maintenance of our MBE system. I would also like to acknowledge the staff of the UCSB Nanofabrication Facility, Amanda Strom for managing the TEMPO facilities in the MRL, Youli Li for managing the x-ray characterization facilities, Joanne McNie for her assistance in the complicated reimbursement paperwork, and Jocelyn Guzman for her assistance with the bureaucracy of the graduate study.

I'd like to thank my friends and family, specifically my mom, dad, and brothers for their encouragement and support throughout my PhD program. Finally, I must thank my wonderful wife Salva, as without her support I may never completed this program.

KAVEH AHADI
Santa Barbara, CA

Curriculum Vitæ

Kaveh Ahadi

Education

2016-2019	PhD in materials, University of California, Santa Barbara, USA
2013-2015	M.Sc in materials, University of Alberta, Edmonton, Canada
2008-2010	M.Sc in ceramics, Sharif University of Technology, Tehran, Iran
2004-2008	B.Sc in materials, Azad University, Karaj, Iran

Selected Honors

- DCMP student travel award, APS march meeting, Boston (2019)
- Ovshinsky student travel award, APS march meeting, Los Angeles (2018)
- Outstanding poster, fourth annual FAME research review, Los Angeles (2017)
- Alberta Innovate Technology Future Scholarship, Edmonton, Canada (2014-2015)

Selected Publications

- **K. Ahadi**, L. Galletti, Y. Li, S. Salmani-Rezaie, W. Wu, S. Stemmer, enhancing superconductivity with strain in $SrTiO_3$, Sci. Adv., **5** 120 (2019) [DOI]
- **K. Ahadi**, X. Lu, S. Salmani-Rezaie, P.B. Marshall, J.M. Rondinelli, S. Stemmer, Anisotropic magnetoresistance in itinerant, antiferromagnetic $EuTiO_3$, Phys. Rev. B. **99**, 041106(R) (2019) [DOI]
- **K. Ahadi**, Z. Gui, Z. Porter, J.W. Lynn, Z. Xu, S.D. Wilson, A. Janotti, S. Stemmer, Carrier density control of magnetism and Berry phases in doped $EuTiO_3$, APL Mater. **6** 056105 (2018) [DOI]

- **K. Ahadi**, H. Kim, S. Stemmer, Spontaneous Hall effects in the electron systems at the $SmTiO_3$/ $EuTiO_3$ interface, APL Mater. **6** 056102 (2018) [DOI]
- **K. Ahadi**, L. Galletti, S. Stemmer, Evidence of a topological Hall effect in $Eu_{1-x}Sm_xTiO_3$, App. Phys. Lett. **111** 172403 (2017) [DOI]
- **K. Ahadi** and S. Stemmer, Novel metal-insulator transition at the $SmTiO_3$/ $SrTiO_3$ interface, Phys. Rev. Lett. **118** 236803 (2017) [DOI]
- **K. Ahadi**, O.F. Shoron, P.B. Marshall, E. Mikheev, S. Stemmer, Electric field near the metal-insulator transition of a two-dimensional electron system in $SrTiO_3$, App. Phys. Lett. **110** 062104 (2017) [DOI]
- **K. Ahadi**, K.C. Cadien, Ultra-low density of interfacial defects with mixed thermal and plasma enhanced ALD of high-κ gate dielectrics, RSC Adv. **6** 16301 (2016) [DOI]
- **K. Ahadi**, A. Nemati, S.-M. Mahdavi, A. Vaezi, Effect of simultaneous chemical substitution of A and B sites on the electrical properties and electronic structure of $BiFeO_3$ films, J. Mater. Sci. Mater. Electron. **24** 2128 (2013) [DOI]

Selected Oral Presentations

- Unusual superconducting states in $SrTiO_3$, Geballe Laboratory for Advanced Materials (GLAM) Special Seminar, Stanford University (2019)
- Anisotropic magnetoresistance and anomalous Hall effect in $EuTiO_3$, MRS spring, Phoenix (2019)
- Magnetic field control of Fermi surface topology in $EuTiO_3$, APS march meeting, Boston (2019)
- Topological Hall effect and itinerant metamagnetism in $EuTiO_3$, MRS spring meeting, Phoenix (2018)
- Non-Fermi liquid behavior and topological Hall effect in $SrRuO_3$, APS march meeting, Los Angeles (2018)
- Novel metal-insulator transition at the $SmTiO_3$/$SrTiO_3$ interface, MRS fall meeting, Boston (2017)

Abstract

Cooperative Orders in Complex Oxide Heterostructures

by

Kaveh Ahadi

Perovskite materials, having the simple ABO_3 chemical formula, show a wide variety of electronic properties depending on the choice of the A and/or B cations. Multiple orders (e.g. electronic, magnetic and structural) with similar energy scales frequently occur in a single perovskite material. Cooperation between neighboring orders is believed to enhance the existing orders or, more excitingly, give rise to new phenomena.

$SrTiO_3$ is the first oxide superconductor to be discovered, but the nature of its superconducting state has been a longstanding subject of debate. $SrTiO_3$ is an incipient ferroelectric and becomes superconductive upon doping, which means that superconductivity is near ferroelectricity in this material. In this thesis, the superconducting states of doped $SrTiO_3$ thin films grown by molecular beam epitaxy are investigated. Epitaxially strained $SrTiO_3$ films tuned into a ferroelectric ground state show a record high superconducting transition temperature and field. Untangling the intertwined relationship between superconductivity and ferroelectricity in $SrTiO_3$ could pave the way towards understanding the nature of the superconducting state.

Antiferromagnetic ordering can potentially bridge topological phenomena and spintronics. $EuTiO_3$ is a tunable antiferromagnet. In this thesis, the topological states of doped $EuTiO_3$ thin films grown by molecular beam epitaxy are investigated. Unusual anomalous Hall effects are observed in doped $EuTiO_3$. The non-monotonic Hall signal was attributed to topological Hall effect. The magnitude and sign of these Hall effects strongly depend on the carrier concentration. The strong dependence on the carrier concentration makes $EuTiO_3$ of potential interest for topological field-effect devices. It is also shown that the magnetic field can systematically control the symmetry of electronic states in $EuTiO_3$. Finally, the formation of a two-dimensional electron system at the $SmTiO_3/EuTiO_3$ interface is studied. The results open interesting possibilities for epitaxial heterostructures that combine topological states, antiferromagnetic ordering, and other phenomena.

Discovery of a wide range of emergent phenomena at interfaces between complex oxides generated excitement in last decade. In this thesis, the polar discontinuity at the interface of two perovskite titanates, $SrTiO_3$ and $SmTiO_3$, is investigated. The polar discontinuity is compensated with half-electron donation per interfacial unit cell to the $SrTiO_3$ conduction band, potentially leading to electron-electron correlation effects. At the $SmTiO_3/SrTiO_3$ interface, a gate voltage induced metal-insulator transition is observed. Increasing the thickness of $SmTiO_3$ or $SrTiO_3$ lowers the resistance below the Mott-Ioffe-Regel limit at low temperatures. In these structures an abrupt metal-insulator transition is observed in a narrow temperature window which does not fit conventional description.

Contents

Acknowledgements v
Curriculum Vitæ vii
Abstract ix
Chapter 1. Introduction: perovskite titanates 1
1.1. Perovskites titanates: $SrTiO_3$, $EuTiO_3$, and $SmTiO_3$ 4
1.1.1. $SrTiO_3$ 4
1.1.2. $EuTiO_3$ 5
1.1.3. $SmTiO_3$ 6
1.2. Oxide Molecular beam epitaxy (MBE) 7
1.2.1. Hybrid molecular beam epitaxy 8
1.3. Outline 10
1.4. Permissions and attributions 12
1.5. Electronic transport in *d*- and *f*-bands 14
1.6. Basic definitions 14
1.7. Components of electronic transport 16
1.8. Electron-phonon resistivity $\rho_{e\text{-}ph}(T)$ 17
1.8.1. The normal component of electron-phonon resistivity $\rho_{Ne\text{-}ph}(T)$ 18
1.8.2. The Umklapp component of electron-phonon resistivity $\rho_{Ue\text{-}ph}(T)$ 19
1.8.3. Phonon drag 20
1.8.4. Polaron-phonon resistivity $\rho_{p\text{-}ph}(T)$ 20
1.9. Electron-electron resistivity $\rho_{e\text{-}e}(T)$ 21
1.9.1. The Kondo effect (scattering from magnetic impurities) 23
1.10. Residual resistivity (elastic electron-impurity interaction) $\rho_0(c)$ 23
1.10.1. Matthiessen's rule 24
1.11. Quantum criticality and emergent non-Fermi liquid behavior 24
1.12. Electronic phases of $SrTiO_3$ 27
1.13. Superconductivity on the border of ferroelectricity 30
1.13.1. Isotope substitution 34
1.13.2. Chemical substitution: 35
1.13.3. Uniaxial stress 35
1.13.4. Epitaxial stress 36

1.14. Two-dimensional electron liquids at titanate oxide interfaces 37
1.15. Tuning Two-dimensional electron liquids 40
1.16. Metal-insulator transition at the complex oxide interfaces 41
1.17. Time reversal symmetry and Kramers' theorem 46
1.18. Time-reversal symmetry loss, chiral edge states and quantum Hall effect 47
1.19. Berry phase, Berry connection, and Berry curvature 49
1.20. Topological invariants: Thouless-Kohmoto-Nishtingale-den Nijs relationship for Hall conductivity 50
1.21. Anomalous and Topological Hall effects 51
1.21.1. Anomalous Hall effect: Hall effect with band structure Berry curvature 51
1.21.2. Topological Hall effect: Hall effect with non-trivial spin texture 55
Chapter 2. Carrier density control of Berry phases and magnetism in $EuTiO_3$ 58
2.1. Introduction 59
2.2. Growth and structural characterization 60
2.3. Magnetoelectric measurements 65
2.4. Anisotropic magnetoresistance (AMR) 81
2.5. Spontaneous Hall effects at $SmTiO_3$/$EuTiO_3$ interface 88
Chapter 3. Metal-insulator transitions at $SmTiO_3$/$SrTiO_3$ interfaces 94
3.1. Introduction 95
3.2. Gate-induced MIT above the MIR limit 96
3.3. Sheet resistance with temperature 98
3.4. Gate leakage and gate metal depletion 99
3.5. Transistor behavior 101
3.6. Capacitance voltage and transconductance voltage characteristics 103
3.7. Metal-insulator transition with gate voltage 105
4.8. Temperature-triggered MIT below the MIR limit 108
Chapter 4. Superconductivity intertwined with ferroelectricity in $SrTiO_3$ 119
4.1. Introduction 120
4.2. $SrTiO_3$ thin films epitaxially strained to LSAT 121
4.3. Growth and characterization 122
4.4. Magnetoelectric characterization of normal state 126
4.5. Critical temperature of superconductivity 131
4.6. Interplay between superconductivity and ferroelectricity 133

4.7. Critical field of superconductivity 139
4.8. Superconductivity emerging from ferroelectric state: possibility of unconventional parity and topological superconductivity 143
Chapter 5. Conclusions and future directions 145
5.1. Carrier density control of Berry phases and magnetism in $EuTiO_3$ 146
5.2. Metal-insulator transitions at $SmTiO_3$/$SrTiO_3$ interface 147
5.3. Superconductivity intertwined with ferroelectricity in $SrTiO_3$ 148
Bibliography 151

Table of figures

Figure 1.1. Schematic illustrating the structure of a simple cubic perovskite oxide (center), octahedral distortions and cation displacement (top) and selected interesting properties that result from variations in the structure (middle, bottom). 3
Figure 1.2. Schematic showing film growth using hybrid molecular beam epitaxy (Courtesy of Roman Engel-Herbert).. 10
Figure 1.3. Schematic illustration of (a) Van der Pauw and (b) Hall bar structures for four-terminal electrical measurements.. 16
Figure 1.4. Schematic demonstration of (a) normal and (b) Umklapp electron-phonon scattering mechanisms. Adapted from Ref. [63].. 18
Figure 1.5. Generic phase diagram in the proximity of a quantum phase transition. The horizontal axis is the tuning parameter and the vertical axis is the temperature T. Adapted from Ref. [75]. 26
Figure 1.6. (a) Crystal-field splitting for 3d orbital electronic states with different symmetries. (b) Conduction band dispersion of tetragonal $SrTiO_3$ with spin-orbit interaction. Adapted from Ref. [88].. 28
Figure 1.7. Electronic phase diagram of electron doped $R_xSr_{1-x}TiO_3$ where R represents rare-earth n-type dopants like La, Nd, Sm, and Gd. The phase boundaries are extracted from references [11], [82], [84], [86]–[89]. Adapted from Ref. [88] 30
Figure 1.8. Electronic phase diagram of electron doped and ferroelectric tuned $R_xSr_{1-x}TiO_3$ where R represents rare-earth n-type dopants like La, Nd, Sm, and Gd. The ferroelectric phase boundary shown here is for Sm:$SrTiO_3$ films grown epitaxially on LSAT and is extracted from Ref. [60, 61] and [126]... 33
Figure 1.9. Superconducting critical temperature (Tc) with carrier density for electron doped $SrTiO_3$ from literature (Koonce et al. [81], Lin et al. [12], Suzuki et al. [79], Stucky et al. [104], and Rischau et al. [82], Herrera et al. [105], Tomioka et al. [128] and Ahadi et al. [60]).. 37
Figure 1.10. Schematic illustration of polar/non-polar interface at the (100) type plane of $SmTiO_3$/$EuTiO_3$. 40
Figure 1.11. Schematic of top-gated $SmTiO_3$/$SrTiO_3$ heterostructure using $SmTiO_3$ as the high-κ gate dielectric... 41
Figure 1.12(a) Mott metal insulator where U self-localizes electrons, forming upper and lower Hubbard bands. (b) Schematic realization of U and t parameters. 43
Figure 1.13. Bandwidth and filling-controlled Mott metal-insulator transitions. Adapted from Ref. [140]. 44
Figure 1.14. Mott-Hubbard (a) and charge transfer (b) insulators band structures. Adapted from [140]... 45
Figure 1.15. Two-dimensional electron system with out-of-plane applied magnetic field. The chiral edge state confirms loss of time-reversal symmetry....................................... 48
Figure 1.16. The chiral edge state in (a) real space and (b) momentum space. 49
Figure 1.17. Hall conductivity with respect to longitudinal conductivity. Hall conductivity becomes insensitive to scattering (longitudinal conductivity), highlighting

intrinsic dissipationelss topological transport governed by Berry curvature (adapted from Ref. [155].) 55
Figure 1.18. Conduction electrons moving in a smoothly varying internal magnetization couple adiabatically and accumulate Berry curvature, directly proportional to magnitude of spin chirality. 56
Figure 2.1. In-situ characterization of $EuTiO_3$ during growth. Reflection high-energy electron diffraction of the $EuTiO_3$ film in (a) [100] and (b) [110] azimuths. 61
Figure 2.2. XRD pattern of an $EuTiO_3$ thin film grown on a (001) LSAT substrate. 61
Figure 2.3. Reciprocal space mapping of LSAT/$EuTiO_3$ heterostructure carried out near the 113_{pc} reflection for a $EuTiO_3$ film. 63
Figure 2.4. Cross-section HAADF-STEM image of Sm:$EuTiO_3$ film grown on LSAT, confirming an atomically sharp and uniform interface between film and substrate (courtesy of Salva Salmani-Rezaie). 64
Figure 2.5. Neutron diffraction intensities with temperature for Sm doped $EuTiO_3$ thin films at the magnetic [1 0 L] reflections. Here the incoherent background is removed, and intensities are normalized by the reflection intensity of the [103] substrate (Courtesy of Zach Porter and Stephen Wilson). 65
Figure 2.6. Carrier concentration vs. temperature for Sm-doped $EuTiO_3$ thin films with various carrier densities. 66
Figure 2.7. Sheet resistance as a function of temperature for doped and undoped $EuTiO_3$ thin films. 67
Figure 2.8. Sheet resistance vs. temperature for electron doped $EuTiO_3$ thin films with different carrier densities. 68
Figure 2.9. (a), (b), (c), and (d) shows the magnetoresistance of the doped $EuTiO_3$ with n_{RT}=1.2, 3.4, 6.5, and 8.7×10^{20} cm^{-3}) carrier densities, respectively, at 2 K, 5 K, 10 K, and 15 K. 69
Figure 2.10. Longitudinal magnetoresistance as a function of magnetic field, for various orientations of B for $n_{300K}=3.4\times10^{20}$ cm^{-3} at 2 K. 70
Figure 2.11. The difference between antisymmetric and normal Hall component (R_0B) of the doped $EuTiO_3$ with n_{RT}=1.2, 3.4, 6.5, and 8.7×10^{20} cm^{-3} carrier densities, respectively, at 2 K. 72
Figure 2.12. THE and AHE components after subtraction of the linear Hall component (R_0B) for $n_{RT}=8.7\times10^{20}$ cm^{-3} at 2 K, 5 K, 10 K and 15 K with respect to out-of-plane B component at different B orientations. 73
Figure 2.13. σ_{xy} as a function of σ_{xx} at different carrier concentrations (the data points, from left to right, correspond to $n_{300K}=1.2\times10^{20}$ cm^{-3}, 6.4×10^{20} cm^{-3}, 8.7×10^{20} cm^{-3}, and 3.4×10^{20} cm^{-3} at (a) 2 K and (b) 5 K, respectively. 74
Figure 2.14. (a) The proposed phase diagram for electron-doped $EuTiO_3$ with carrier concentration ($n_{RT}=1\text{-}10\times10^{20}$ cm^{-3}) and out-of-plane magnetic field (0-6 T) at 2 K. (b) Band structure for electron-doped $EuTiO_3$ along Γ-X. The colored lines show z-component of spin (Courtesy of Zhigang Gui and Anderson Janotti). 76

Figure 2.15. THE and AHE components of Hall experiment for $n_{RT}=8.7\times10^{20}$ cm^{-3} at 2 K with respect to out-of-plane magnetic field component at different applied magnetic field orientations.......... 78
Figure 2.16. Magnetometry with field cooling (100 Oe) for doped $EuTiO_3$. 79
Figure 2.17. Magnetic hysteresis for electron doped $EuTiO_3$ films with carrier densities of (a) 3.4×10^{20} cm^{-3} and (b) 6.5×10^{20} cm^{-3}. 80
Figure 2.18. Temperature-independent coefficient from general transport expression of $R(T)=R_0+AT^n$ as function of out-of-plane applied magnetic field. 81
Figure 2.19. (a) Top view of the AMR experiment Hall bar and (b) AMR experiment geometry. 82
Figure 2.20. AMR results for various in-plane applied magnetic fields (0.25 T, 0.3 T, 0.4 T, 0.5 T, 0.6 T, 0.7 T, 0.75 T, 0.8 T, 0.9 T, 1 T, 1.1 T, 1.2 T, 1.25 T, 1.3 T, 1.4 T and 2 T) for half rotation. 83
Figure 2.21. Anisotropic magnetoresistance results with polar graphs at (a) 0.5 T, (b) 1 T, (c) 1.3 T, and (d) 2 T with current parallel to [100] crystallographic direction. 84
Figure 2.22. Anisotropic magnetoresistance results with polar graphs at (a) 0.5 T, (b) 1 T, (c) 1.3 T, and (d) 2 T with current parallel to [110] crystallographic direction. 85
Figure 2.23. Density functional theory resolved band structure of electron doped $EuTiO_3$ with respect to neighboring Eu spin alignment (Courtesy of Xuezeng Lu and James Rondinelli). 86
Figure 2.24. Schematic illustration of the $SmTiO_3$(10 u.c.s)/$EuTiO_3$(60 nm) heterostructure with Van der Pauw contact structure grown on LSAT substrate. 89
Figure 2.25. (a) Temperature dependence of sheet resistance of $EuTiO_3$(60 nm) with and without of the $SmTiO_3$(10 u.c.s). (b) Temperature dependence of the two-dimensional Hall carrier concentration of the $SmTiO_3$(10 u.c.s)/$EuTiO_3$(60 nm) heterostructure.......... 90
Figure 2.26. Magnetization measurements of the $SmTiO_3$(10 u.c.s)/$EuTiO_3$(60 nm) heterostructure at 2 K. (a) Magnetization as a function of temperature under field cooling (100 Oe, in-plane). (b) Magnetization as a function of in-plane applied magnetic field. 91
Figure 2.27. (a) Longitudinal magnetoresistance of the $SmTiO_3$(10 u.c.s)/$EuTiO_3$(60 nm) heterostructure at 2 K, 5 K, 15 K and 30 K. THE and AHE of the $SmTiO_3$(10 u.c.s)/$EuTiO_3$(60 nm) heterostructure at 2 K, 5 K, 15 K and 30 K. 92
Figure 3.1. (a) Schematic cross-section of the $SrTiO_3$/$SmTiO_3$ based field effect device. The two-dimensional electron system at the $SrTiO_3$/$SmTiO_3$ interface are illustrated in shaded region. (b) Optical micrograph, showing top view of the device.......... 97
Figure 3.2. Sheet resistance (R_s) with temperature for $SmTiO_3$/$SrTiO_3$ heterostructure with and without the Pt gate metal.......... 99
Figure 3.3. (a) Gate current density I_{GS} vs. gate voltage V_G at different temperatures (400 K, 350 K, 300 K, 250 K, 200 K, 150 K, 100 K, and 50 K). (b) Gate leakage at room temperature with thermionic fit. 101
Figure 3.4. I_{DS}-V_{DS} characteristics as a function of gate voltage at (a) 400 K, (b) 300 K, (c) 200 K, and (d) 150 K. Gate voltage was varied from -2 V to 1 V (top curve in each panel) in 0.5 V increments. The current is normalized to drain inner circumference. 102

Figure 3.5. (a) Frequency-dependent capacitance voltage characteristics at 300 K. (b) Transconductance as a function of gate voltage at V_{DS}=+6V. 104
Figure 3.6. (a) I_{DS}-V_{DS} characteristic transistor sheet resistance with temperature at different gate voltages extracted from slope of linear region in Fig. 4.4. The solid lines are a variable range hopping fit. (b) Data in (a) as a function of normalized temp. 106
Figure 3.7. (a) Sheet resistance (R_s) as a function of the temperature for heterostructures with various $SrTiO_3$ (20, 60, and 80 nm) and $SmTiO_3$ (3, 5, 7, and 20 u.c.) thicknesses, respectively, as indicated in the legend. (b) Calculated sheet resistance derivative as a function of the temperature. The arrow signifies the resistance anomaly at ~110 K. The dashed line is a power law fit, T^n, to sheet resistance behavior of the 20 u.c. $SmTiO_3$ sample, which is determined n ~ 5/3. 110
Figure 3.8. Metal-insulator transition temperature (T_{MIT}) as a function of carrier density (n_s) for the samples shown in Fig. 4.7. The dotted line is a guide for the eye. The labels specify samples, with the first and second numbers indicating $SmTiO_3$ thickness in number of unit cells and $SrTiO_3$ thickness in nanometers. Here the sample with 20 u.c. thick $SmTiO_3$, does not show a sharp metal-insulator transition and the temperature for the weak upturn in the sheet resistance is illustrated. 112
Figure 3.9. (a) $(eR_H)^{-1}$ vs. temperature. Low temperature data is not shown here due very large resistance which makes the measurement unreliable. (b) Hall angle as a function of T^2. The solid lines are the T^2 fit to Hall angle data. 114
Figure 4.1. Effect of epitaxial strain of crystal structure and symmetry of $SrTiO_3$. An exaggerated comparison between unstrained (a) and epitaxially strained to LSAT (b) $SrTiO_3$. 122
Figure 4.2. In-situ characterization of the $SrTiO_3$ during growth. Reflection high-energy electron diffraction of $SrTiO_3$ film in [100] (a) and [110] (b) azimuths. 123
Figure 4.3. 2θ-ω scan of an $SrTiO_3$ film around the 001 peak of LSAT/$SrTiO_3$ heterostructure. 124
Figure 4.4. Reciprocal space mapping of LSAT/$SrTiO_3$ heterostructure carried out at near 113_{pc} reflection for a $SrTiO_3$ film. 125
Figure 4.5. Cross-section HAADF-STEM image of Sm: $SrTiO_3$ film grown on LSAT. (a) Low magnification image, showing no extended defect. (b) High magnification image, confirming an atomically sharp and uniform interface between film and substrate (Courtesy of Salva Salmani-Rezaie). 126
Figure 4.6. Effect epitaxial strain on Hall carrier density. Temperature dependent carrier density of electron doped $SrTiO_3$ grown on (a) LSAT [48] and (b) $SrTiO_3$ [21]. Only strained films show a carrier loss (n_{loss}=2-6×10^{19} cm^{-3}). 128
Figure 4.7. Effect epitaxial strain on resistivity. Temperature dependent resistivity of electron doped $SrTiO_3$ grown on (a) LSAT [48] and (b) $SrTiO_3$ [21]. Only strained films show a carrier density dependent metal-to-insulator transition. 130
Figure 4.8. Superconducting transitions for Sm-doped $SrTiO_3$ films grown on LSAT with different carrier densities. The resistivity as a function of temperature (1 K-15 mK) at different carrier densities ($nH300K = 2 \times 1019cm - 3{,}6 \times 1019cm - 3, 1.4 \times 1020cm - 3, and\ 2.8 \times 1020cm - 3$) . Lines are a guide for the eye. 132

Figure 4.9. Superconducting transition in La- and Sm-doped $SrTiO_3$ grown on $SrTiO_3$ substrate. Longitudinal resistance with temperature for La- and Sm-doped $SrTiO_3$ grown on $SrTiO_3$ single crystal substrate. The lines are guidance to the eye. 133
Figure 4.10. Connection between the resistance upturn and onset of ferroelectric transition. Temperature dependence of electrical sheet resistance (left axis) and SHG intensity (right axis) for epitaxially strained $SrTiO_3$ films with Hall resolved room temperature carrier concentrations of $n3\mathrm{D} = \mathrm{a}\ 0.6 \times 1020\mathrm{cm} - 3$, $\mathrm{b}\ 1.4 \times 1020\mathrm{cm} - 3$ and $\mathrm{c}\ 2.8 \times 1020\mathrm{cm} - 3$. Black arrows mark onset of ferroelectric transition which is associated with minima is sheet resistance... 134
Figure 4.11. Doping-temperature phase diagram of epitaxially strained Sm-doped $SrTiO_3$. An enhanced superconducting dome appears deep inside the ferroelectric state, highlighting a deep connection between ferroelectric and superconducting orders. The superconductivity diminishes abruptly where ferroelectric order is screened by doped electrons in over-doped samples.. 137
Figure 4.12. Superconducting critical temperature (T_C) with carrier density for electron doped $SrTiO_3$ from literature (Koonce *et al.* [81], Lin *et al.* [12], Suzuki *et al.* [79], Stucky *et al.* [104], and Rischau *et al.* [82], Herrera *et al.* [105], Tomioka *et al.* [128] and Ahadi *et al.* [60]). A significant enhancement of T_C is observed for tuned $SrTiO_3$ towards ferroelectricity at optimally and under-doped $SrTiO_3$, emphasizing importance of long-range ferroelectric order for pairing. Over-doped tuned $SrTiO_3$ samples, where long-range ferroelectric order is screened by charge carriers perform like pristine $SrTiO_3$.... 138
Figure 4.13. Longitudinal magnetoresistance at different temperatures and carrier concentrations. The longitudinal magnetoresistance for Sm-doped $SrTiO_3$ grown epitaxially on LSAT with $nH300K = a\ 2 \times 1019cm - 3, b\ 6 \times 1019cm - 3, c\ 1.4 \times 1020cm - 3,$ and $d\ 2.8 \times 1020cm - 3$ carrier concentrations. 140
Figure 4.14. Upper critical magnetic field (H_{C2}) with normalized temperature and carrier concentration. The H_{C2} for Sm-doped $SrTiO_3$ grown epitaxially on LSAT with $nH300K = 2 \times 1019\mathrm{cm} - 3, 6 \times 1019\mathrm{cm} - 3, 1.4 \times 1020\mathrm{cm} - 3,$ and $2.8 \times 1020\mathrm{cm} - 3$ carrier concentrations.. 141
Figure 4.15. Exceeding the Pauli-Chandrasekhar-Clogston limit, $\mu_B H_{C2}/K_B T_C$=1.84. The under-doped sample with $n_{3D}=0.6\times10^{20}$ cm^{-3} exceeds the Pauli-Chandrasekhar-Clogston limit with out-of-plane applied magnetic field. 144

Tables

Table 1.1. Comparison between transport behaviors of films grown by oxide MBE and other techniques. Adapted from Ref. [28]............ 7
Table 4.1. Values for T_C, H_{C2}, Δ, and ξ extracted for the three Sm-doped $SrTiO_3$ films on LSAT with different carrier densities. 142

Chapter 1. Introduction: perovskite titanates

Perovskite oxides, having a simple ABO_3 chemical formula (where O is oxygen and A and B are cations), display a wide variety of properties. The relative ionic radii between the oxygen, the A cation, and the B cation control the resulting crystal structure, in terms of cation displacements and/or oxygen octahedra tilting [1,2]. Different combinations of cations result in a diverse class of materials with a wide range of polar (e.g. ferroelectric), structural (e.g. antiferrodistortive) and electronic (e.g. superconducting, orbital and spin ordering) instabilities. In this class of materials, multiple states with similar energy scales occur frequently in proximity of each other. Here, a small external stimulus (e.g. applied pressure or field) can generate a large response, making this class of materials interesting for a wide range of applications.

While many unique and exciting properties have been discovered in the perovskite oxide family [3–7], there is only a limited understanding of how neighboring orders interact. The competition or cooperation of adjacent orders may have substantial consequences. For example, the cooperation between neighboring orders with similar energy scales can potentially provide a novel knob to control existing orders or, more excitingly, give rise to new functionalities.

In this thesis, I will mainly focus on magnetotransport properties in two semiconducting perovskite oxide titanate thin films: strontium titanate ($SrTiO_3$) and europium titanate ($EuTiO_3$). The motivation to grow and study perovskite titanate thin films is three-fold: high quality films provide us the opportunity to study fundamental condensed matter properties and emergent phenomena in this class of

materials; advanced growth techniques enable us to fabricate novel geometries and heterostructures with previously unexplored phenomena; heterostructures formed with these materials allow us to harvest their exciting properties for real-world applications.

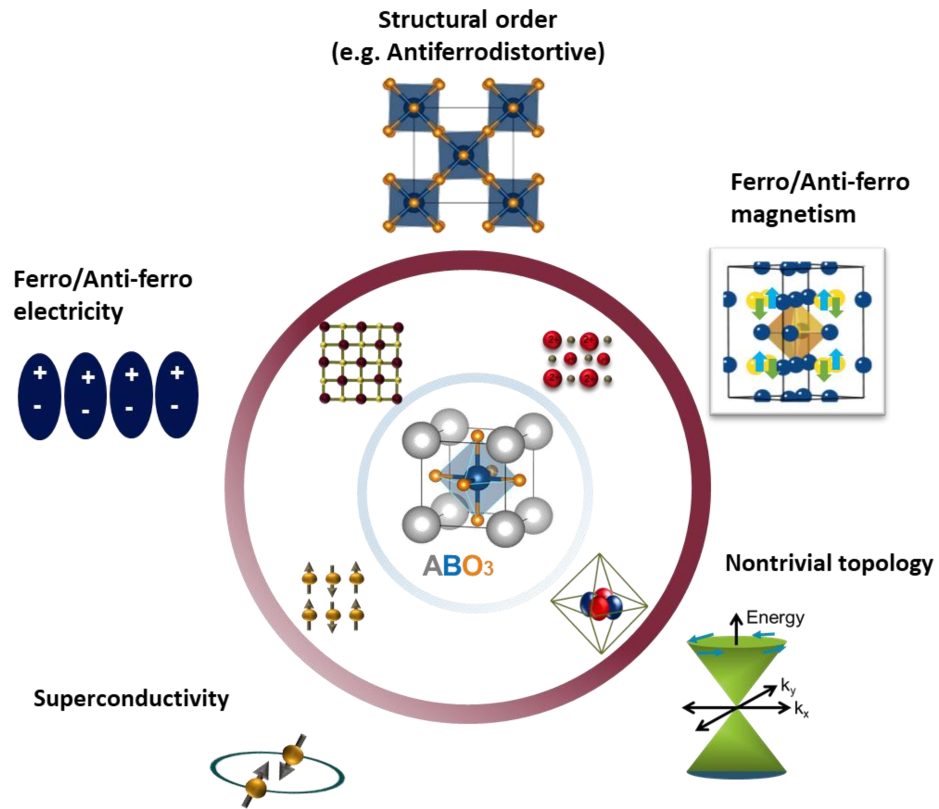

Figure 1.1. Schematic illustrating the structure of a simple cubic perovskite oxide (center), octahedral distortions and cation displacement (top) and selected interesting properties that result from variations in the structure (middle, bottom).

This introductory chapter provides a brief overview of the materials systems ($SrTiO_3$, $EuTiO_3$ and $SmTiO_3$), the growth technique (hybrid molecular beam epitaxy) and an outline of this thesis is given. This chapter also deals with the electronic transport behavior in perovskite titanates. The main theme of this introductory chapter is to establish the groundwork for phenomenological properties affecting electronic transport in perovskite titanates and identify the features that deviate from conventional metals and semiconductors. This introduction will review systematic investigations of transport behavior in $SrTiO_3$ and $EuTiO_3$ tuned by heterostructuring, doping and applied electric and magnetic fields. This chapter starts by describing the anomalous and topological Hall effects using the concept of the Berry phase. Afterwards, an introduction into the polar catastrophe in heterointerfaces of two perovskite titanates ($SrTiO_3$ and $SmTiO_3$) is introduced with a brief overview of the formation of 2D electron liquid at these interfaces. Finally, a brief overview of the electronic phases in $SrTiO_3$ is presented, followed by a review of the interplay between ferroelectricity and superconductivity in this material.

1.1. Perovskites titanates: $SrTiO_3$, $EuTiO_3$, and $SmTiO_3$

1.1.1. $SrTiO_3$

$SrTiO_3$ is one of the materials of interest for this thesis. It shows the ideal perovskite structure ($Pm\bar{3}m$) with a lattice constant of 0.3905 nm at room temperature. A unique aspect of $SrTiO_3$ is its proximity to a ferroelectric transition [8,9]. Its dielectric constant rises drastically with lowering temperature

and plateaus at very large values (ε>20,000) at low temperatures (T<10 K) [8].

In pure and stoichiometric form, $SrTiO_3$ is an insulator with indirect and direct band gaps of 3.3 eV and 3.8 eV, respectively [10]. One can introduce mobile electrons into $SrTiO_3$ through substituting Sr with a trivalent ion (e.g. La, Sm, Nd, Gd, etc.), Ti with a pentavalent ion (e.g. Nb), or inducing oxygen vacancies.

$SrTiO_3$ is the first oxide superconductor to be discovered [11]. It is currently one of the most dilute superconductors known, with a superconducting ground state that has a sharp Fermi surface persisting down to 5×10^{17} cm^{-3} carrier density [12,13]. In this range of carrier concentration, its Debye temperature is over one order of magnitude larger than Fermi temperature and the ability of phonons to mediate electron-electron pairing is uncertain according to Bardeen-Cooper-Schrieffer (BCS) description [14,15].

1.1.2. $EuTiO_3$

$EuTiO_3$ has also a perfect cubic perovskite structure ($Pm\bar{3}m$) with a lattice constant of 0.3905 nm at room temperature. Europium titanate is on the border of ferromagnetic and ferroelectric transitions [16,17]. In pure and stoichiometric form, $EuTiO_3$ is an insulator with a ~0.93 eV energy gap, which is formed between Eu $4f$ and Ti $3d$ [18]. The Eu [$4f^7$ (s=7/2)] shows antiferromagnetic ordering with a Néel temperature of ~5.5 K [19]. Superexchange interaction of Eu electrons through oxygen ions (antiferromagnetic ordering) competes with an indirect

exchange through Eu 5*d* (ferromagnetic ordering). While in $EuTiO_3$ the former dominates [18], the latter controls magnetic ordering in EuO [20].

Doping $EuTiO_3$ introduces itinerant electrons into titanium 3*d* t_{2g} states. In dilute samples, the interaction between localized 4*f* and itinerant 3*d* t_{2g} electrons is reported to be of the Ruderman-Kittel-Kasuya-Yoshida (RKKY) type [21], which favors the ferromagnetic ordering of Eu sites in doped samples. A ferromagnetic ordering with full spin moment of Eu^{2+} (s=7/2) has been reported for doped $EuTiO_3$ structures grown by pulsed-laser deposition (PLD) [19,22]. A more recent neutron diffraction study of high quality doped $EuTiO_3$ grown by MBE shows an antiferromagnetic ground state with doping up to ~10^{21} cm^{-3} [23]. A large negative magnetoresistance around T_c, which is due to the interaction between localized spins and itinerant electrons, has been reported for doped $EuTiO_3$ [12–13]. La-doped $EuTiO_3$ films exhibit a strong anomalous Hall effect (AHE), the sign of which can be manipulated by the carrier density [11].

1.1.3. $SmTiO_3$

$SmTiO_3$ is a Mott insulator in which both A and B cations are in 3+ ionic states [25,26]. Here, the crystal structure is orthorhombic (P*bnm*, a=0.5436 nm, b=0.5748 nm, and c=7.791 nm). $SmTiO_3$ shows antiferromagnetic ordering with two Néel ordering temperatures of 45 K and 70 K for Sm^{3+} and Ti^{3+} sublattices, respectively [27].

1.2. Oxide Molecular beam epitaxy (MBE)

Emergent electronic phenomena are extremely sensitive to disorder. MBE stands out for its unparallel control of composition, thickness and purity in growth of heterostructures. MBE is the “gold standard” technique for growing high quality films for electronic and photonic applications [28]. Table 1.1 compares the quality of oxide films grown by MBE with those of films grown by other techniques.

Table 1.1. Comparison between transport behaviors of films grown by oxide MBE and other techniques. Adapted from Ref. [28].

Material	Best MBE properties	Best non-MBE properties	References
ZnO	$\mu_e = 770\,000$ cm^2/Vs at 0.4 K	$\mu_e = 5500$ cm^2/Vs at 1 K	[29–31]
$SrTiO_3$	$\mu_e = 53\,200$ cm^2/Vs at 2 K	$\mu_e = 6600$ cm^2/Vs at 2 K	[32,33]
$SrRuO_3$	$R_{300K}/R_{4K} = 76$	$R_{300K}/R_{4K} = 8.4$	[34–37]
$SrVO_3$	$R_{300K}/R_{5K} = 222$	$R_{300K}/R_{5K} = 2$	[38–40]
EuO	Metal-insulator $\Delta R/R = 10^8$	Metal-insulator $\Delta R/R = 50000$	[41,42]

MBE benefits significantly from an ultra-high vacuum (UHV) growth environment (<$1 - 10 \times 10^{-10}$ Torr) which enables very large mean free paths (>1-10 Km). Such large mean free paths facilitate the direct transport of a thermally sublimated molecular or atomic beams from high purity source materials to the heated substrate. Delivery of such a beam enables precise control of film growth rate and the possibility of growing heterostructures with precision down to a single atomic layer. Furthermore, in MBE, the molecular beams thermally sublimated from source materials have lower energy (~0.1 eV) compared to PLD (1-10 eV) and sputtering (10-100 eV) [43]. This prevents formation of defects and

intermixing at the interface of heterostructures grown with MBE.

Using lattice-mismatched substrates makes possible the growth of coherently strained films with very large biaxial stresses. This strong perturbation of the lattice brings about novel possibilities of engineering electronic and magnetic properties in materials with strong couplings between lattice, orbital, spin and charge degrees of freedom. The combination of precise growth rate, thickness, and applied stress control, along with high purity and extremely low defect density that can be obtained in thin films, makes MBE an ideal technique for the investigation of emergent phenomena and low temperature transport behavior in quantum materials.

A Veeco Gen. 930 molecular beam epitaxy system was utilized for this work. A schematic of the system is illustrated in Fig. 1.2. A self-regulating growth is key for high quality MBE grown thin films [44]. This regime is frequently referred to as "growth window" in which an unmatched flux of constituents forms a stoichiometric film. High substrate temperature and volatility of constituent elements are of tantamount importance for a wide growth window controlled by adsorption/desorption. A self-regulating growth has been reported for III-V compounds [44], $PbTiO_3$ [45], and $BaBiO_3$ [46] due to volatility of group V elements, Pb and Bi, respectively.

1.2.1. Hybrid molecular beam epitaxy

A self-regulating growth rarely happen in perovskite titanates from

elemental metals due to the low volatility of cations, especially titanium. The low vapor pressure of metals like titanium prohibits stable evaporation of the metal from a regular effusion cell. This issue has been addressed with utilizing a volatile metal-organic precursor called titanium tetra-isopropoxide (50 ^{o}C for 1 Torr vapor pressure) [47]. Titanium tetra-isopropoxide (TTIP) has a chemical formula of $Ti[OCH(CH_3)_2]_4$, where each Ti is bonded to four oxygens. TTIP decomposes to TiO_2 and other volatile byproducts on the surface of a hot substrate (>700 ^{o}C) in a self-regulating growth mode, thus opening a growth window for titanates like $SrTiO_3$ [48], $EuTiO_3$ [49] and $SmTiO_3$ [50,51]. The success of hybrid MBE in the growth of titanates motivated use of this technique in the growth of zirconate [52], vanadate [53], stannate [54] and ruthenate [55,56] complex oxides.

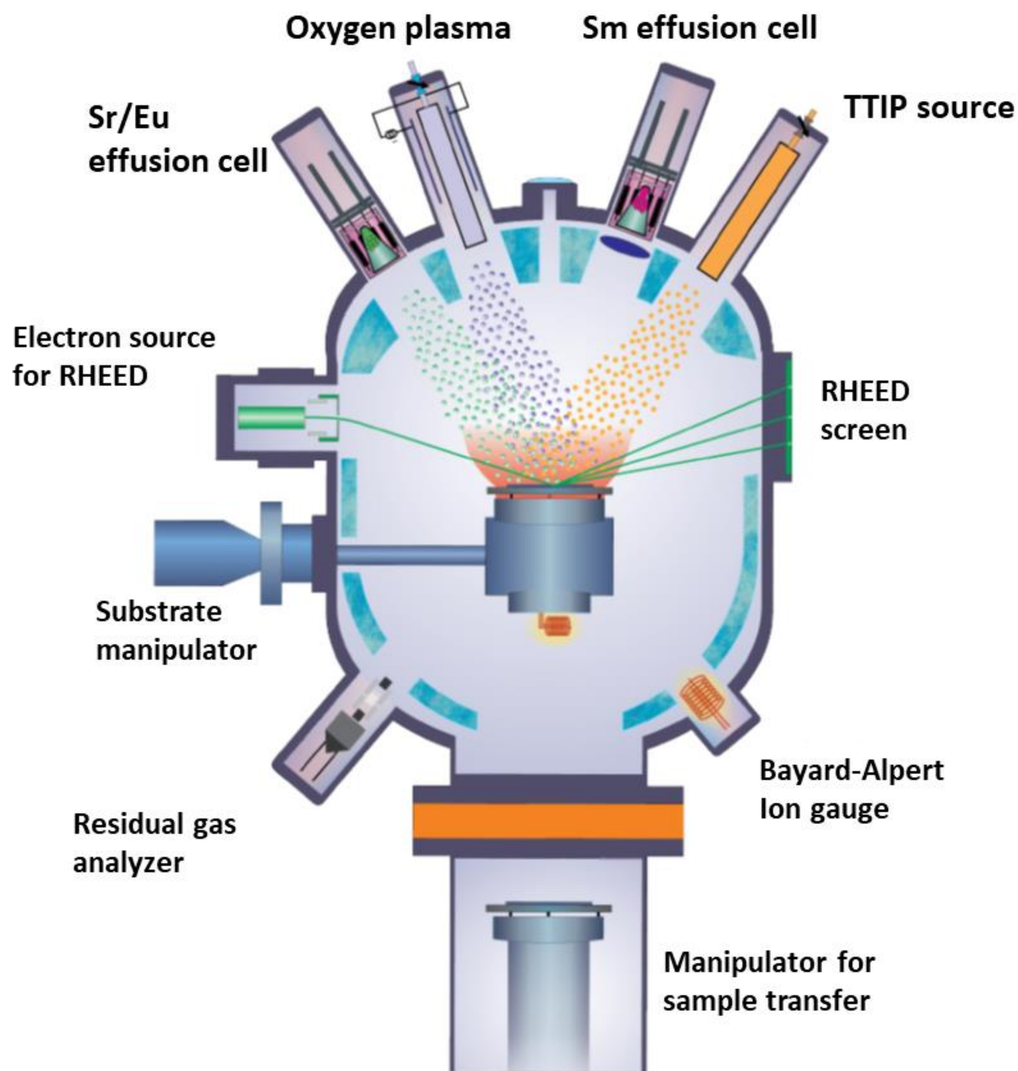

Figure 1.2. Schematic showing film growth using hybrid molecular beam epitaxy (Courtesy of Roman Engel-Herbert).

1.3. Outline

This thesis is organized into four main chapters. Chapter 1 provides background for transport behavior in transition metal oxides and specifically perovskite titanates. Chapter 2 is designated to the cooperation between magnetic

ordering and band structure topology in $EuTiO_3$. Chapter 3 is designated to metal-insulator transition at the $SmTiO_3/SrTiO_3$ interfaces triggered by applied gate voltage and temperature. Chapter 4 covers the cooperation between superconductivity and ferroelectricity in $SrTiO_3$.

In Chapter 1 (1.5-1.20), the background for Chapters 2-4 is laid out. In these sections of chapter 1, electronic transport in *d*- and *f*- derived bands are introduced and is compared to that of conventional semiconductors (typically *s*- and *p*-derived bands). Furthermore, aspects of resistivity in these materials are introduced, which lay the groundwork for the following chapters of this thesis.

In Chapter 2, the effect of carrier density on magnetic structure and band topology of $EuTiO_3$ is introduced. Also, the evolution of magnetic ordering, band topology, and symmetry of the electronic states with magnetic fields is presented. It is shown that magnetic fields can systematically control electronic state symmetry in doped $EuTiO_3$ thin films. Finally, the coupling between the Néel vector orientation and topology of the electronic states in $EuTiO_3$ films was investigated.

Chapter 3 introduces the concept of polar catastrophe in polar/non-polar interfaces of oxide heterostructures. More specifically, the polar discontinuity at the heterointerface of two perovskite titanates, which are band ($SrTiO_3$) and Mott ($SmTiO_3$) insulators is investigated. $SmTiO_3/SrTiO_3$ shows a metal-insulator transition which is triggered with temperature and can be tuned with the geometry

of the heterostructure up to ~260 K. Furthermore, applying electric field shows great promise in inducing a repeatable metal-insulator transition in these heterostructures.

Chapter 4 introduces the concept of superconductivity on the border of ferroelectricity and the possibility of cooperation/competition of these two orders. $SrTiO_3$ is on the border of ferroelectricity. Epitaxially strained $SrTiO_3$ films show a ferroelectric transition with a Curie temperature as high as ~150 K. In this chapter, the interplay between metallicity and ferroelectricity is laid out, and it is described how, films tuned deeply into the ferroelectric ground state show much higher critical temperature and field of superconductivity.

In Chapter 5, the works presented in previous chapters of this thesis are summarized and future research directions that arise from the results in Chapters 3-5 are introduced.

1.4. Permissions and attributions

The contents of Chapter 2 have previously appeared in Applied Physics Letters, 111, 172403 (2017) [49], APL Materials, 6, 056102 (2018) [51] and APL Materials, 6, 056105 (2018) [57]. It is licensed under Creative Commons Attribution (CC BY 4.0) by the AIP Publishing LLC and reproduced here. The contents of Chapter 3, have also partially appeared in Physical Review B, 99, 041106 (2019) [58]. It is Copyrighted by the American Physical Society and reproduced here with permission.

- https://aip.scitation.org/doi/abs/10.1063/1.4997498
- https://aip.scitation.org/doi/abs/10.1063/1.5025169
- https://aip.scitation.org/doi/abs/10.1063/1.5025317
- https://journals.aps.org/prb/abstract/10.1103/PhysRevB.99.041106

The contents of Chapter 3, have partially appeared in Physical Review Letters, 118, 236803 (2017) [50]. It is copyrighted by the American Physical Society and reproduced here with permission. The contents of Chapter 3 have also previously appeared in Applied Physics Letters, 110, 062104 (2017) [59]. It is licensed under Creative Commons Attribution (CC BY 4.0) by the AIP Publishing LLC and reproduced here.

- https://journals.aps.org/prl/abstract/10.1103/PhysRevLett.118.236803
- https://aip.scitation.org/doi/abs/10.1063/1.4975806

The contents of Chapter 4 have previously appeared in Science Advances, 5, eaaw0120 (2019) [60]. It is copyrighted by the American Association for Advancement of Science (AAAS) and reproduced here with permission. The contents of Chapter 5, have also partially appeared in Physical Review Materials, 3, 091401 (2019) [61]. It is Copyrighted by the American Physical Society and reproduced here with permission.

- https://advances.sciencemag.org/content/5/4/eaaw0120.abstract
- https://journals.aps.org/prmaterials/abstract/10.1103/PhysRevMaterials.3.091401

1.5. Electronic transport in *d*- and *f*-bands

Conventional semiconductors frequently used in solid state devices (e.g. Si and GaAs) have electronic bands arising from *s*- and *p*-orbitals. Bands derived from *s* and *p*-orbitals have wider bandwidth and larger kinetic energy for charge carriers compared to bands arisen from *d*- and *f*-orbitals. Accordingly, interactions between the charge carriers are relatively weak and frequently neglected in conventional semiconductors. As the demand for novel functionalities grows, conventional semiconductors face inherent challenges.

The *d*- and *f*- derived bands dominate transport in perovskite titanates. Here, the spatial extent of these bands is smaller than the distance between neighboring cations. Therefore, charge carriers experience narrower band widths and stronger Coulombic interactions at occupied sites. Here, interactions between charge carriers are often a dominant factor, which can give rise to novel and exciting emergent phenomena and functionalities.

1.6. Basic definitions

Electrical resistivity (ρ) or conductivity (σ) is defined based on a linear relationship (i.e. Ohm's law) between the electric field (*E*) and the current density (*J*):

$$J = \sigma E = eNV_d \qquad 1.1$$

where $e, N,$ and V_d are the elementary charge, the carrier density and the drift velocity, respectively. The carrier charge mobility can be defined as the drift

velocity normalized by the applied electric field ($\mu \equiv V_d/E$), and for classical particles the drift velocity is $V_d = eE\tau/m^*$, m^* being the effective mass. Combining the definition of mobility and the classical description of drift velocity, the electron mobility can be shown as:

$$\mu = \frac{e\tau}{m^*} \tag{1.2}$$

Electron mobility contains information about both the charge carrier scattering phenomena (through τ) and the electronic band structure (through m^*). There is a direct proportionality between the charge carrier mobility and the density with conductivity in the Drude picture:

$$\sigma = \frac{1}{\rho} = e\mu N = \frac{e^2\tau N}{m^*} \tag{1.3}$$

Two common four-terminal electrical conductivity measurement methods are shown schematically in Fig. 2.1. Four-terminal measurements eliminate contact resistance, stressing sheet resistance R_s (with units of Ohm/square). The width and length of the conducting channel are crucial for the Hall bar geometry and need to be defined precisely.

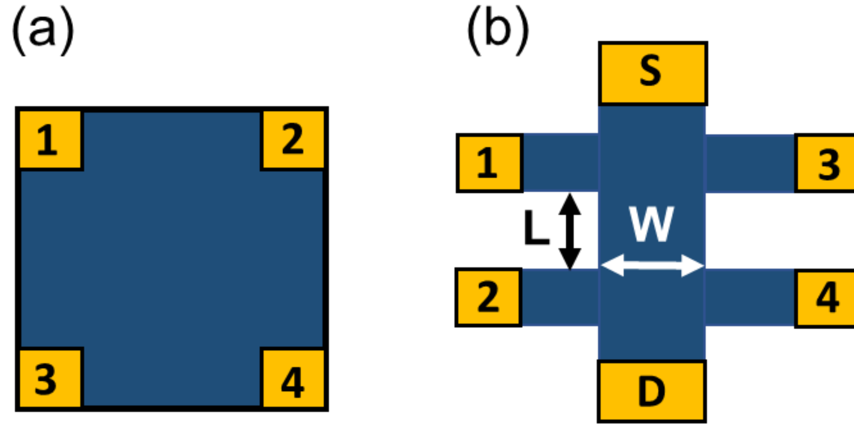

Figure 1.3. Schematic illustration of (a) Van der Pauw and (b) Hall bar structures for four-terminal electrical measurements.

The longitudinal resistance and the Hall coefficient are defined as follows:

$$R_{xx}^{Hall\ bar} = \frac{W}{L}\frac{V_{12}}{I_{SD}} = \frac{W}{L}\frac{V_{34}}{I_{SD}}, R_{xx}^{VdP} = \frac{V_{12}}{I_{34}} = \frac{V_{13}}{I_{24}} \quad 1.4$$

$$R_{H}^{Hall\ bar} = \frac{V_{13}}{BI_{SD}} = \frac{V_{24}}{BI_{SD}}, R_{H}^{VdP} = \frac{V_{24}}{BI_{13}} = \frac{V_{14}}{BI_{32}} \quad 1.5$$

The type and the charge of carriers can be calculated using the measured Hall coefficient ($N = 1/eR_H$) for linear a Hall signal in the low magnetic field regime ($\mu B \ll 1$) under the assumption of a single carrier type.

1.7. Components of electronic transport

The Bloch theorem states that the eigenstates of a one-electron Hamiltonian (Bloch states), having a periodic potential the same as the lattice, can be expressed

in the form of a function with the same periodicity as the lattice times a plane wave [62]. The wave vector of the plane wave (**K**) is used to illustrate the state of the electron. Bloch states are the eigenstates of a periodic Hamiltonian, meaning in the absence of scattering events by other electrons, a perfectly periodic lattice must express zero resistance. In other words, resistance in such systems only arises due to deviations from perfect periodicity in the lattice [63].

1.8. Electron-phonon resistivity $\rho_{e\text{-}ph}(T)$

At high temperatures, phonons (quantized lattice vibrations induced by temperature) are the main source of deviation from perfect periodicity in high-purity metals. Electrons are scattered by phonons leading to a resistivity component ($\rho_{e\text{-}ph}$(T)). It is observed that metals with relatively simple band structures at high temperatures show an electron-phonon resistivity that is linearly varying with temperature ($\rho_{e\text{-}ph}$~T). This *T* dependence gradually shift to higher powers of *T* at lower temperatures [62]. It is customary to recognize two components in the electron-phonon resistivity [63]. The normal component ($\rho_{Ne\text{-}ph}$) includes the scattering of charge carriers by phonons without the contribution of a reciprocal lattice vector [Fig. 1.4(a)]. The second component is called Umklapp ($\rho_{Ue\text{-}ph}$) and includes the contribution of a reciprocal lattice vector [Fig. 1.4(b)].

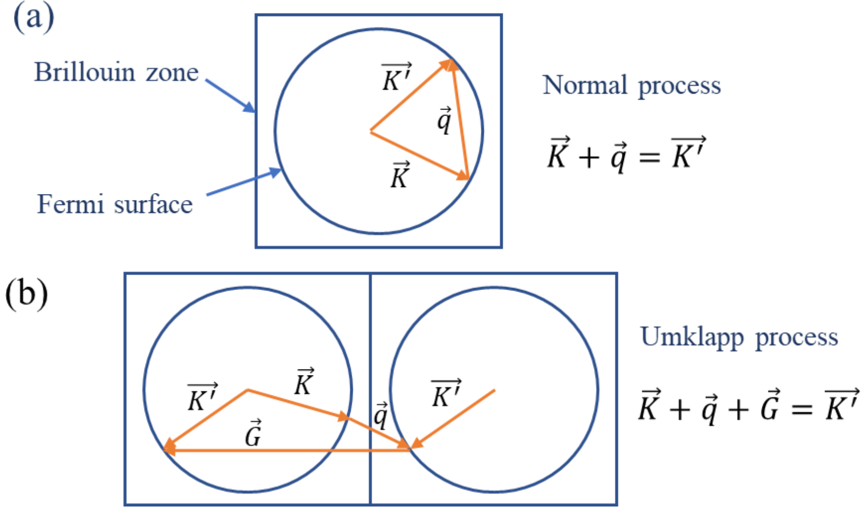

Figure 1.4. Schematic demonstration of (a) normal and (b) Umklapp electron-phonon scattering mechanisms. Adapted from Ref. [63].

1.8.1. The normal component of electron-phonon resistivity $\rho_{Ne\text{-}ph}(T)$

The analytical expression for the normal component of electron-phonon resistivity was proposed by Bloch and Grüneisen based on the Debye model [64]. Phonons are typically characterized by a particle in a box spectrum which is determined by the Debye temperature:

$$\Theta_D = \frac{h\upsilon_D}{k_B} = \frac{h}{k_B}\left(\frac{3}{4\pi}\,N(atoms)\right)^{\frac{1}{3}} \upsilon_s\,, \qquad 1.6$$

where υ_D, h and k_B are the Debye frequency, Planck's constant and the Boltzmann constant. The Debye frequency is given by the volume density of atoms in the crystal times the speed of sound. The Debye frequency represents the crystal's theoretical maximum frequency. The cross section of electron-phonon scattering is

estimated using the amplitude of atomic thermal vibrations, enhancing scattering cross section at elevated temperatures.

The Bloch-Grüneisen model assumes a spherical Fermi surface within the first Brillioun zone, thermal equilibrium of phonons, i.e., no phonon drag, and a phonon spectrum illustrated by the Debye frequency:

$$\rho_{\mathrm{Ne-ph}} = K\left(\frac{T}{\Theta_D}\right)^5 \cdot \int_0^{\frac{\Theta_D}{T}} \frac{z^5 dz}{(e^z-1)(1-e^{-z})} \quad , \tag{1.7}$$

where K is an electron-phonon coupling constant depending on the material. Accordingly, the Bloch-Grüneisen model divides temperature scaling electron-phonon scattering rate into two regimes with respect to Debye temperature:

$$\rho_{\mathrm{Ne-ph}} \sim T \; (T \gg \Theta_D) \tag{1.8}$$

$$\rho_{\mathrm{Ne-ph}} \sim T^5 \; (T \ll \Theta_D) \tag{1.9}$$

1.8.2. The Umklapp component of electron-phonon resistivity $\rho_{\mathrm{Ue-ph}}(T)$

$\rho_{\mathrm{Ue-ph}}$ also varies roughly linearly with temperature T at elevated temperatures and crosses over to a stronger temperature scaling (but not necessarily T^5) at lower temperatures. Ziman [65] and Bailyn [66] expected an exponential temperature dependency at lower temperatures mainly because of the necessity of a minimum wave vector to conserve crystal momentum. Moreover, the temperature for such a dependency should be inversely proportional to Fermi surface distortions.

1.8.3. Phonon drag

In 1930, Peierls predicted that $\rho_{Ne\text{-}ph}(T)$ will be reduced if phonons are dragged out of equilibrium by electron flow at low temperatures [67]. It is also expected that $\rho_{Ue\text{-}ph}(T)$ is reduced, but not by the same order as $\rho_{Ne\text{-}ph}(T)$.

1.8.4. Polaron-phonon resistivity $\rho_{p\text{-}ph}(T)$

$SrTiO_3$ has a Θ_D above room temperature (693 K measured from its elastic constant and 513 K from an estimate of its heat capacity). Therefore, a T^5 behavior is expected at practical temperatures for $\rho_{Ne\text{-}ph}(T)$. Interestingly, such behavior has never been reported. While the Bloch-Grüneisen picture falls short in explaining $SrTiO_3$ resistivity behavior, a polaron-phonon based model has been successful in shedding light on high temperature transport behavior in $SrTiO_3$ [68]. A polaron is a quasiparticle proposed by Landau and Pekar to explain electrons moving in a dielectric material [69]. Atoms move out of their equilibrium position to screen electron charge and the electron effective mass will increase accordingly. This interaction is mediated by the electron-phonon coupling constant (K_{e-ph}):

$$K_{e-ph} = \frac{e^2}{\hbar}\sqrt{\frac{m^*}{2\hbar\omega}}\left(\frac{1}{\varepsilon_\infty} - \frac{1}{\varepsilon}\right), \qquad 1.10$$

$$m_p = m^* \left(1 + \frac{K_{e-ph}}{6}\right), \qquad 1.11$$

where $m^*, \omega, \varepsilon_\infty$ and m_p are the effective mass, the phonon frequency, the high frequency dielectric constant (electronic contribution) and the polaron mass. The

polaron-phonon scattering model predicts a strong temperature dependence for carrier mobility and resistance in $SrTiO_3$ above 200 K [70].

1.9. Electron-electron resistivity $\rho_{e\text{-}e}(T)$

The well-known hallmark of electron-electron resistivity is the T^2 scaling of resistivity in a metallic solid [71]:

$$\rho_{e-e} \sim \frac{1}{\tau_{e-e}} \sim A_{e-e} T^2, \qquad 1.12$$

where A_{e-e} is the temperature coefficient and τ_{e-e} is the scattering rate. The T^2 behavior was explained by Landau considering a scattering event at 0 K between two non-interacting electrons obeying the Pauli exclusion principle and Fermi-Dirac statistics. The Fermi sphere is filled in this model and an excited electron with an energy E_1 ($E_1 \geq E_F$) interacts with a second electron with energy E_2 within the Fermi sphere ($E_2 \leq E_F$). Due to this scattering event, the electron with energy E_1 loses w while the electron with energy E_2 gains w. Moreover, both electrons should be scattered into unoccupied sites ($E_{3,4} \geq E_F$), following the Pauli exclusion principle. Energy conservation requires $E_1 + E_2 = E_3 + E_4$. At 0 K in the absence of activation energy $E_1 = E_F$. Furthermore, the Pauli exclusion principle imposes $E_{2,3,4} = E_F$. Thus, the scattering volume in the vicinity of the Fermi surface collapses into the Fermi surface. This conclusion implies an infinite Fermi surface electron lifetime at zero Kelvin, which is also noticeable from equation 1.12.

The decay rate of a particle with energy ϵ above the Fermi surface can be expressed using Fermi's golden rule at 0 K [71]:

$$\frac{1}{\tau_\epsilon} = \frac{2\pi}{\hbar}\sum_f \left|V_{if}\right|^2 \delta(\epsilon - \epsilon_f), \qquad 1.13$$

where f represents the possible final states and $\left|V_{if}\right|$ the scattering matrix elements. Consequently, the sum over the final states yields a ϵ^2 scattering dependency:

$$\frac{1}{\tau_\epsilon} \sim \frac{\pi}{\pi} V^2 \epsilon^2 g_F^3 \,, \qquad 1.14$$

where g_F is the density of states at the Fermi surface. At finite temperatures (T>0 K), the ambient temperature sets a minimum energy for the quasiparticle in the vicinity of the Fermi surface and the scattering region becomes a shell around the Fermi surface with the approximate width of K_BT. Consequently, a T^2 dependency in the scattering rate and the resistivity becomes recognizable according to equation 1.12. Landau's Fermi liquid theory justifies the validity of the argument above and assumes independent and non-interacting electrons. Landau's Fermi liquid theory considers strongly interacting electrons as quasiparticles.

Beside energy conservation, the total momentum of electrons needs to be conserved in the electron-only process above:

$$\vec{K}_1 + \vec{K}_2 + \vec{K}_3 + \vec{K}_4 = 0 \qquad 1.15$$

Interestingly, this process should not contribute to resistivity. However, a non-zero momentum contribution can be extracted from Umklapp in which the process resolves momentum contribution as lattice reciprocal vector $\vec{G}$.

$$\vec{K}_1 + \vec{K}_2 + \vec{K}_3 + \vec{K}_4 = \vec{G} \qquad 1.16$$

Finally, for equation 1.16 and the Umklapp process to work, the Fermi surface should be near the Brillouin zone boundary, which means that the Brillouin and Fermi surfaces should have roughly the same size ($K_F>G/4$). A robust T^2 behavior of the $SrTiO_3$ resistivity has been reported at various doping concentrations [72,73].

1.9.1. The Kondo effect (scattering from magnetic impurities)

The Kondo effect refers to the logarithmic resistivity enhancement with decreasing temperature in a metallic phase due to scattering from localized magnetic impurities [71]. Accordingly, the resistivity shows a minimum at the Kondo temperature. At temperatures below the Kondo temperature, the antiferromagnetic interaction between the magnetic impurity and the electron enhances drastically with decreasing temperature. At sufficiently low temperatures, the coupling becomes so strong that they form an inert singlet state.

1.10. Residual resistivity (elastic electron-impurity interaction) $\rho_0(c)$

Impurities in alloys or metals can have a tremendous effect on the scattering rate of charge carriers. Impurities and other static defects (e.g. surfaces, interfaces, dislocations, and grain boundaries) disturb the lattice periodicity locally, adding another component to resistivity [63]. For a relatively dilute concentration of impurities, this component is directly proportional to the impurity concentration. Although, $\rho_0(c)$ is generally expected to be temperature independent, impurities

with forces and masses different from the lattice host can modify Θ_D, and accordingly add a temperature dependent term to the resistivity.

1.10.1. Matthiessen's rule

Matthiessen and Vogt showed in 1864 that the total resistivity for various alloys could be estimated by the sum of the pure host metal ($\rho(T)$) and the temperature independent impurity ($\rho_0(c)$) components of resistivity [63]. This additivity (simple series resistance model) is known as Matthiessen's rule. Furthermore, Matthiessen's rule can be written for different scattering mechanisms:

$$\tau^{-1}(T) = \tau_0^{-1} + \sum_i \tau_i^{-1}(T) \qquad 1.17$$

Four conditions need to be met for Matthiessen's rule to be valid: (a) impurities must not alter the properties of the host materials; (b) there should not be any interaction between different scattering mechanisms; (c) impurity scattering must be temperature independent; and (d) electron distribution in k space should be the same for both pure-material and impurity scatterings.

1.11. Quantum criticality and emergent non-Fermi liquid behavior

The quantum critical point (QCP) occurs at the boundary between ordered and quantum disordered phases tuned by a non-thermal tuning parameter δ (e.g. magnetic field, doping, pressure) [74]. Quantum phase transition (QPT) refers to a transition between ordered and disordered quantum phases driven by a non-thermal

driving force δ (magnetic field, doping, pressure) at 0 K. Proximity to the critical tuning parameter is defined, accordingly, in classical phase transition (CPT) theory [75]:

$$r \equiv \frac{\delta - \delta_c}{\delta_c} \qquad 1.18$$

It is also known from classical phase transition (CPT) theory that the correlation length (ξ_L) diverges at the critical point (r=0) to a critical exponent (ν):

$$\xi_L \sim |r|^{-\nu} \qquad 1.19$$

In classical phase transition theory, thermal fluctuations destroy the ordered phase. The order parameter reflects quantum mechanical nature of transition. While QPT cannot be reached experimentally, quantum mechanical fluctuations of the order parameter are still relevant at finite temperatures. Figure 1.5 shows a generic phase diagram for QPT. Interestingly, a "quantum critical fan" is recognizable at *T*>0 K above QCP.

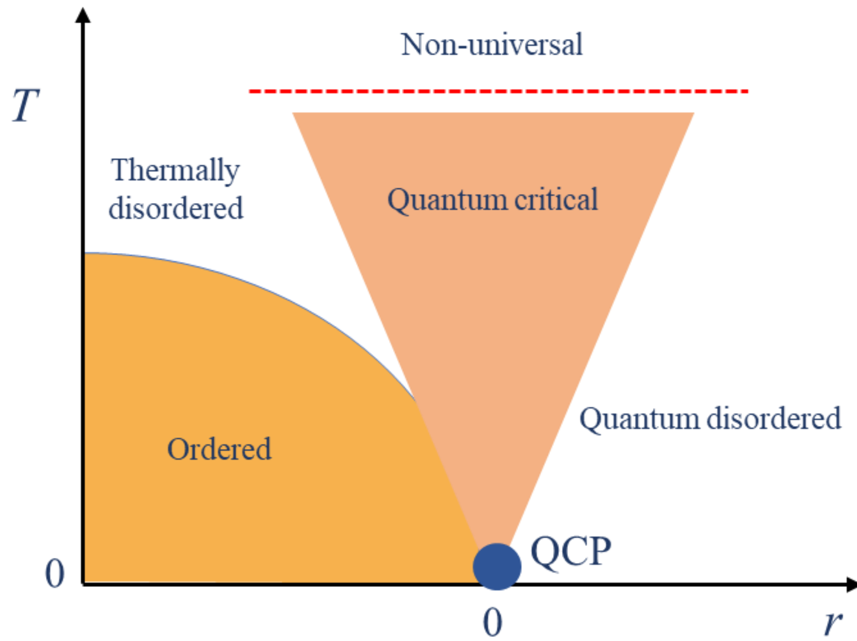

Figure 1.5. Generic phase diagram in the proximity of a quantum phase transition. The horizontal axis is the tuning parameter and the vertical axis is the temperature T. Adapted from Ref. [75].

If the energy scale of the order parameter is smaller than the thermal one ($E < k_B T$), the correlation time ξ_τ is longer than the thermal one. Accordingly, the system might now be governed by a "quantum critical" spectrum of fluctuations that can give rise to anomalous temperature dependencies of physical properties in the proximity of QCP, potentially stabilizing strange phases.

Anomalous temperature dependencies of electronic properties (electrical resistivity, heat capacitance and magnetic susceptibility) in the proximity of a ferro- and antiferromagnetic orders often hint deviation from the Landau's Fermi liquid theory:

$$\rho_{FL} \sim AT^2 \quad 1.20$$

$$C_{FL} \sim \gamma T \quad 1.21$$

Such "non-Fermi liquid" (NFL) behavior refers to anomalous temperature dependencies observed near the quantum critical point (QCP):

$$\rho_{NFL} \sim AT^n, 1 \leq n < 2 \quad 1.22$$

$$C_{NFL} \sim Tlog(T) \quad 1.23$$

A universal microscopic picture for NFL behavior is still an ongoing problem in theoretical condensed-matter physics.

1.12. Electronic phases of $SrTiO_3$

Strontium titanate is a cubic perovskite and the lowest electron doped states are sixfold t_{2g} manifold. Combination of tetragonal distortion, occurring at ~105 K, and spin-orbit coupling lifts this degeneracy. Accordingly, the six-fold t_{2g} orbital splits into two-fold d_{xy}, d_{xz}, and d_{yz} states. The energy momentum dispersion of the three resulting bands is illustrated in Fig. 1.6 [76,77].

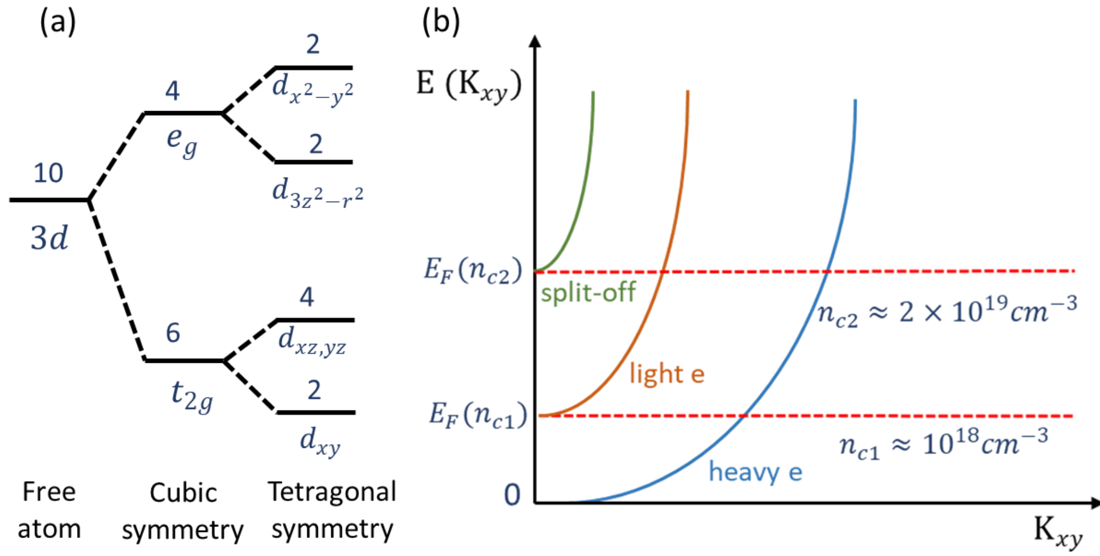

Figure 1.6. (a) Crystal-field splitting for 3*d* orbital electronic states with different symmetries. (b) Conduction band dispersion of tetragonal $SrTiO_3$ with spin-orbit interaction. Adapted from Ref. [88].

Three concentric bands are filled consecutively starting with the heavy electron band (up to ~10^{18} cm^{-3} carrier concentration). It is called the heavy electron band due to the large effective mass of xy plane electrons. Above the critical carrier concentration of ~10^{18} cm^{-3} the light electron band starts to fill [12]. Finally, above the critical carrier concentration of ~10^{19} cm^{-3} the split-off electron band starts to fill [12].

Mobile electrons are donated into $SrTiO_3$ by substituting Sr with La [78,79], Nd [80] or Sm [60], Ti with Nb [81], or removing oxygen [82]. The electron doped phase diagram of $SrTiO_3$ hosts a fertile land for a wide range of exciting electronic phases and emergent phenomena. This is underscored by the

($(R_xSr_{1-x})TiO_3$, (with *R*= La, Nd, Sm, and Gd) phase diagram in which there is no immiscibility region for the solution of rare earth ions in the strontium titanate structure. R acts as an n-type dopant and substituting each Ti^{4+} with R^{3+} donates one electron to $SrTiO_3$. Substituting Ti with Nb or removing oxygen have an upper limit to the doping concentration ($n \approx 5 \times 10^{20}$ cm^{-3}) than can be achieved. Figure 1.7 illustrates the rich phase diagram of $(R_xSr_{1-x})TiO_3$ in which x can be tuned freely, with $RTiO_3$ (a Mott insulator) and $SrTiO_3$ (a band insulator) on two ends.

Here the metallic state ($d\rho/dT > 0$) extends down to a very dilute regime (~10^{15} cm^{-3}) without any sign of carrier freezeout at low temperature. This is primarily due to the very large Bohr radius of conduction electrons in $SrTiO_3$ [83]. If the dopant density exceeds x=0.5, the structure goes through a transition into a doped $RTiO_3$ with $GdFeO_3$-type distortions. Further increase, of *R* triggers a filling-controlled Mott metal-insulator transition [84] with strong electron correlations that are characteristic of rare earth titanates ($RTiO_3$ with *R*=La, Nd, Sm, Gd, Dy, Ho, Er, Yb) [27,70,85–88]. Finally, depending on the ionic radius of the rare earth cation, an antiferromagnetic (T_N=10-140 K) or a ferromagnetic (T_C=10-60 K) ground state dominates [27].

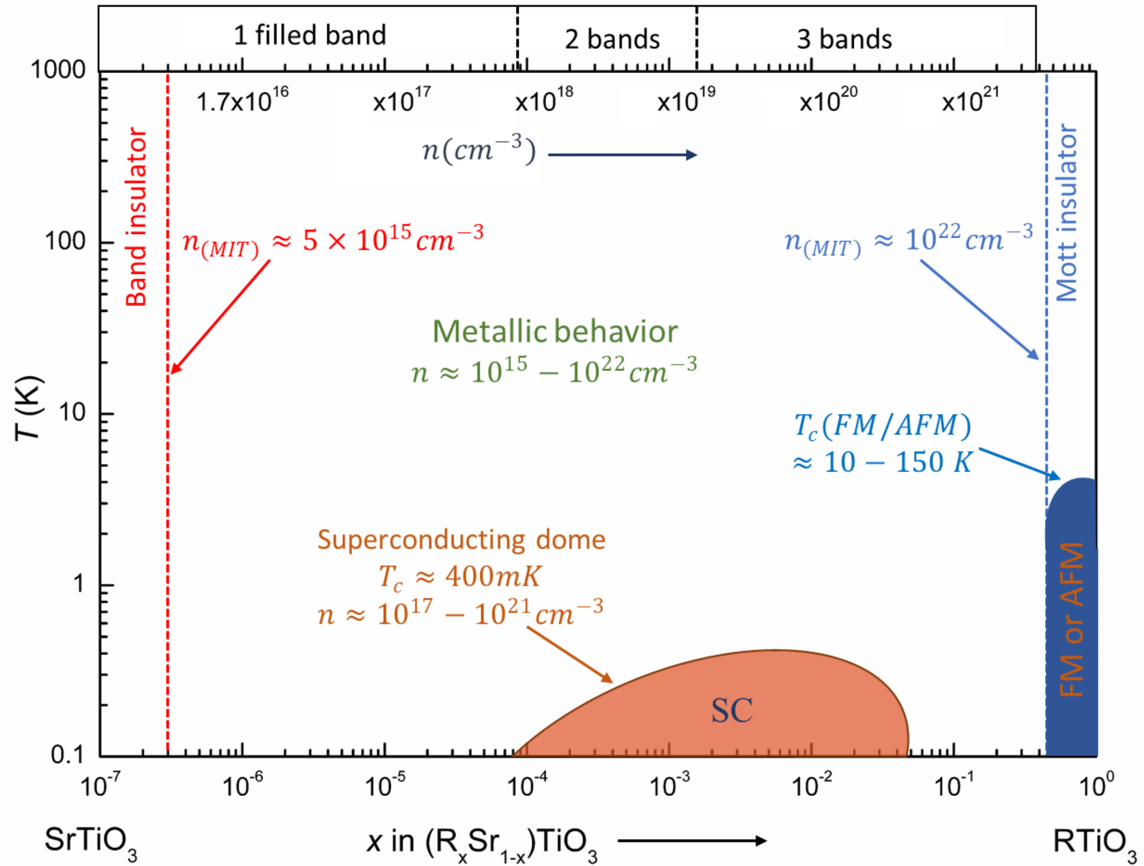

Figure 1.7. Electronic phase diagram of electron doped $R_xSr_{1-x}TiO_3$ where R represents rare-earth n-type dopants like La, Nd, Sm, and Gd. The phase boundaries are extracted from references [11], [82], [84], [86]–[89]. Adapted from Ref. [88]

1.13. Superconductivity on the border of ferroelectricity

$SrTiO_3$ is a quantum paraelectric [8], which can be tuned into the ferroelectric state using isotope substitution [9,89], chemical substitution [90,91], or applied strain [92–94]. $SrTiO_3$ also becomes superconducting upon doping [81,95] which means that superconductivity is near a ferroelectric state in

this material. It is not uncommon for superconductivity to occur in the vicinity of another electronic order in unconventional superconductors [96–99]. Here superconductivity and ferroelectricity could be closely connected, which brings up the unique opportunity of using ferroelectricity to control superconductivity. More recently, theoretical predictions [100–103] and experimental observations [82,103–106] have raised the possibility of connections between the two orders in $SrTiO_3$. Furthermore, it is predicted that the intersection of ferroelectricity and superconductivity hosts exciting quantum phenomena like Majorana fermions in $SrTiO_3$ [107,108]. Finally, untangling the convoluted relationship between superconductivity and ferroelectricity in $SrTiO_3$ could pave the way towards understanding the nature of the superconducting state, which is to this date not clearly understood in this material [14,103].

A striking feature here is that superconductivity in $SrTiO_3$ appears in the very dilute regime ($\sim 5 \times 10^{17}$ cm^{-3} [109]), where the Fermi temperature is lower than the Debye temperature, which is at odds with a Bardeen-Cooper-Schrieffer (BCS) description [110,111]. Furthermore, the presence of superconductivity at such small density of states around the Fermi level hints a very strong interaction which, if it remains effective at sufficiently large carrier densities, can lead to superconductivity at elevated temperatures. The nature of these interactions is still heavily debated in $SrTiO_3$. Recently, antiferrodistortive (AFD) phonons [112], longitudinal optical phonons [113], plasmons [14] and quantum fluctuation of ferroelectric mode [100] have been proposed to mediate the formation of Cooper

pairs.

The phase diagram of electron doped $SrTiO_3$ tuned into the ferroelectric state is vastly unexplored and highly complicated due to the interplay between mobile charge carriers and spontaneous polarization. For example, a substantial density of charge carriers can screen the splitting of the longitudinal and transverse optical phonon modes [114,115], which is crucial for ferroelectricity in perovskites [116]. Also, whether the transition has order-disorder or displacive character in first place in this class of materials [61,117]. The phase diagram of $(R_xSr_{1-x})TiO_3$ with a ferroelectric ground state is illustrated in Fig. 1.8. Here, the tantalizing question is how the critical temperature, field and carrier concentration of superconductivity varies with a continuous tuning towards the ferroelectric ground state. But probably the fundamental and more exciting question is the possibility of coexistence between ferroelectricity and superconductivity in the first place.

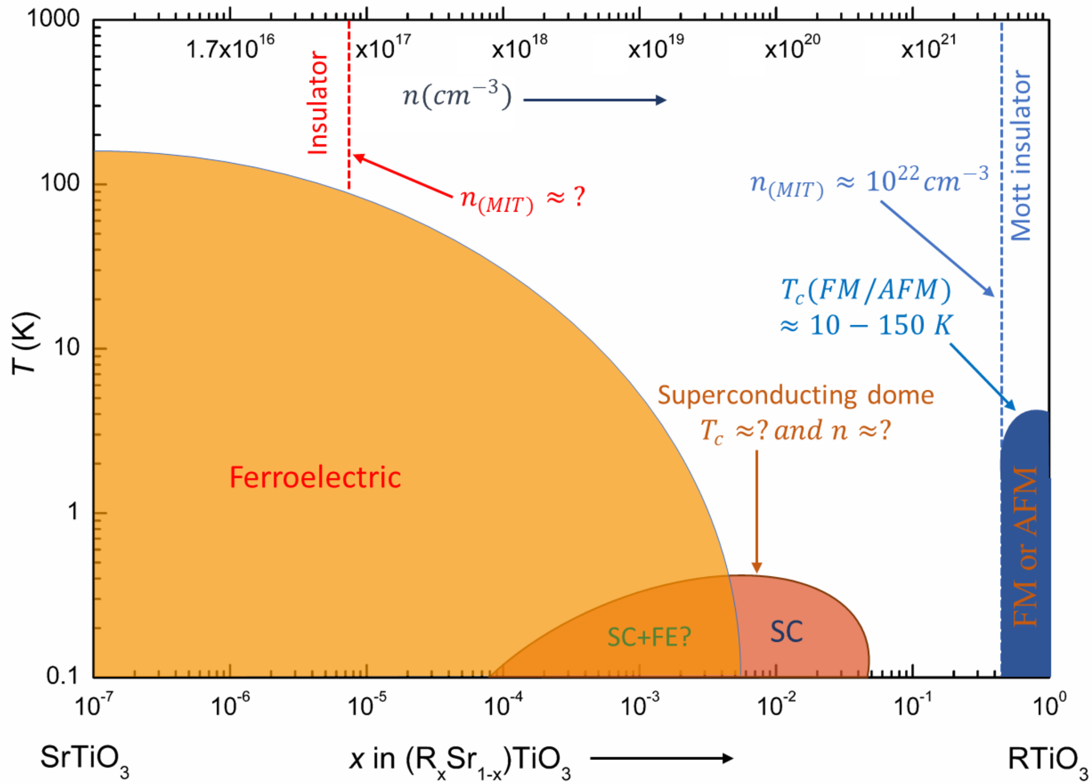

Figure 1.8. Electronic phase diagram of electron doped and ferroelectric tuned $R_xSr_{1-x}TiO_3$ where *R* represents rare-earth n-type dopants like La, Nd, Sm, and Gd. The ferroelectric phase boundary shown here is for Sm:$SrTiO_3$ films grown epitaxially on LSAT and is extracted from Ref. [60, 61] and [126].

Similar to cuprates and heavy fermions where low energy spin excitations in the proximity to magnetic quantum criticality are invoked to explain superconductivity [118,119], quantum fluctuations of the ferroelectric mode are proposed to explain superconductivity in $SrTiO_3$ [100]. Accordingly, the q=0 optical phonon modes are responsible for the pairing interactions in $SrTiO_3$. It is

expected that tuning the system away from ferroelectric quantum criticality will suppress the superconducting order parameter.

More recently, experimental results have shown a sizeable enhancement (up to 100%) in the superconducting critical temperature in $SrTiO_3$ samples tuned towards the ferroelectric ground state using epitaxial stress [60], uniaxial stress [105], chemical substitution [82] and isotope substitution [104,106,120]. Ferroelectric enhancement of superconductivity in tuned $SrTiO_3$ suggests the critical role of proximity to ferroelectric order in pairing and limits theoretical proposals for emergence of superconductivity. In the following, each tuning method and the corresponding results are discussed.

1.13.1. Isotope substitution

The BCS weak coupling limit predicts -5% variation of critical temperature of superconductivity with ^{18}O substitution ($\alpha = -d(\ln T_c)/d(\ln M) = 0.5$ where α is the isotope coefficient and M is the isotope mass). Conversely, a considerable enhancement in the superconducting transition temperature is reported using ^{18}O substitution with oxygen vacancy [104] and La [106] doping. Here both the sign and magnitude of change in T_c are incompatible with the BCS description. A negative isotope coefficient was previously reported for the metal hydrite $PhH(D)_x$ [121] and the high T_c superconductor $Bi_2Sr_2Ca_2Cu_3O_{10}$ [122]. Here, $SrTiO_3$ becomes ferroelectric upon substituting 35% or more of oxygen atoms with

isotope ^{18}O [89]. More recently, a factor of two enhancement in the superconducting transition temperature was reported with 50% ^{18}O substitution [120].

1.13.2. Chemical substitution:

$SrTiO_3$ becomes ferroelectric with small substitution (>0.2%) of Sr with isovalent Ca [90]. It was reported that $Sr_{1-x}Ca_xTiO_{3-\delta}$ bulk single crystals have an enhanced critical temperature of superconductivity [82]. Here a resistance upturn at 15-25 K for carrier densities of 1.3×10^{19} cm^{-3}- 8.3×10^{17}cm^{-3} is associated with the ferroelectric transition. The hardening of the soft transverse optical phonon mode responsible for the ferroelectric transition occurs at the same temperature as the resistance anomaly using Raman spectroscopy. Increasing carrier density ($\geq 2 \times 10^{19}$ cm^{-3}), the resistance anomaly vanishes, suggesting the screening of long-range polarization. It was shown that oxygen deficient $Sr_{1-x}Ca_xTiO_3$ has an enhanced critical temperature of superconductivity only when ferroelectric and superconducting states coexist and at higher carrier densities, where free charge carriers screen long-range polarization the critical temperature of superconductivity agrees with previously reported values for $SrTiO_{3-\delta}$.

1.13.3. Uniaxial stress

By applying uniaxial stress, an asymmetric response of the critical temperature of superconductivity was reported [105]. It is predicted that a ferroelectric ground state can be stabilized in $SrTiO_3$ using strain [92,123]. Nb

doped $SrTiO_3$ single crystals show a significant enhancement of T_c under uniaxial tensile stress along [001] while compressive stress along [001] and [110] yields suppression of superconductivity. Tensile stress along [001] elongates the c-axis, and motivates the rotation of oxygen octahedra, both of which promote a ferroelectric transition [124]. It is also expected that compressive uniaxial stress along [110] enhances ferroelectricity similar to tensile stress along [001]. The surprising suppression of T_c under compressive stress in this study could have been due to the non-uniform nature of strain fields.

1.13.4. Epitaxial stress

Using epitaxial stress, it was shown that $SrTiO_3$ thin films strained to (001) $(La_{0.3}Sr_{0.7})$ $(Al_{0.65}Ta_{0.35})O_3$ (LSAT) single crystal substrates (~1 compressive in-plane strain) display a ferroelectric ground state below room temperature [60,93,125,126]. It was previously reported that $SrTiO_3$ thin films grown heteroepitaxially on LSAT substrates have a critical thickness of ~200 nm, above which the lattice constant gradually relaxes [127]. The in-plane strain ($\varepsilon = \frac{a_{\parallel} - a_0}{a_0}$) can be estimated as -0.947%, where $a_{\parallel}$ is the in-plane lattice constant of strained $SrTiO_3$ (3.868 Å) and a_0 is the lattice constant of relaxed single-crystal $SrTiO_3$ (3.905 Å). The largest enhancement of T_c to date is reported to have used epitaxial stress with Sm-doped $SrTiO_3$ films grown on LSAT [60]. Figure 2.7 compares the T_c values for $SrTiO_3$ samples with similar carrier densities reported

in the literature, including $SrTiO_3$ films and crystals that are tuned toward ferroelectricity using the aforementioned approaches except for epitaxial stress, which will be discussed in detail in Chapter 5 [12,60,79,81,82,104,105,128].

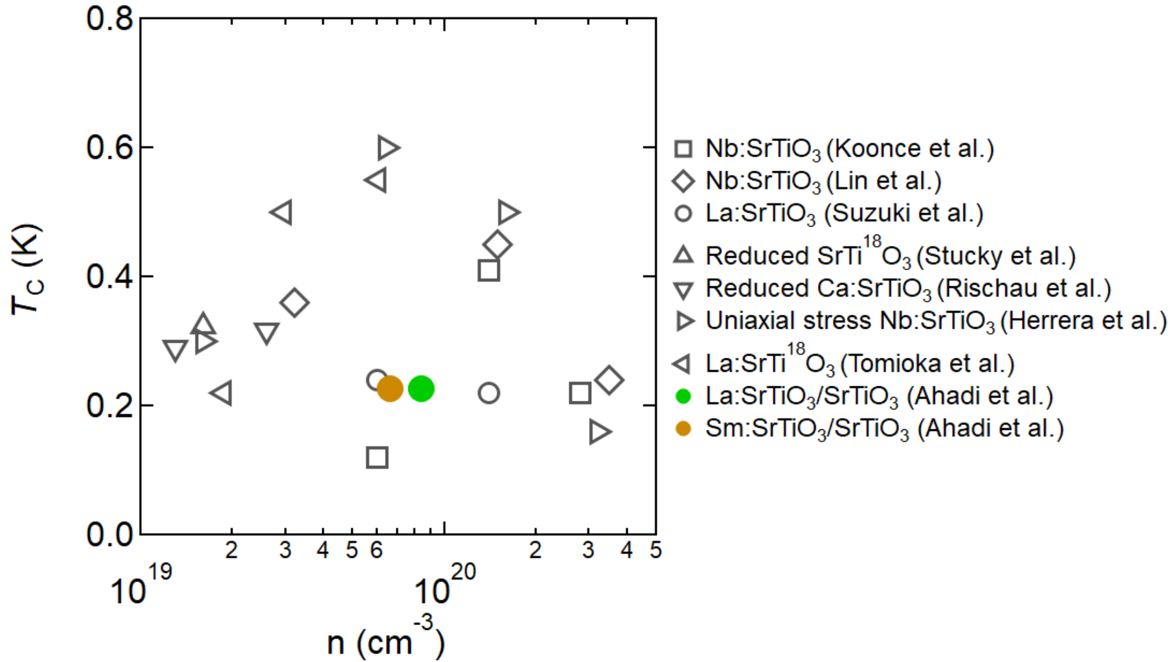

Figure 1.9. Superconducting critical temperature (*T*c) with carrier density for electron doped $SrTiO_3$ from literature (Koonce et al. [81], Lin et al. [12], Suzuki et al. [79], Stucky et al. [104], and Rischau *et al*. [82], Herrera *et al*. [105], Tomioka *et al*. [128] and Ahadi *et al*. [60])

1.14. Two-dimensional electron liquids at titanate oxide interfaces

Discovery of a wide range of emergent phenomena at the heterointerface of complex oxides generated excitement [5,129–133]. High-quality MBE grown group-IV and III-V semiconductors led to many scientific discoveries. States near the bottom of conduction band, which can be approximated with a simple effective

mass, dominate transport in these conventional heterostructure semiconductors. However, an often significantly filled narrow *d*-band controls transport in transition metal oxides. Here exchange coupling and electron-electron coupling can dominate transport. $SrTiO_3$ and $EuTiO_3$ both have d^0 electron configurations and share many similarities with conventional semiconductors, such as a relatively small effective mass. Here, however, the strong coupling to lattice and polaronic transport enhances the effective mass. A metallic state is expected in the case of partially filled *d*-band complex oxides like $RTiO_3$ (rare earths except Eu). Here, strong coupling to the lattice and electron-electron correlations can motivate a wide range of magnetic ordering, charge ordering, and insulating or metallic states, with varying pressure, temperature or magnetic field. In the case of $R$$TiO_3$ (d^1 electronic configuration) while a metallic ground state is expected from a simple electron counting, electron correlation phenomena self-localizes electrons and opens an energy gap. These materials are called Mott insulators which are reviewed in detail in the following section

At the heterointerfaces of $R$$TiO_3$/$SrTiO_3$ or $R$$TiO_3$/$EuTiO_3$, the Mott and band insulators share the same boundary. Furthermore, the d^1/d^0 electronic configurations at these interfaces create an ambivalence for titanium ($Ti^{3+/4+}$) where the polar discontinuity can be compensated with donation of half-electron per interfacial unit cell. The band-offsets at the $R$$TiO_3$/$SrTiO_3$ ($R$$TiO_3$/$EuTiO_3$) interfaces causes electron transfer into the $SrTiO_3$ ($EuTiO_3$) [3,7]. A (001) oriented $SrTiO_3$ ($EuTiO_3$) consists of alternating neutral $Sr^{2+}O^{2-}$ ($Eu^{2+}O^{2-}$) and $Ti^{4+}O_2^{2-}$.

Since there is no dipole, the surface is neutral or non-polar. On the other hand, the $R^{3+}O^{2-}$ and $Ti^{3+}O_2^{2-}$ planes of the $R$$TiO_3$ are polar and have alternating +1 and -1 charges per lateral unit cell. The fixed charge at this interface is energetically unstable is compensated by half-electron per interfacial unit cell of mobile charges. In the case of $SrTiO_3$ or $EuTiO_3$ with a cubic unit cell of 0.3905 nm, the half electron per unit cell amounts to $\approx 3.4 \times 10^{14}\mathrm{cm}^{-2}$, which if confined in the one unit cell corresponds to very large carrier density of $\approx 8 \times 10^{21}\mathrm{cm}^{-3}$. The extremely large carrier density in the narrowly spread *d*-band drastically enhances electron-electron interactions compared to a conventional two-dimensional electron gas (2DEG). This is referred to as a two-dimensional electron liquid (2DEL). In reality, the spatial distribution of the two-dimensional electrons depends on the dielectric constant and is typically in order of tens of nanometers in $SrTiO_3$ [3,134,135]. Fig. 1.10 shows a schematic illustration of the (100) type plane of $SmTiO_3$/$EuTiO_3$.

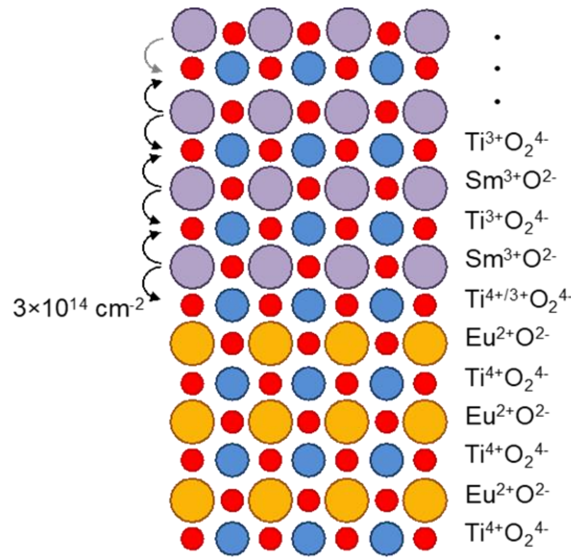

Figure 1.10. Schematic illustration of polar/non-polar interface at the (100) type plane of $SmTiO_3/EuTiO_3$.

1.15. Tuning Two-dimensional electron liquids

Two-dimensional electron liquids formed at polar/non-polar interfaces of perovskite oxides are highly tunable [3,7]. For example, it was shown that carrier density at the $LaAlO_3/SrTiO_3$ interfaces heavily depend on the thickness of the $LaAlO_3$ layer and there is a critical thickness for two-dimensional electron formation [136]. Furthermore, utilizing the electric field, the ground state of the interface can be tuned and a superconducting-insulator transition was reported using applied gate voltage in $LaAlO_3/SrTiO_3$ interfaces [137]. Two-dimensional electron systems at the oxide interfaces can be gated using different geometries like top, side and bottom gating. For example, in the case of $SmTiO_3/SrTiO_3$, the top $SmTiO_3$ layer can serve as both the source for a polar discontinuity, which provides

a mobile electron gas, and as a high-κ gate dielectric [138]. Fig. 1.11 illustrates a schematic cross section of the top-gated $SmTiO_3/SrTiO_3$ heterostructure.

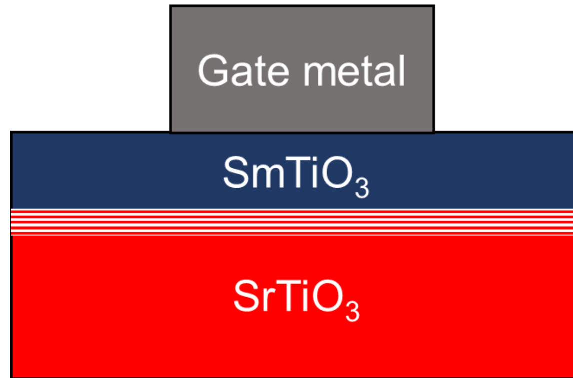

Figure 1.11. Schematic of top-gated $SmTiO_3/SrTiO_3$ heterostructure using $SmTiO_3$ as the high-κ gate dielectric.

1.16. Metal-insulator transition at the complex oxide interfaces

Deciphering and classifying metal-insulator transitions (MITs) are some of the earliest questions in condensed matter physics that continue to be exciting to this date [139,140]. Strong electron correlation induced MITs are the cause of some of the most exciting phenomena in condensed matter. There are two limiting cases: extremely high carrier density, where on-site Coulomb repulsion self-localizes electrons ("strongly correlated materials"); the extremely dilute regime, where unscreened long-range Coulomb interactions dominate. The ground states corresponding to these two cases are the Mott insulator [141] and the Wigner crystal [142], respectively. Wigner crystals have only been observed in one

dimensional electron systems [143].

For example, in case of RTiO$_3$ (d^1 electronic configuration), while a simple electron counting predicts a metallic state, a sufficiently strong on-site Coulomb interaction self-localizes the electrons and splits the band into a filled lower and empty upper Hubbard bands. An insulating behavior in a partially filled d-band oxide was initially reported in NiO [144]. Wigner proposed the electron-electron correlation as principal phenomena [145] and Mott laid out a quantitative model [141]:

$$\mathcal{H} = -\mathrm{t}\sum_{<i,j>,\sigma}(C_{i\sigma}^{\dagger}C_{j\sigma} + C_{j\sigma}^{\dagger}C_{i\sigma}) + U\sum_{i} n_{i\uparrow}n_{i\downarrow} + \mu\sum_{i,\sigma} n_{i,\sigma} \qquad 1.24$$

where U, t and μ are the Coulombic repulsion, the hopping integral and the chemical potential. σ is the spin of the electron, i and j are atomic sites, $C_{j\sigma}^{\dagger}$ and $C_{i\sigma}$are the particle annihilation and creation operator, and n is the number operator. The first term signifies the kinetic energy and hopping between neighboring sites. The second term corresponds to the energy penalty of double occupying site i. The third term accounts for band filling with μ as the chemical potential. Fig. 1.12(a) illustrates a Mott metal insulator in which on-site Coulomb repulsion splints the d band into lower and upper Hubbard bands, and U and t are shown schematically in Fig. 1.12(b).

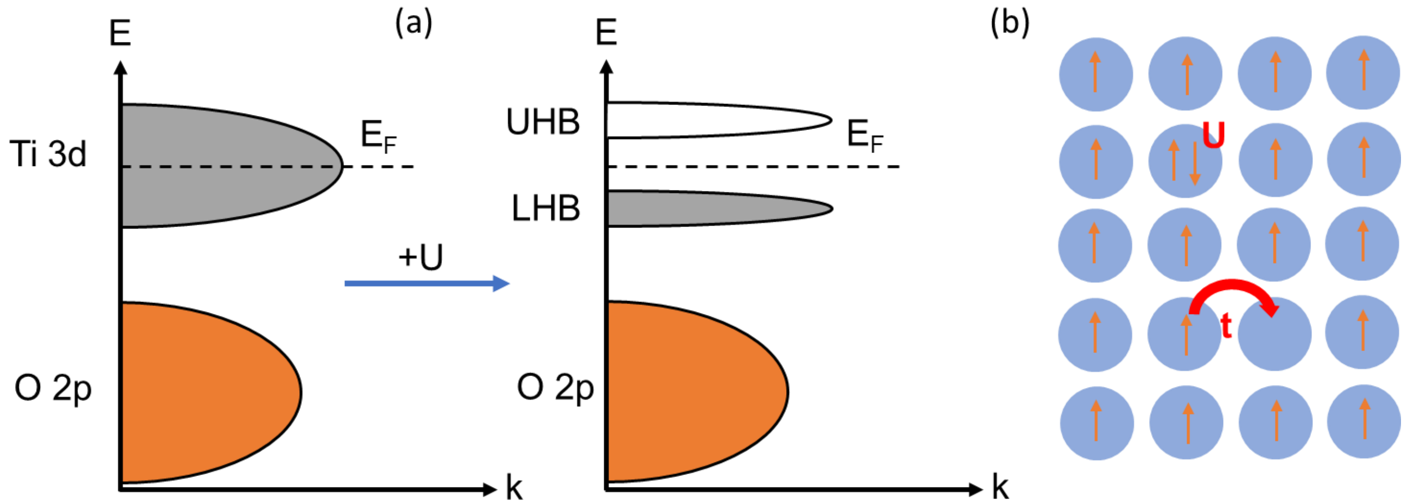

Figure 1.12(a) Mott metal insulator where *U* self-localizes electrons, forming upper and lower Hubbard bands. (b) Schematic realization of *U* and *t* parameters.

Here, the Coulomb repulsion (*U*) of neighboring electrons must be sufficiently large compared to the hopping integral (*t*) to self-localize electrons ($U/t >> 1$). There are two routes for a Mott MIT. The band filling involves manipulating the third term in equation 1.24. The Mott insulating state is only stable near one electron per site carrier density, but it was shown that $SmTiO_3$ Mott insulators can tolerate large carrier densities before a metallic ground state can prevail [84]. The system can tolerate larger deviation from one electron per site in higher *U/t* values (see Fig. 1.13) since stronger *U* can shift balance towards the insulating state. In perovskite oxides the bandwidth can be tuned drastically with the Ti-O-Ti bonding angle. Using scanning transmission electron microscope, it was shown that in $GdTiO_3/SrTiO_3/GdTiO_3$ quantum wells this angle can deviate

from a prefect 180^0 in $SrTiO_3$, thus lowering the bandwidth and causing a MIT [146,147].

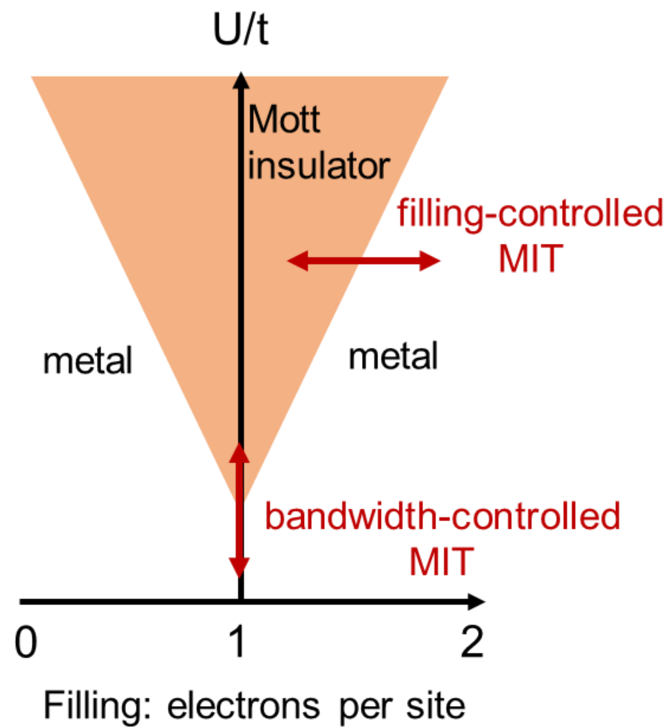

Figure 1.13. Bandwidth and filling-controlled Mott metal-insulator transitions. Adapted from Ref. [140].

Finally, whether the *p-d* charge transfer gap (Δ) is larger ($\Delta > U$) or smaller ($\Delta < U$) than the on-site Coulomb repulsion energy can trigger either Mott-Hubbard or charge transfer insulators, respectively (See Fig. 1.14). Heavier 3*d* transition metals like cuprates and rare earth nickelates tend to have smaller *p-d* charge transfer gaps and are prone towards charge transfer Mott MITs.

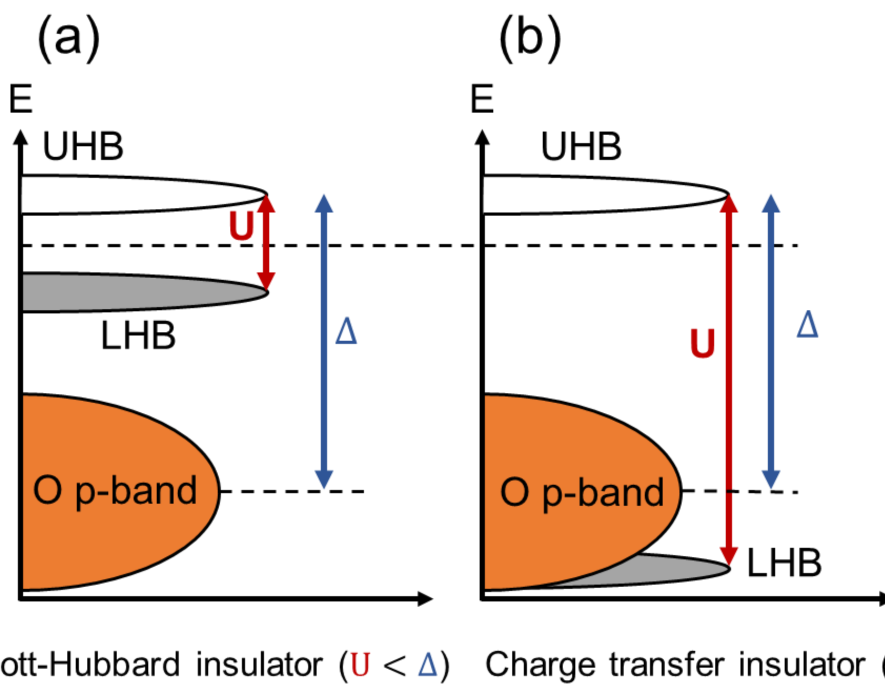

Figure 1.14. Mott-Hubbard (a) and charge transfer (b) insulators band structures. Adapted from [140].

Real materials often substantially deviate from the abovementioned scenarios. For example, a sizeable concentration of defects can localize charge carriers ("Anderson insulator") and dominate transport. Two-dimensional electron systems at polar-nonpolar interfaces avoid dopants and associated defects but

strong spin-orbit coupling via Rashba fields [148] can enhance interactions. In these heterostructures, carrier densities are large for the formation of Wigner crystals which also occur only at zero disorder density, so this scenario seems farfetched here. Finally, low carrier mobilities in complex oxide two-dimensional electron liquids pose the challenge of exceeding quantum resistance or the Mott-Ioffe-Regel limit (*h*/*e* ~ 25 kΩ/□), making the system insulating at low temperatures [137]. The Mott-Ioffe-Regel type insulating state obstructs the correlation-induced MITs emerging from an itinerant two-dimensional electron liquid.

1.17. Time reversal symmetry and Kramers' theorem

Time reversal symmetry (TRS) refers to invariance of a physical property to the change of the time arrow ($t \mapsto -t$). The system is time reversal invariant if its Hamiltonian ($\hat{h}$) stays unchanged under this transformation. A particle located at position $\boldsymbol{r}$ with linear momentum $\boldsymbol{p}$ and spin $\boldsymbol{s}$ time reversal transformation produces an unchanged position and reversal of momentum and spin directions. A time-reversal invariant system should be, for example, independent of spin and an even function of the momentum (e.g. non-relativistic free particles).

$$\boldsymbol{r} \mapsto \boldsymbol{r}, \boldsymbol{p} \mapsto -\boldsymbol{p}, \text{and} \;\; \boldsymbol{s} \mapsto -\boldsymbol{s} \tag{1.25}$$

Kramers' theorem has significant implications for time reversal invariant systems. Kramers' theorem states that for a time-reversal invariant system with half-integer spin, each energy level is at least doubly degenerate. If the system is time-reversal invariant (i.e. $\mathbb{T}$ is a symmetry of the Hamiltonian, $\hat{h}$), two degenerate states must be related with the time reversal operation. Since they are independent states, they must also be orthogonal ($\langle + | - \rangle = 0$). This can be proven simply as following:

$$\langle + | - \rangle = \left\langle - \middle| \mathbb{T}^{\dagger}\mathbb{T}^{-1} \middle| + \right\rangle = -\left\langle - \middle| \mathbb{T}^{\dagger}\mathbb{T} \middle| + \right\rangle = -\langle - | + \rangle^{*} = -\langle + | - \rangle \qquad 1.26$$

1.18. Time-reversal symmetry loss, chiral edge states and quantum Hall effect

Time-reversal symmetry typically holds for non-magnetic systems in the absence of an external magnetic field. One example of the effect of time-reversal symmetry breaking is shown in Fig. 1.15. Here a two-dimensional electron system is subjected to an out-of-plane applied magnetic field, $\boldsymbol{B}$. In the classical description, electrons go through a circular trajectory. While bulk electrons can finish a full circle, electronic states at the edge cannot and these electrons repeatedly hit the edges of the sample. The open orbital trajectory forms the chiral edge state in the quantum picture under strong applied magnetic field while bulk of the sample stays insulating.

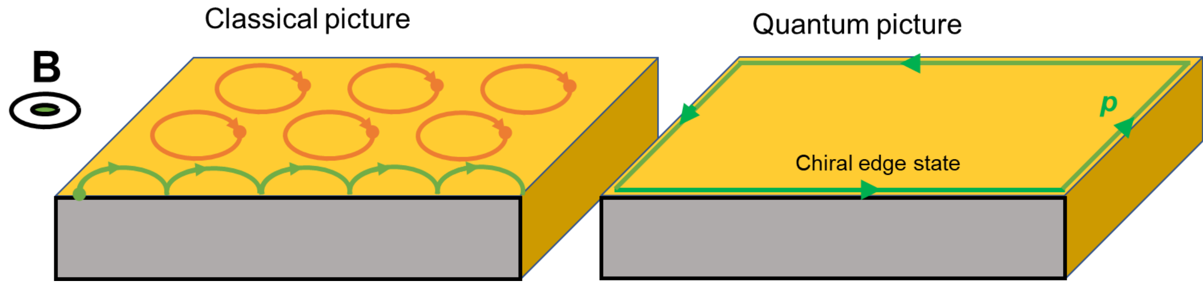

Figure 1.15. Two-dimensional electron system with out-of-plane applied magnetic field. The chiral edge state confirms loss of time-reversal symmetry.

Here quasi-one-dimensional motion of electrons is quantized at the edge of the system. The electronic edge state is protected since backscattering of electronic edge states ($\boldsymbol{p} \mapsto -\boldsymbol{p}$) is prohibited in this system and there is no counter-propagating state. In the limit of strong magnetic fields, the Hall conductivity quantizes into integer units of quantum conductance ($2e^2/h$) [149].

$$\sigma_H = \frac{2e^2}{h} n, \qquad 1.27$$

where e and h are the elementary charge and Planck's constant, respectively. Here dissipationless quasi-one-dimensional transport (without resistance) is due to the lack of a counter-propagating state and scattering events. The bulk must not have mobile charge carriers for this transport, hinting at the presence of edge mode states inside the band gap of the system. Finally, this dissipationless quasi-one-dimensional transport is protected against continuous deformation of the band structure.

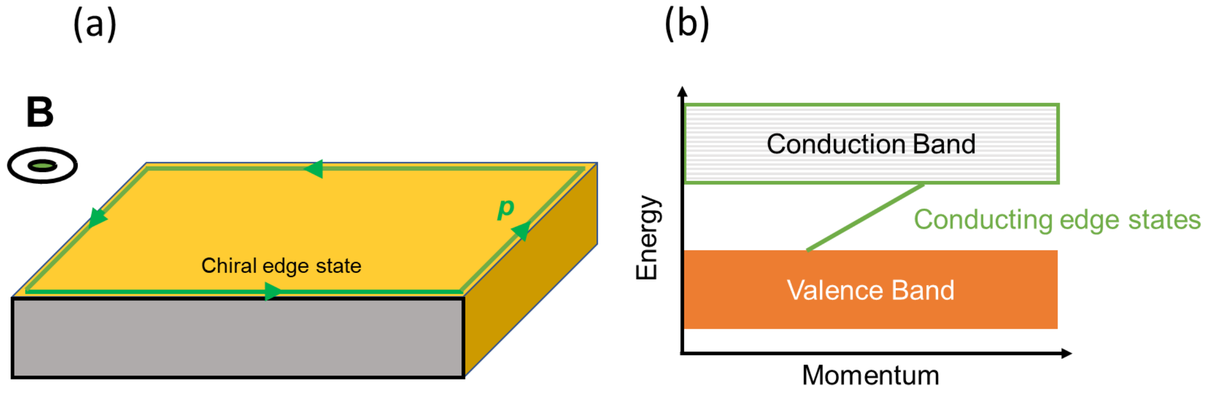

Figure 1.16. The chiral edge state in (a) real space and (b) momentum space.

1.19. Berry phase, Berry connection, and Berry curvature

The quantum phase factor due to an adiabatic evolution of a quantum system is called Berry phase [150]. The quantum phase factor with one adiabatic revolution can be shown as:

$$\gamma_s = -i \oint \langle \varphi_{\boldsymbol{k}s} | \nabla_{\boldsymbol{k}} | \varphi_{\boldsymbol{k}s} \rangle . d\boldsymbol{k} \tag{1.28}$$

where $\varphi_{\boldsymbol{k}s}$ is a bulk state. The Berry connection ($A_{\boldsymbol{k}s}$) is defined as:

$$A_{\boldsymbol{k}s} = \langle \varphi_{\boldsymbol{k}s} | \nabla_{\boldsymbol{k}} | \varphi_{\boldsymbol{k}s} \rangle \tag{1.29}$$

Combining 2.25 and 2.26 with the help of Stokes theorem defines the Berry phase:

$$\gamma_s = \oint A_{\boldsymbol{k}s} . d\boldsymbol{k} = \int (\nabla_{\boldsymbol{k}} \times A_{\boldsymbol{k}s}) dk_x dk_y \tag{1.30}$$

Here the Berry curvature ($\nabla_{\boldsymbol{k}} \times A_{\boldsymbol{k}s}$), unlike the Berry connection ($A_{\boldsymbol{k}s}$) is gauge invariant and plays the role of an effective applied magnetic field [151].

1.20. Topological invariants: Thouless-Kohmoto-Nishtingale-den Nijs relationship for Hall conductivity

Starting from the Kubo formula, Thouless, Kohmoto, Nishtingale, and den Nijs (TKKN) developed a relationship for the Hall conductivity in the limit of zero temperature and frequency, thus relating Hall conductivity to Berry curvature [152]:

$$\sigma_{xy} = \frac{e^2}{h} \int \frac{dk_x dk_y}{2\pi} (\nabla_{\boldsymbol{k}} \times A_{\boldsymbol{k}s})_z, \qquad 1.31$$

where the integration considers the whole Brillouin zone. The TKNN formula establishes a connection between the Hall conductivity and the topology of the structure. Two aspects of Eq. 1.31 need special attention.

- The Berry curvature ($\Omega(k) = \nabla_{\boldsymbol{k}} \times A_{\boldsymbol{k}s}$) is an odd function of momentum with time reversal invariance ($\Omega(k) = -\Omega(-k)$), highlighting a finite Hall conductivity only with broken TRS. So, Hall conductivity can only be nonzero for broken time-reversal and finite Berry curvature.
- The Hall conductivity is quantized with integer values of quantum conductance (e^2/h). Starting from the TKNN formula with a periodic boundary condition, edges of Brillouin zone can be connected. Accordingly, the Fermi surface maps into the surface of a torus without any boundary and the Brillouin zone can be divided into two manifolds with the Hall

conductivity only depending on the random boundary of the two manifolds as follows:

$$\sigma_{xy} = \frac{e^2}{h}\frac{1}{2\pi}\left[\oint_C A_k^I . d\boldsymbol{k} - \oint_C A_k^{II} . d\boldsymbol{k}\right], \qquad 1.32$$

where C is the common boundary between two manifolds. The difference between the Berry connections at the boundary is an arbitrary phase due to gauge invariance. Accordingly, the integer quantization of Hall conductance is directly proportional to the winding number of the phase, n.

$$\sigma_{xy} = \frac{e^2}{h}n, \qquad n = \frac{1}{2\pi}\oint_C (A_k^I - A_k^{II}). d\boldsymbol{k} = \int \frac{dk_x dk_y}{2\pi}(\nabla_{\boldsymbol{k}} \times A_{\boldsymbol{ks}})_z \qquad 1.33$$

Finally, n is determined based on the electronic structure and topology of filled bands and is invariant with continuous deformation of band structure.

1.21. Anomalous and Topological Hall effects

1.21.1. Anomalous Hall effect: Hall effect with band structure Berry curvature

Edwin Hall observed an extraordinary transverse voltage in magnetic metals like nickel and iron shortly after the discovery of ordinary Hall effect. Behavior of this anomalous transverse signal with magnetic field was very similar to magnetization of these materials, hence an empirical relationship was born to explain this mysterious transverse voltage, Eq. 1.34.

$$H_e = H_0 + 4\pi M\alpha, R_H = R_0(H_0 + 4\pi M\alpha), \quad 1.34$$

where M and H are the magnetization and the applied magnetic field, respectively. Karplus and Luttinger revisited the problem in 1954 [153]. Their calculations surprisingly showed that the anomalous Hall conductivity only depends on the effective mass and the spin-orbit coupling, which was in good agreement with experimental results for high quality Fe and Ni.

$$R_{AHE} \sim \frac{B_{s.o}}{m^*} R_{xx}^2 \quad 1.35$$

Karplus and Luttinger showed that electrons acquire an *anomalous velocity* (second term in Eq. 1.36) perpendicular to the applied electric field, and hence a Hall effect. The sum of the anomalous velocity stays finite over all occupied bands, highlighting a contribution to the Hall conductivity. Furthermore, this signal stays independent of the scattering rate and, correspondingly, the longitudinal conductivity. It is therefore referred to as the *intrinsic* anomalous Hall effect. Using the TKNN formula for Hall conductivity (Eq. 1.31), one can depict the Berry curvature as an effective magnetic field, generating a finite Hall signal and contributing to Hall conductivity:

$$\frac{d\langle \boldsymbol{r} \rangle}{dt} = \frac{\partial E}{\hbar \partial \boldsymbol{k}} + \frac{e}{\hbar} \boldsymbol{E} \times (\nabla_{\boldsymbol{k}} \times A_{\boldsymbol{k}s})_z \quad 1.36$$

The problem was revisited more recently by Haldane as a "topological Fermi-liquid" property, which addresses the issue as an accumulated Berry phase by an adiabatic motion of quasiparticles only at the Fermi surface and not bulk Fermi sea [154]. Finally, a complete theoretical picture, addressing intrinsic and extrinsic anomalous Hall effects, was proposed by Nagaosa, Sinova, Onoda, Macdonald and Ong [155–157]. The intrinsic component of the anomalous Hall conductivity is directly proportional to the Berry curvature and does not depend on scattering. Furthermore, using the TKNN formula, the anomalous Hall conductivity is quantized with integer values of quantum conductance (e^2/h) in the two-dimensional limit:

$$\sigma_{xy}^{AHE-int} = -\epsilon_{ijl}\frac{e^2}{\hbar}\sum_n \int \frac{d\boldsymbol{k}}{(2\pi)^d} f\big(\epsilon_n(\boldsymbol{k})\big)(\nabla_{\boldsymbol{k}} \times A_{\boldsymbol{ks}}), \qquad 1.37$$

where ϵ_{ijl} and $f\big(\epsilon_n(\boldsymbol{k})\big)$ are the antisymmetric tensor and the Fermi-Dirac statistics with summation going through all the filled bands, n. The extrinsic anomalous Hall conductivity originates from side jump or skew scattering [156]. Side jump is the time integrated velocity deflection of electrons interacting with an impurity or disorder. Skew scattering refers to asymmetric scattering of electrons (effective TRS breaking for charge carriers) because of spin-orbit coupling to impurity atoms. The measured anomalous Hall conductivity typically contains all three components and it is challenging to distinguish them from each other.

$$\sigma_{xy}^{AHE} = \sigma_{xy}^{AHE-int} + \sigma_{xy}^{AHE-skew} + \sigma_{xy}^{AHE-sj} \qquad 1.38$$

Here, the interesting question is the conditions under which the intrinsic anomalous Hall conductivity dominates the Hall signal as only the intrinsic AHE contains information about the topology of the band structure. Three regimes and two crossovers are recognized in the case of a fixed spin-orbit coupling energy ($E_{SO} < E_F$) [155]: the clean regime with a very small scattering rate ($\hbar/\tau \leq u_{imp}E_{so}D$); the moderately dirty regime with modest scattering rate ($u_{imp}E_{so}D \leq \hbar/\tau \leq E_F$); the dirty regime ($E_F \leq \hbar/\tau$). In the clean regime, the skew scattering, which is inversely proportional to impurity density, dominates AHE signal. Here $u_{imp}$and D are the impurity potential and the density of states. Only in the second regime (moderately dirty) does the Hall conductivity become insensitive to scattering (longitudinal conductivity, σ_{xx}) due to the intrinsic Berry phase contribution, giving rise to dissipationless topological transport. Finally, a power law scaling of Hall conductivity with longitudinal conductivity is predicted in the dirty regime. Fig. 1.17 shows these three regimes with varying longitudinal conductivity (i.e. impurity density).

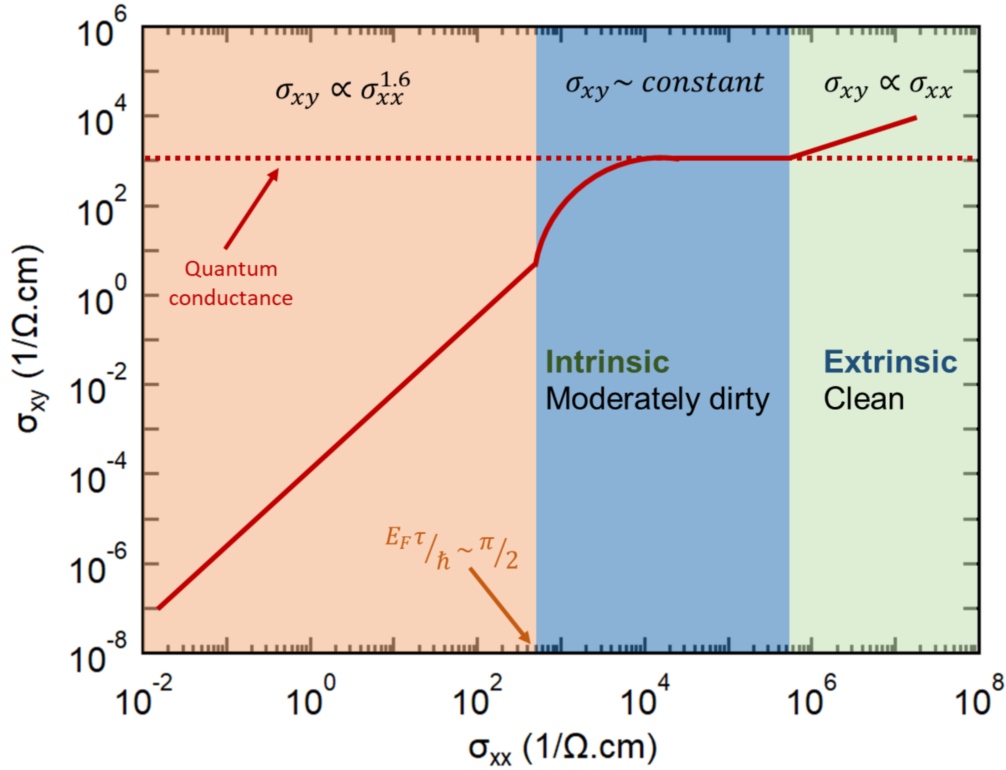

Figure 1.17. Hall conductivity with respect to longitudinal conductivity. Hall conductivity becomes insensitive to scattering (longitudinal conductivity), highlighting intrinsic dissipationelss topological transport governed by Berry curvature (adapted from Ref. [155].)

1.21.2. Topological Hall effect: Hall effect with non-trivial spin texture

Broken time-reversal symmetry and a finite Berry curvature are essential for a nonzero Hall conductivity using the TKNN formula (Eq. 1.31). In the anomalous Hall effect a significant spin-orbit interaction and a topologically nontrivial band structure were responsible for the dissipationless topological transverse current. On the other hand, band structure is not the only place to look for large Berry curvature and it was shown that an adiabatic motion of electrons in a smoothly varying magnetic field can also generate Berry curvature even in the

absence of spin-orbit coupling [158]. Here, the spin of conduction electrons couples adiabatically and acquires a Berry phase, and the effective Lorentz force is independent of spin-orbit interaction. This signal is referred to as the *topological Hall effect* (THE), to distinguish it from the anomalous Hall effect. Accordingly, here the Berry phase is from the topologically nontrivial magnetic texture and is directly proportional to the spin chirality of electrons (Fig. 1.20) [159,160].

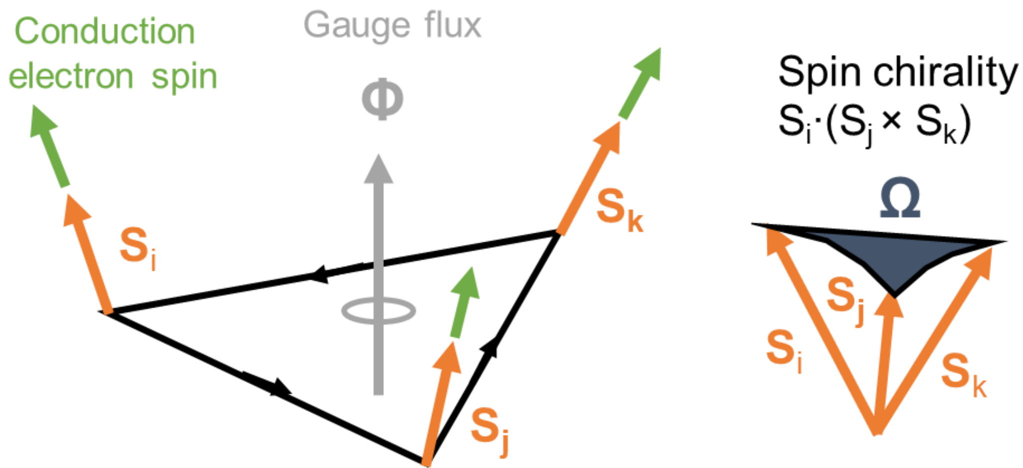

Figure 1.18. Conduction electrons moving in a smoothly varying internal magnetization couple adiabatically and accumulate Berry curvature, directly proportional to magnitude of spin chirality.

The topological Hall effect (THE) is the hallmark of topologically nontrivial (chiral) spin textures, such as skyrmions [161]. It can be understood as a distinctive contribution superimposed on the ordinary and anomalous Hall effects. The origin of THE is the “Berry phase” picked up by conduction electrons due to moving in a topologically protected spin texture [162,163]. The topological field poses an

effective magnetic field on conduction electrons in spin-polarized arisen subbands. The topological field is proportional to ($\frac{\partial \boldsymbol{n}}{\partial x} \times \frac{\partial \boldsymbol{n}}{\partial y}$) and is nonzero for non-coplanar spin textures [161]. While the Dzyaloshinskii-Moriya interaction in non-centrosymmetric crystals, such as MnSi causes skyrmions [162,164], magnetic frustration can also trigger helical structures in centrosymmetric crystals, such as $SrFe_{1-x}Co_xO_3$ and pyrochlores [165,166]. Furthermore, although, thermal spin fluctuations necessary for skyrmions in B20 non-centrosymmetric crystals, frustration could trigger skyrmion crystals SkX at 0 K [167]. In thin films, inversion symmetry may be lifted by interfaces and surfaces and motivate SkX formation [20,168].

Carrier density-controlled topologically nontrivial spin textures in oxide films and interfaces are interesting due to the possibility of exploiting electric field and proximity effects to realize other exotic states within all-epitaxial heterostructures [169].

Chapter 2. Carrier density control of Berry phases and magnetism in $EuTiO_3$

2.1. Introduction

Antiferromagnetic order has the potential to bridge topological phenomena and spintronics [170,171]. In this chapter, I will report on tuning topological states and magnetic order of doped $EuTiO_3$ thin films grown by molecular beam epitaxy. Electron-doped $EuTiO_3$ thin films show signatures of non-trivial topology in both real space spin texture (i.e. topological Hall effect) and momentum space band structure (i.e. anomalous Hall effect). Both anomalous and topological Hall effects show a strong dependence on carrier density, i.e. chemical potential. Here, carrier density is used as a knob to control anomalous and topological Hall signals. The strong dependence on the carrier concentration makes $EuTiO_3$ of potential interest for field-effect devices. It is also shown that the magnetic field can systematically control the symmetry of electronic states in doped $EuTiO_3$ thin films. The coupling between the Néel vector orientation and underlying symmetries is studied using anisotropic magnetoresistance (AMR). Finally, formation of a two-dimensional electron system is shown at $SmTiO_3$ /$EuTiO_3$ interface. Here, the two-dimensional electron system shows signatures of topologically nontrivial structure beyond antiferromagnetic ordering temperature of $EuTiO_3$. The results open interesting possibilities for epitaxial heterostructures that combine topological states, tunable antiferromagnetic ordering, and other phenomena.

2.2. Growth and structural characterization

Sm-doped $EuTiO_3$ thin films were grown epitaxially on (001) $(La_{0.3}Sr_{0.7})(Al_{0.65}Ta_{0.35})O_3$ (LSAT) single crystals using MBE. Elemental Eu and TTIP, were used to supply Eu, Ti, and oxygen. The MBE growth procedure is similar to that previously used for $SrTiO_3$ [48,172], except that no extra oxygen was provided. A thin $SmTiO_3$ film was grown on top of $EuTiO_3$ for two-dimensional electron system study. Electron beam evaporation through a shadow mask was used to deposit Au/Ti (400/40 nm) contacts for Hall and sheet resistance (R_s) measurements using square Van der Pauw structures. Temperature (T) dependent magnetotransport measurements were carried out using a Quantum Design Physical Property Measurement System (PPMS). Magnetic properties were measured using a Quantum Design 5XL MPMS superconducting quantum interface device (SQUID) magnetometer. A Hall bar structure was fabricated for measuring anisotropic magnetoresistance with the current parallel to [100] and [110] crystallographic directions. Reflection high-energy electron diffraction (Staib Instruments, Germany) was used to monitor the growth *in-situ*. Fig. 2.1. shows the reflection high-energy electron diffraction (RHEED) of a $EuTiO_3$ film along the [100] and [110] azimuths. The surface reconstruction is similar to the previously reported c(4×4) reconstruction for stoichiometric $SrTiO_3$ [173].

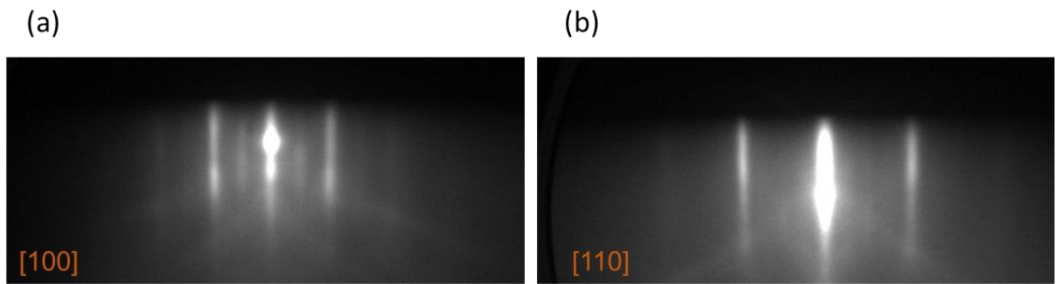

Figure 2.1. *In-situ* characterization of $EuTiO_3$ during growth. Reflection high-energy electron diffraction of the $EuTiO_3$ film in (a) [100] and (b) [110] azimuths.

Figure 2.2 shows an x-ray diffraction (XRD) scan around the 001 reflections of the $EuTiO_3$ film and the LSAT substrate. The film is single-phase and the thickness fringes indicate a smooth film of high structural quality.

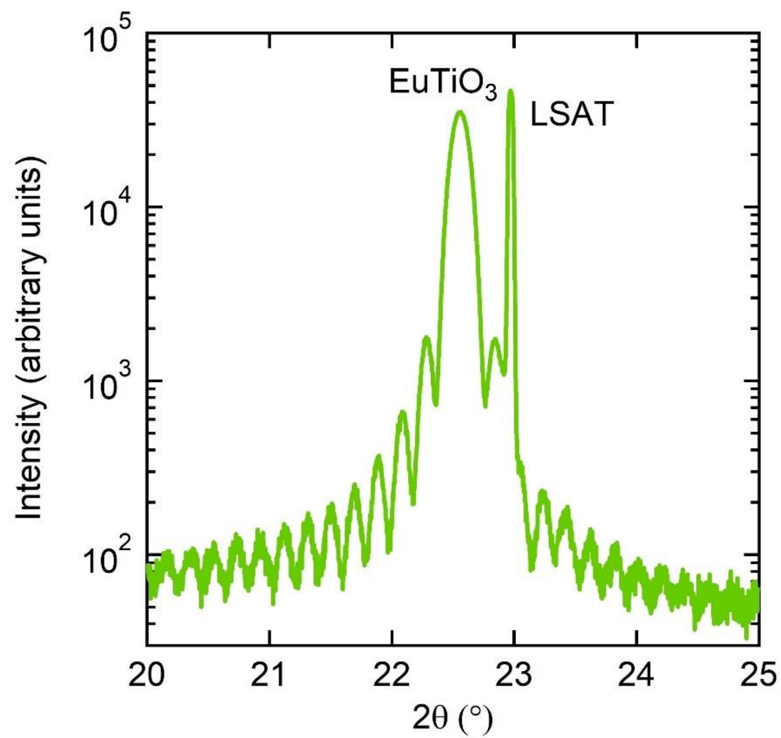

Figure 2.2. XRD pattern of an $EuTiO_3$ thin film grown on a (001) LSAT substrate.

A combination of x-ray diffraction and reflection high-energy electron diffraction was used to calculate the thickness and growth rate of the films. The final thickness was also verified by the Laue's thickness fringes from x-ray diffraction and cross section scanning transmission electron microscopy imaging. Reciprocal space mapping (RSM) was carried out near the 113_{pc} reflection for $EuTiO_3$ films on LSAT and used to determine the in- and out-of-plane lattice parameters of the substrate and film. Fig. 2.3 shows the RSM results for the LSAT/$EuTiO_3$ heterostructure. The axes denote the in-plane (q_x) vectors and out-of-plane (q_z) lattice vectors, scaled as $2\pi/a$, where a is the real-space lattice constant of the respective planes. The reciprocal space mapping confirms that the in-plane lattice of the $EuTiO_3$ film is coherently strained to the LSAT substrate (a= 0.3868 nm). The in-plane strain ($\varepsilon = \frac{a_{\parallel}-a_0}{a_0}$) can be estimated as ~-1%, where $a_{\parallel}$ is the in-plane lattice constant of strained $EuTiO_3$ (3.868 Å) and a_0 is the lattice constant of relaxed single-crystal $EuTiO_3$ (3.90 Å).

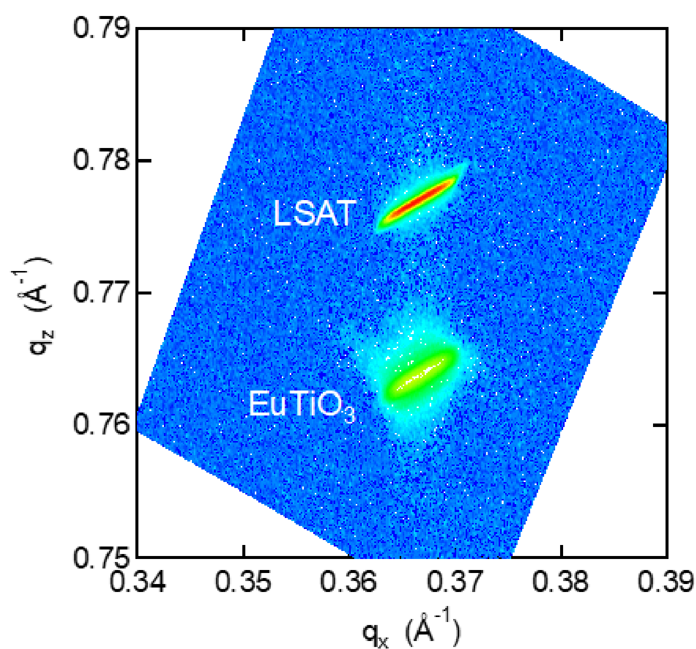

Figure 2.3. Reciprocal space mapping of LSAT/$EuTiO_3$ heterostructure carried out near the 113_{pc} reflection for a $EuTiO_3$ film.

Cross section samples of the heterostructure were used for high angle annular dark-field (HAADF) imaging in scanning transmission electron microscopy (STEM). Samples were prepared using a focused ion beam (FEI Helios Dualbeam Nanolab 650) and imaged using an FEI Titan S/TEM operated at 300 kV, with a convergence angle of 9.6 mrad. Fig. 2.4 shows a HAADF-STEM image, carried out by Salva Salmani-Rezaie, indicating the film to have high structural perfection with an atomically sharp interface between the LSAT substrate and Sm: $EuTiO_3$ film.

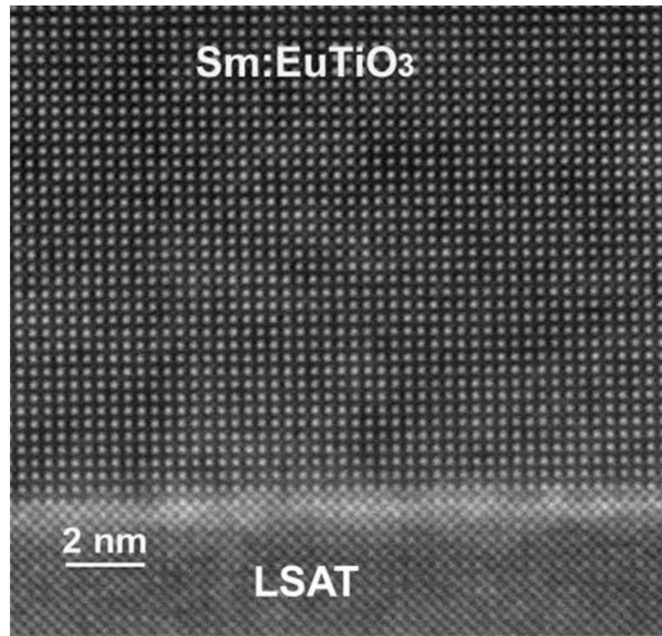

Figure 2.4. Cross-section HAADF-STEM image of Sm:$EuTiO_3$ film grown on LSAT, confirming an atomically sharp and uniform interface between film and substrate (courtesy of Salva Salmani-Rezaie).

Figure 2.5 shows neutron diffraction results for three samples with different Sm concentrations (carried out by Zach Porter). Here magnetic Bragg peaks at tetragonal [odd, 0, odd] (pseudocubic [1/2 1/2 1/2]-type) indices were observed below the Néel temperature in all samples. The mean-field fit highlights the antiferromagnetic order parameter. Here, the results shows the magnetic exchange interaction to be independent of carrier density, contradicting the previously reported Ruderman-Kittel-Kasuya-Yosida (RKKY) antiferromagnetic-ferromagnetic transition with doping concentration [21,174].

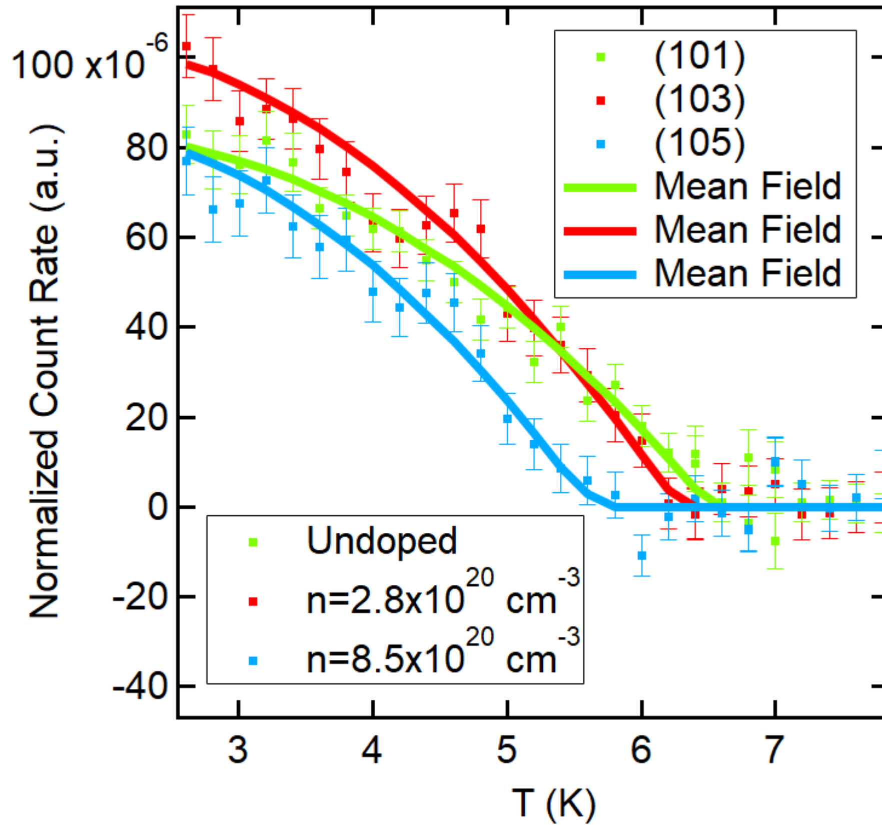

Figure 2.5. Neutron diffraction intensities with temperature for Sm doped $EuTiO_3$ thin films at the magnetic [1 0 L] reflections. Here the incoherent background is removed, and intensities are normalized by the reflection intensity of the [103] substrate (Courtesy of Zach Porter and Stephen Wilson).

2.3. Magnetoelectric measurements

The Hall carrier density was measured as a function of temperature (2-400 K) for samples with various Sm concentrations. There is a small charge carrier freeze out.

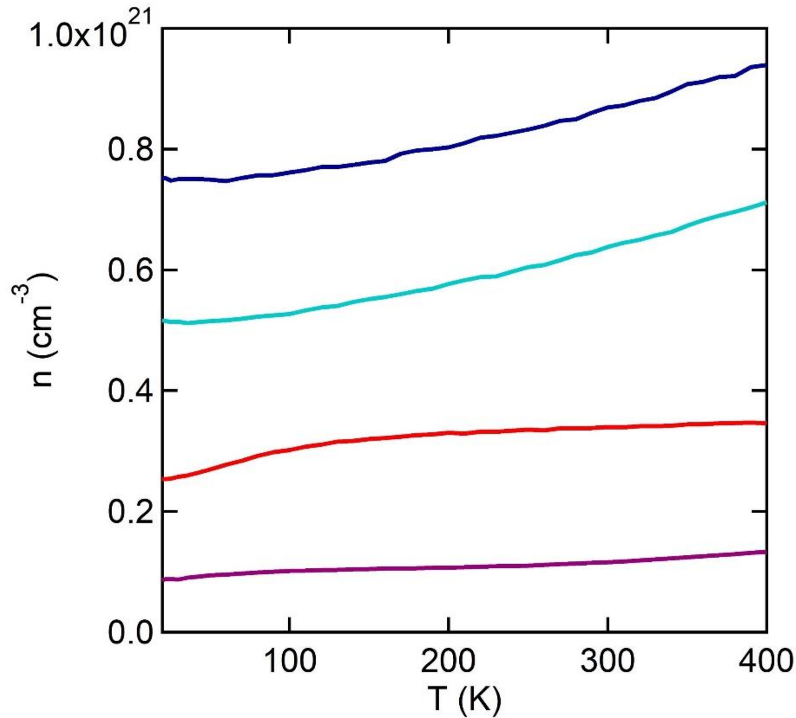

Figure 2.6. Carrier concentration vs. temperature for Sm-doped $EuTiO_3$ thin films with various carrier densities.

Figure 2.7 and 2.8 show the sheet resistance as a function of temperature for $EuTiO_3$ films with various Sm concentrations. The $EuTiO_3$ films show metal-to-insulator transition with Sm doping. While the undoped $EuTiO_3$ film is highly resistive and quickly exceeds the measurement limit below room temperature, the doped samples ($n_{300K} = 1.2, 3.4, 6.5, \text{and } 8.7 \times 10^{20} \text{cm}^{-3}$) show metallic behavior ($\mathrm{d}R_s/\mathrm{d}T > 0$) down to helium liquid temperature. All doped samples show a relatively sharp peak in resistance at ~ 6 K without applied magnetic field. An upturn in R_s emerges at ~30 K followed by a sharp drop at ~ 6 K. Similar behavior was reported previously for La [19] and Nb [24]-doped $EuTiO_3$, and is because of

the alignment of the localized Eu 4*f* spins, which lowers scattering and resistivity of conduction band electrons. The resistance peak temperatures (Fig. 2.8) match the onset of antiferromagnetic order parameter in neutron diffraction mean-field fit (Fig. 2.5).

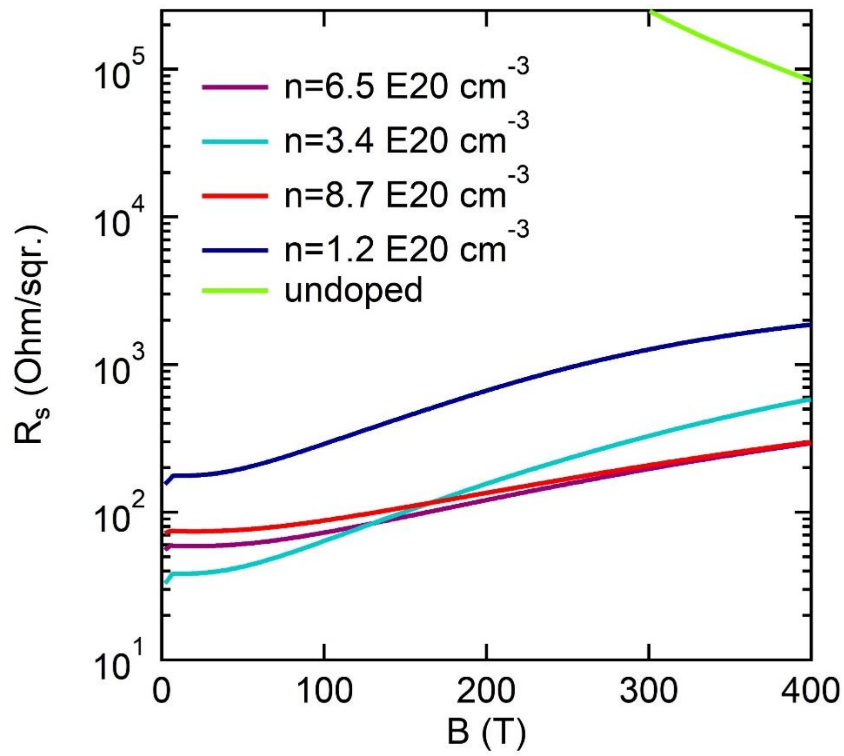

Figure 2.7. Sheet resistance as a function of temperature for doped and undoped $EuTiO_3$ thin films.

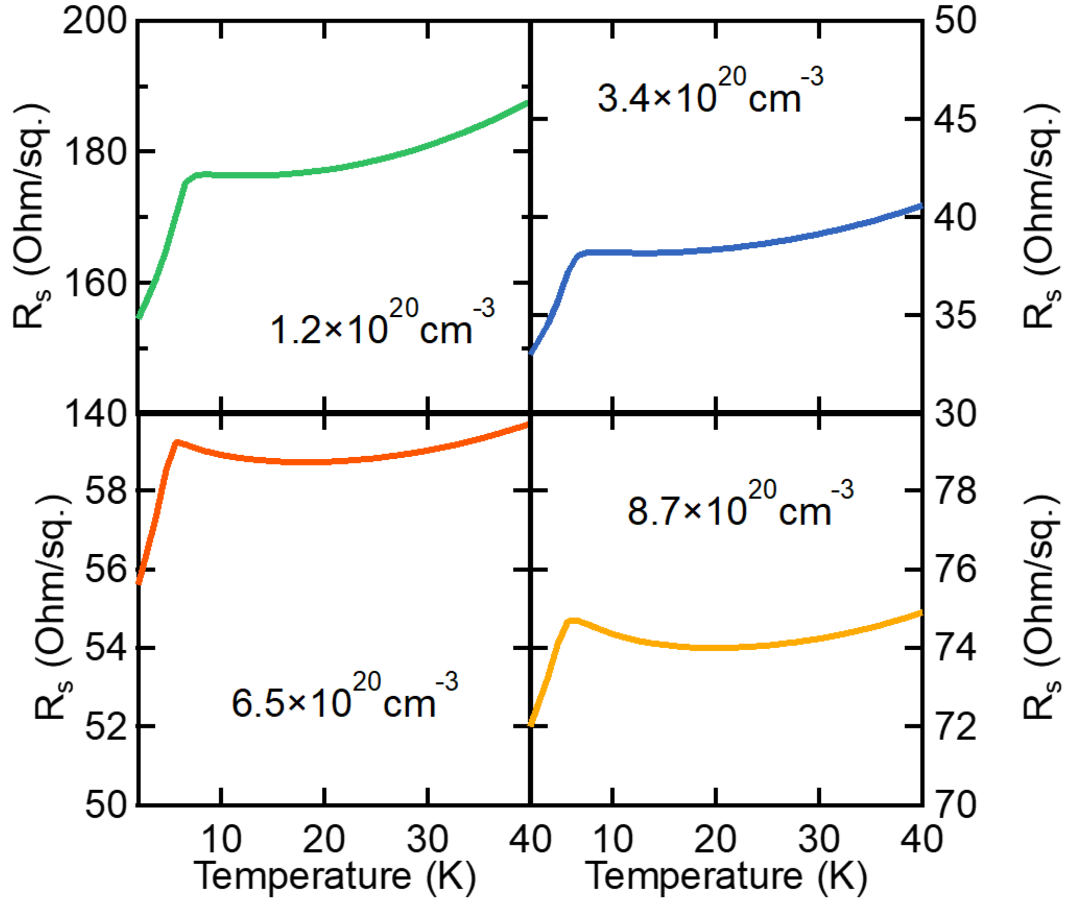

Figure 2.8. Sheet resistance vs. temperature for electron doped $EuTiO_3$ thin films with different carrier densities.

Figure 2.7 (a-d) shows R_{xx} vs. B (longitudinal magnetoresistance) for the doped $EuTiO_3$ films ($n_{RT} = 1.2, 3.4, 6.5, \text{and } 8.7 \times 10^{20}\text{cm}^{-3}$) at 2 K, 5 K, 10 K and 15 K. Here, B was swept from +6 T to -6 T and back. The heavily doped $EuTiO_3$ film ($n_{RT} = 8.7 \times 10^{20}\text{cm}^{-3}$) shows a negative magnetoresistance with a prominent hysteresis. The hysteresis shrinks with decreasing carrier concentration

($n_{RT} = 6.5 \times 10^{20}\text{cm}^{-3}$) and disappears completely for $n_{RT} = 1.2$ and $3.4 \times 10^{20}\text{cm}^{-3}$. Furthermore, the disappearance of hysteresis is concurrent with the occurrence of a pronounced positive magnetoresistance at low magnetic fields.

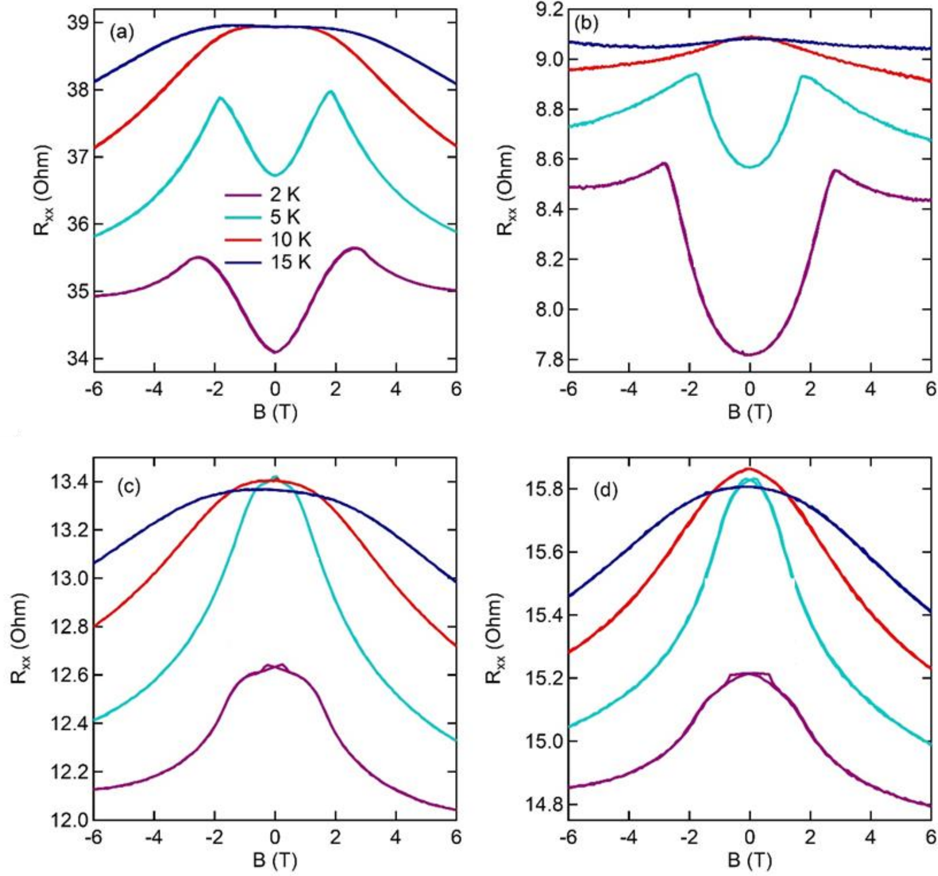

Figure 2.9. (a), (b), (c), and (d) shows the magnetoresistance of the doped $EuTiO_3$ with n_{RT}=1.2, 3.4, 6.5, and 8.7×10^{20} cm^{-3}) carrier densities, respectively, at 2 K, 5 K, 10 K, and 15 K.

The positive magnetoresistance is more prominent closer to the transition (~10%) and expands up to 2.8 T out-of-plane magnetic field at 2 K. The magnetic field range for positive magnetoresistance shrinks systematically with increasing component of in-plane magnetic field. Figure 2.8 shows R_{xx} as a function of the applied magnetic field, for various orientations of B. Here, θ is the angle between B and the film normal. With increasing θ, the in-plane component of B pushes the metamagnetic transition to smaller values.

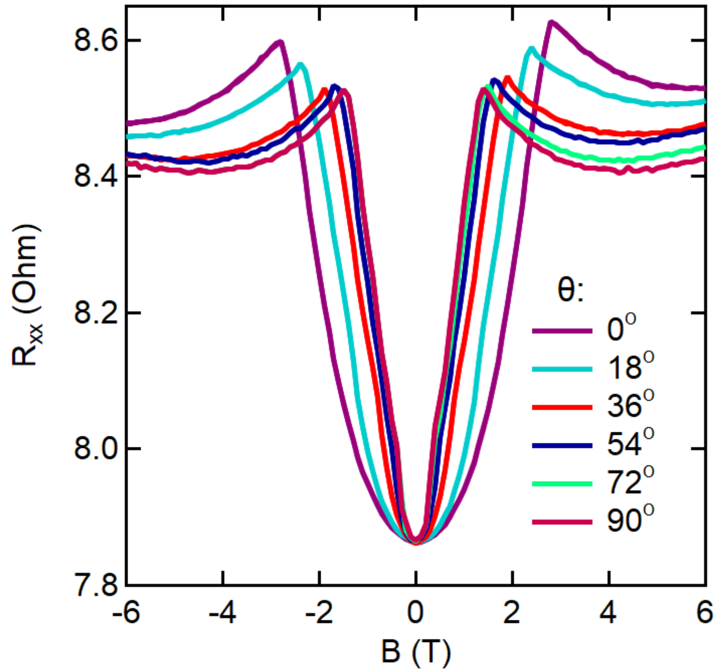

Figure 2.10. Longitudinal magnetoresistance as a function of magnetic field, for various orientations of B for $n_{300K}=3.4\times10^{20}$ cm^{-3} at 2 K.

The magnetoresistance in Fig. 2.9(a-b) and 2.10 is reminiscent of metamagnetism [175]. In a metallic system, the metamagnetic transition is a

characterized as a crossover or phase transition from a less magnetically polarized state to a higher magnetic polarization with increasing magnetic field. In insulating systems, the transition is believed to be an ordered antiferromagnet at low fields becoming ferromagnetically ordered at higher fields through "spin-flip" or "spin-flop" reorientations. Presence of a spin-flopped antiferromagnet has previously been reported in undoped $EuTiO_3$, below 5 K [176].

Figure 2.11 shows the AHE and THE contributions for the doped $EuTiO_3$ films with different carrier concentrations ($n_{RT} = 1.2, 3.4, 6.5,$ and $8.7 \times 10^{20} \mathrm{cm}^{-3}$) at $T = 2$ K. The raw Hall data was antisymmetrized to eliminate the longitudinal magnetoresistance, i.e., $R_{xy} = \left[R_{xy}{}^{raw}(+B) - R_{xy}{}^{raw}(-B) \right] / 2$. The linear fit at high applied magnetic fields (6 – 9 T) yields the ordinary Hall component (R_0B). In the presence of an AHE and/or a THE, R_{xy} is given by: $R_{xy} = R_0 H + R_{AHE} + R_{THE}$, where R_{AHE} and R_{THE} are the AHE and any THE (if present) contributions, respectively [155,177]. Subtracting the ordinary Hall component (R_0B) from R_{xy} yields the AHE and THE contributions, i.e. $R_{AHE} + R_{THE}$.

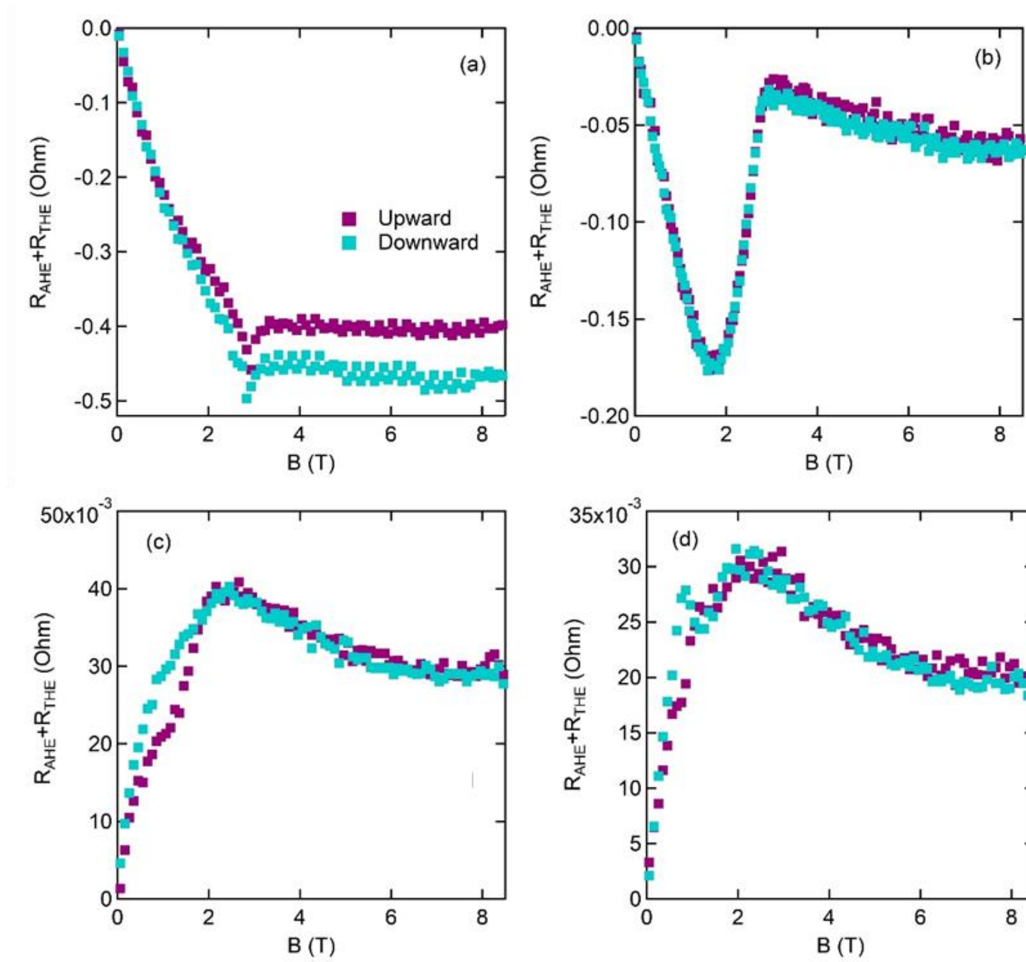

Figure 2.11. The difference between antisymmetric and normal Hall component (R_0B) of the doped $EuTiO_3$ with n_{RT}=1.2, 3.4, 6.5, and 8.7×10^{20} cm^{-3} carrier densities, respectively, at 2 K.

At higher temperatures (5 k, 10 K, and 15 K), the monotonic increase in the resistivity with B is characteristic of the conventional AHE [177]. Figure 2.12 shows extracted AHE and THE components from Hall measurements as a function of the out-of-plane applied magnetic field at various temperatures. Here, THE (peak

in resistance at ~2 T) only appears at 2 K, and at higher temperatures, i.e. 5 K, 10 K, and 15 K, only AHE (monotonic resistance with magnetic field) is observed.

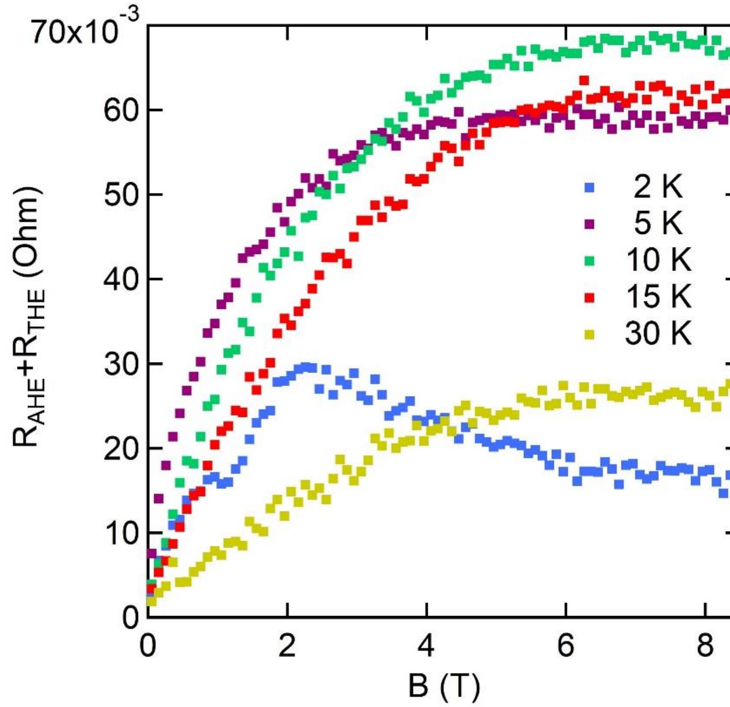

Figure 2.12. THE and AHE components after subtraction of the linear Hall component (R_0B) for n_{RT}=8.7×10^{20} cm^{-3} at 2 K, 5 K, 10 K and 15 K with respect to out-of-plane B component at different B orientations.

These films are in the regime of ρ>10^{-4} Ω cm, which makes the AHE to be dominated by the intrinsic, Berry phase contribution [155]. Figure 2.13 shows the σ_{xx} and σ_{xy} at 2 K and 5 K for different carrier concentrations, calculated from the respective resistivities, assuming negligible out-of-plane transport.

$$\sigma_{xx} = \frac{\rho_{xx}}{\rho_{xx}^2+\rho_{xy}^2} \quad 2.1$$

$$\sigma_{xy} = \frac{-\rho_{xy}}{\rho_{xx}^2+\rho_{xy}^2} \quad 2.2$$

σ_{xx} and σ_{xy} are ~ $10^4\ \Omega^{-1}cm^{-1}$ and $10^3\ \Omega^{-1}cm^{-1}$, respectively, which are considered to fall inside the regime where the Hall resistance is dominated by intrinsic phenomena [155,178,179]. Furthermore, σ_{xy} does not depend on σ_{xx} for the carrier densities through the cross-over behavior in the AHE. These observations suggest that the AHE is in the dissipationless regime where the intrinsic Berry curvature dominates AHE behavior [178].

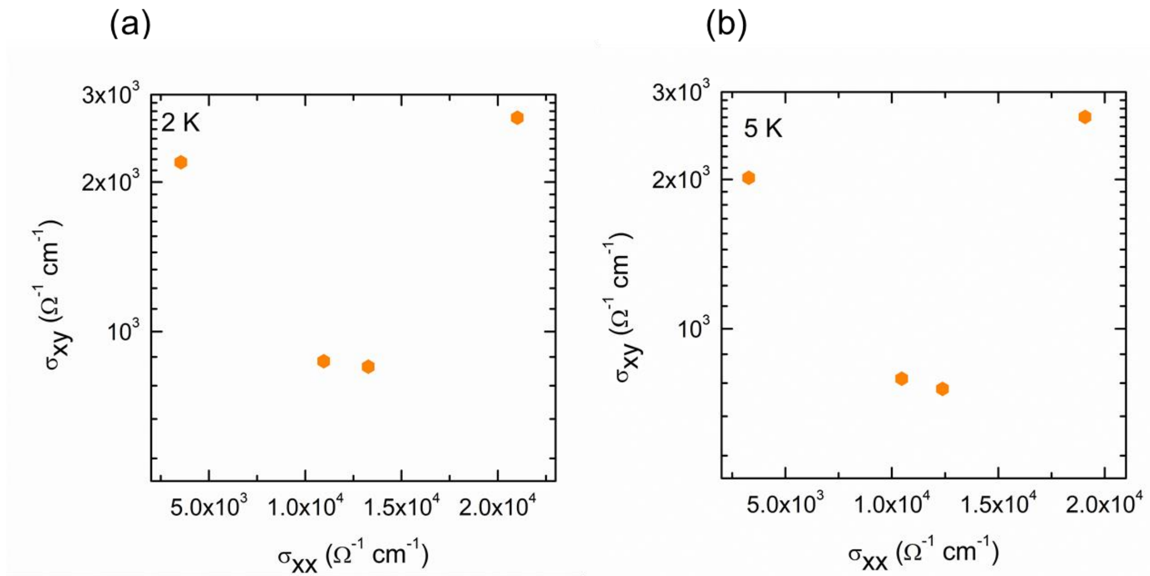

Figure 2.13. σ_{xy} as a function of σ_{xx} at different carrier concentrations (the data points, from left to right, correspond to n_{300K}=1.2×10^{20} cm^{-3}, 6.4×10^{20} cm^{-3}, 8.7×10^{20} cm^{-3}, and 3.4×10^{20} cm^{-3} at (a) 2 K and (b) 5 K, respectively.

The peak on top of anomalous Hall effect is attributed to topological Hall. Here, the sample with $n_{RT} = 1.2 \times 10^{20}\text{cm}^{-3}$ shows a very small onset of THE. As the carrier concentration increases to $3.5 \times 10^{20}\text{cm}^{-3}$, i.e. getting closer to the AHE and THE sign change, the THE component becomes dominant compared to the AHE signal. Further increase of the carrier concentration triggers a sign change in both the AHE and the THE. The AHE sign change with carrier concentration has been reported in La doped $EuTiO_3$ at $n \cong 2.5 \times 10^{20}\text{cm}^{-3}$ [22]. A concurrent THE and AHE sign change with doping concentration was reported for $Mn_{1-x}Fe_xSi$ [180]. While the origin of sign change is not clear in $Mn_{1-x}Fe_xSi$, the reduction in the THE peak magnitude is associated with the increase of the skyrmion helical wavelength. More heavily doped samples ($n_{RT} = 6.5$ and $8.7 \times 10^{20}\text{cm}^{-3}$) show two peaks with a smaller magnitude compared to lighter doped samples. The peak at ~0.8 T (stronger in upward than downward sweep) is near the field at which the closure of the hysteresis is seen in the magnetoresistance data shown in Fig. 2.9(c) and (d). A second, more pronounced peak at ~ 2T has no corresponding feature in the magnetoresistance. EuO thin films show a similar THE peak at ~ 2 T which can be suppressed with in-plane applied magnetic field [20]. These general features are very similar to the THE signal found in a wide range of other materials with skyrmions [20,161,164].

Figure 2.14(a) shows the proposed phase diagram for Sm-doped $EuTiO_3$ with an out-of-plane magnetic field and a carrier concentration at 2 K. The phases on the bottom of the graph show the THE, and accordingly a topologically non-

trivial spin texture. While the dilute samples show metamagnetism, the over-doped samples show the expected negative magnetoresistance with hysteresis. AHE and THE signals show similar trend with carrier density might, i.e. sign change at $n \cong 4 \times 10^{20}\mathrm{cm}^{-3}$, suggesting the possibility of similar origin (e.g. momentum space Berry curvature) for both signals. The sign change in AHE could be a signature for Fermi surface crossing a Weyl node [181]. DFT calculations, carried out by Z. Gui and A. Janotti, also confirm the Fermi surface crossing a Weyl node for a carrier concentration between 3.4×10^{20} and 6.2×10^{20} cm^{-3} (Fig. 2.14(b)).

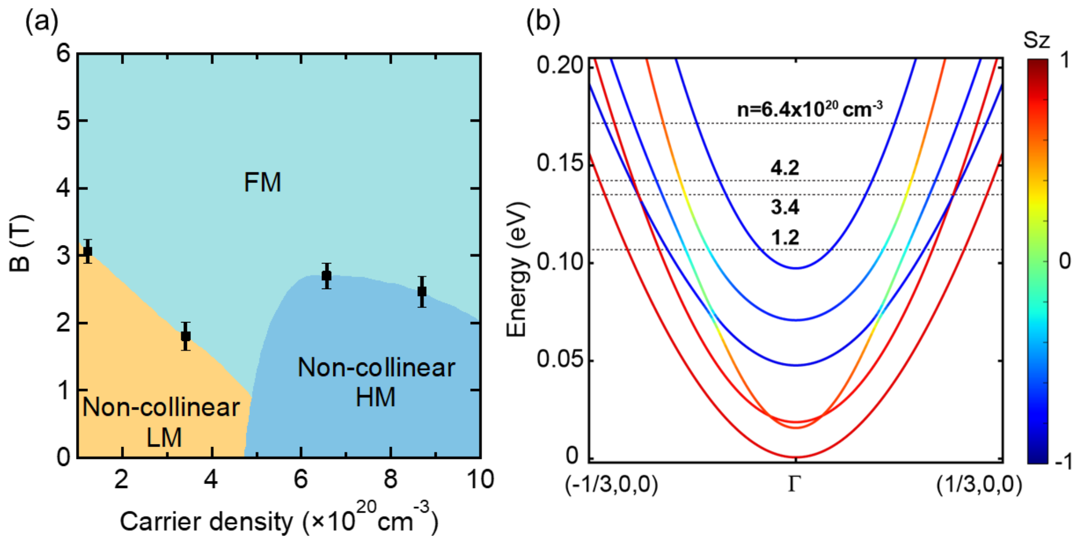

Figure 2.14. (a) The proposed phase diagram for electron-doped $EuTiO_3$ with carrier concentration (n_{RT}=1-10×10^{20} cm^{-3}) and out-of-plane magnetic field (0-6 T) at 2 K. (b) Band structure for electron-doped $EuTiO_3$ along Γ-X. The colored lines show z-component of spin (Courtesy of Zhigang Gui and Anderson Janotti).

Fermi surface crossing a Weyl node causes a sign change in AHE, as a result, the sign and magnitude of AHE depends strongly on energy and momentum of the nodes. It is known that applied magnetic field can move Weyl nodes around (momentum and energy of the nodes), causing a more complicated transverse signal with magnetic field since, AHE also depends strongly on the momentum difference between Weyl nodes [182]. If true, the extra peak in Fig. 2.11 may not be a THE and could be a *nonlinear* AHE due to complicated interplay between magnetic field and relative momentum and energy of the Weyl nodes. The main argument against this hypothesis is wide range of carrier concentrations (~30 meV in term of Fermi energy) in which similar AHE behavior is observed which is much larger than magnetic Zeeman energy applied.

Another argument against nonlinear AHE is that the extra peak in Fig. 2.12 only appears at 2 K, while the AHE extends up to higher temperatures, suggesting different origins for two signals. Here, the THE peak disappears around magnetic ordering temperature Fig. 2.12. Recent neutron diffraction with magnetic field also confirms emergence of a ferromagnetic ordering at similar fields in which THE abruptly disappears in Fig. 2.11 [183]. Additionally, the THE vanishes with an in-plane applied field, highlighting a two-dimensional spin texture origin for this signal. Figure 2.15 shows the AHE and the THE components of Hall measurements as a function of the out-of-plane magnetic field component, $B\cos\theta$, for various orientations of applied magnetic field. Here, θ is the angle between magnetic field and the film normal. With increasing θ, the in-plane component of magnetic field

suppresses the THE, suggesting a two-dimensional spin texture origin for THE signal.

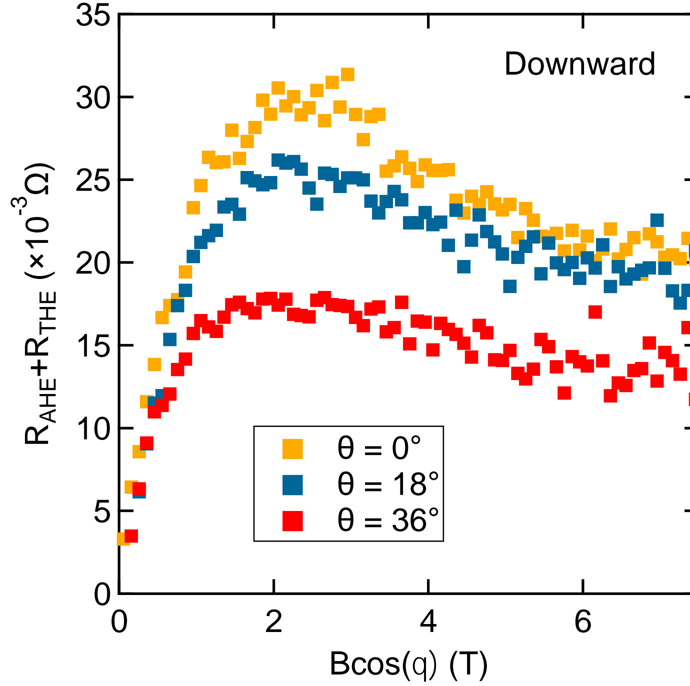

Figure 2.15. THE and AHE components of Hall experiment for n_{RT}=8.7×10^{20} cm^{-3} at 2 K with respect to out-of-plane magnetic field component at different applied magnetic field orientations.

Figure 2.15 and 2.16 show the superconducting quantum interference device (SQUID) magnetometry for doped $EuTiO_3$ with $n_{RT} = 3.4 \text{ and } 6.5 \times 10^{20}\text{cm}^{-3}$. Figure 2.14 shows the field cooling (100 Oe) results for two samples near the crossover ($n_{RT} = 3.4 \text{ and } 6.5 \times 10^{20}\text{cm}^{-3}$). The over-doped $EuTiO_3$ shows larger magnetism.

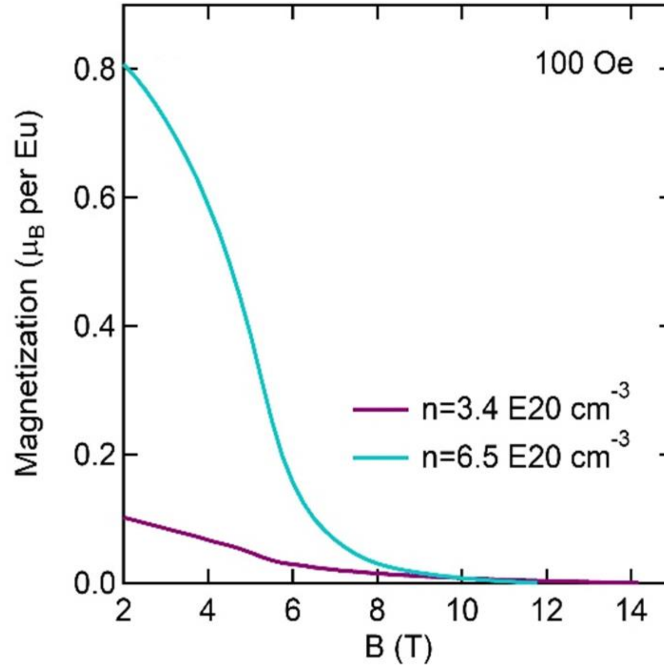

Figure 2.16. Magnetometry with field cooling (100 Oe) for doped $EuTiO_3$.

Fig. 2.15. shows presence of a hysteresis at 2 K, confirming the magnetoresistance data for the over-doped sample. Surprisingly, it also shows a very small hysteresis for $n_{RT} = 3.4 \times 10^{20}\text{cm}^{-3}$ which is not seen in the magnetoresistance data. Here, magnetism shows carrier density dependence. Neutron diffraction results confirm an antiferromagnetic ordering of Eu^{2+} 4f spins with similar Néel temperature regardless of carrier density in $EuTiO_3$, suggesting the change in magnetization observed here cannot be a simple RKKY effect. Additionally, the magnitude of enhancement in magnetization (~0.7 μ_B per Eu) is not proportional to change in density of conduction electrons between two samples ($3.1\ \times 10^{20}\text{cm}^{-3}$).

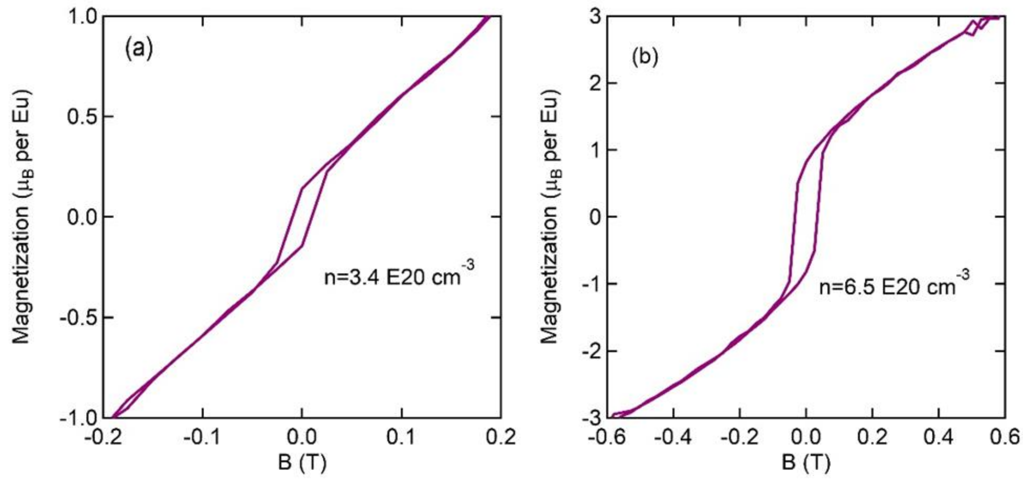

Figure 2.17. Magnetic hysteresis for electron doped $EuTiO_3$ films with carrier densities of (a) 3.4×10^{20} cm^{-3} and (b) 6.5×10^{20} cm^{-3}.

Figure 2.18 is calculated from resistivity measurements at 2-5 K with various magnetic fields (0-9 T). The data is interpreted using the general expression for temperature dependence of resistance, $R(T) = R_0 + AT^n$. The natural logarithm of the derivative of resistance with respect to temperature is used for the fitting, ($Log(\frac{dR(T)}{dT}) = Log(nA) + (n-1)Log(\mathrm{T})$). The slope of the graph is used independently to extract the "n", and knowing "n", "A" can be resolved from the intercept. "A" is directly proportional to carrier mass. The significant enhancement of "A" suggests carrier mass enhancement and possibility of a magnetic field quantum critical point.

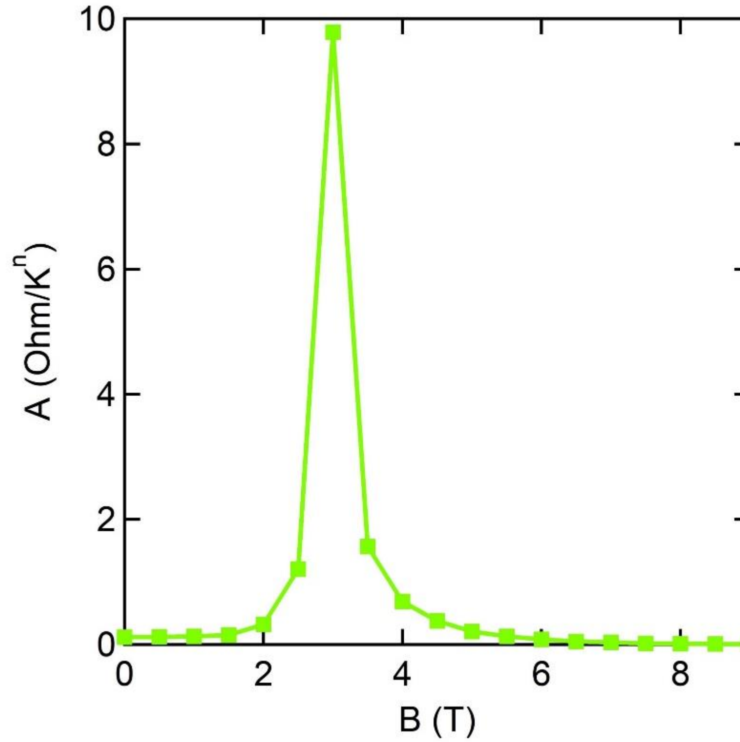

Figure 2.18. Temperature-independent coefficient from general transport expression of $R(\mathrm{T})=R_0+\mathrm{A}T^n$ as function of out-of-plane applied magnetic field.

2.4. Anisotropic magnetoresistance (AMR)

A Hall bar structure was fabricated for measuring anisotropic magnetoresistance (AMR) with the current parallel to [100] and [110] crystallographic directions (Fig. 2.19(a)). Here, the applied magnetic field is kept parallel to the film and theta is the in-plane angle between the current and applied magnetic field (Fig. 2.19(b)). AMR measurements capture relative change of resistivity with respect to theta. The measurements were carried out at 2 K and sample used for this experiment showed carrier concentration and mobility of $n_{2K} = 2.2 \times 10^{20}\mathrm{cm}^{-3}$ and $\mu_{2K} = 211\ \mathrm{cm}^2/\mathrm{V\ s}$, respectively.

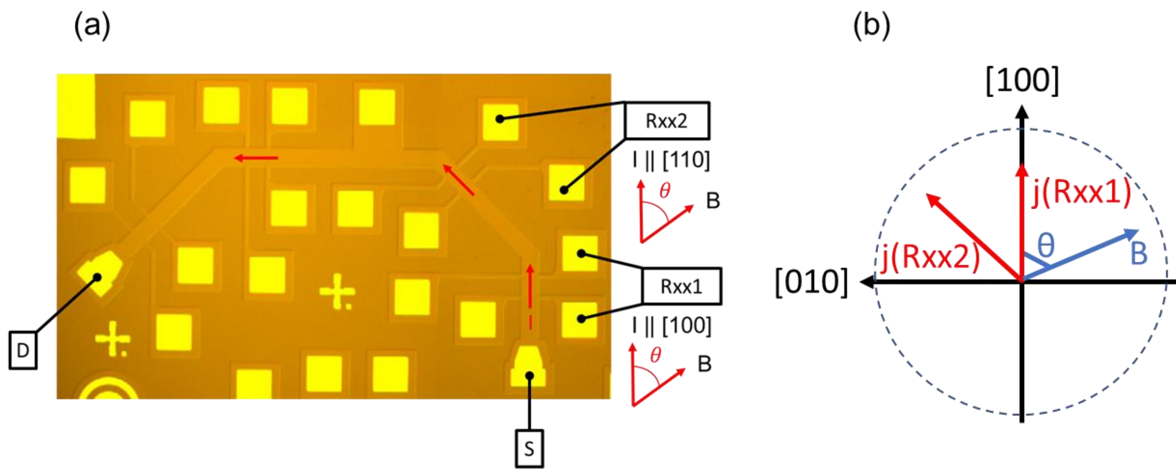

Figure 2.19. (a) Top view of the AMR experiment Hall bar and (b) AMR experiment geometry.

Figure 2.20 shows anisotropic magnetoresistance for half rotation. At low fields (up to 0.3 T), the resistance stays insensitive to the angle between the current and the in-plane magnetic field. A four-fold AMR emerges for larger magnetic fields (0.4 T<*B*<0.75 T) with maximum resistance for magnetic field parallel to [100] and [010] crystallographic directions. At *B*~0.8 T, resistance again becomes insensitive to the applied magnetic field direction, followed by the formation of another four-fold AMR at larger fields (*B*=0.9 T and 1 T). The maximum resistance now happens for magnetic field parallel to <110> crystallographic directions, highlighting a 45° rotation in the four-fold AMR compared to lower fields. Figure 2.21 (b) shows the AMR results for higher magnetic fields (1-2 T). Here, resistance peaks, parallel to <110> crystallographic directions at lower fields (*B*=1 T), show a systematic shift twoards the [010] direction with increasing magnetic field. A

two-fold AMR, with maximum resistance parallel to [010] crystallographic direction, emerges at 2 T.

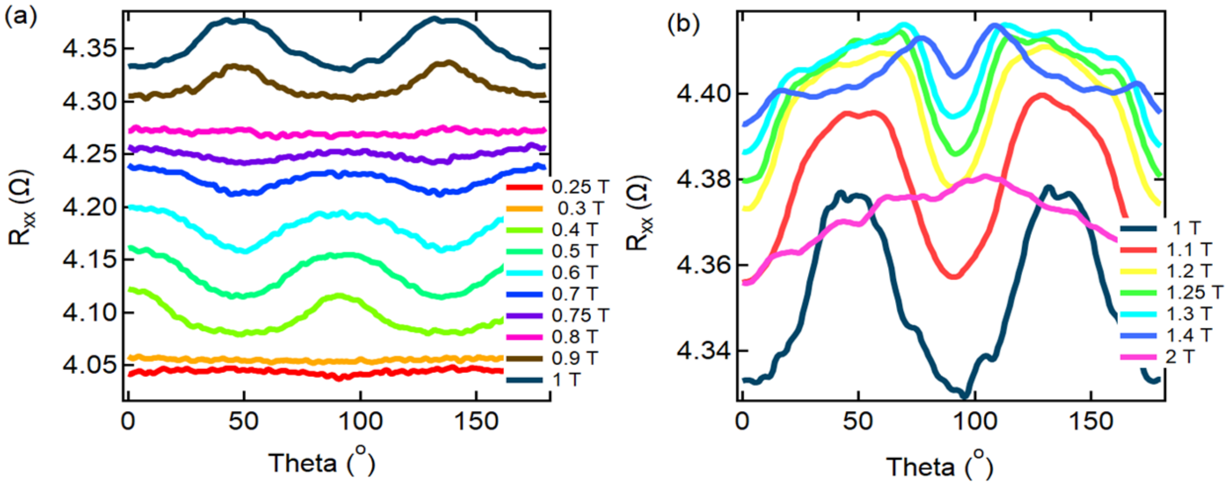

Figure 2.20. AMR results for various in-plane applied magnetic fields (0.25 T, 0.3 T, 0.4 T, 0.5 T, 0.6 T, 0.7 T, 0.75 T, 0.8 T, 0.9 T, 1 T, 1.1 T, 1.2 T, 1.25 T, 1.3 T, 1.4 T and 2 T) for half rotation.

Figures 2.21 and 2.22 show the anisotropic magnetoresistance symmetry evolution at 0.5 T, 1 T, 1.3 T and 2 T using polar graphs for a full rotation with current parallel to the [100] and the [110] crystallographic directions, respectively.

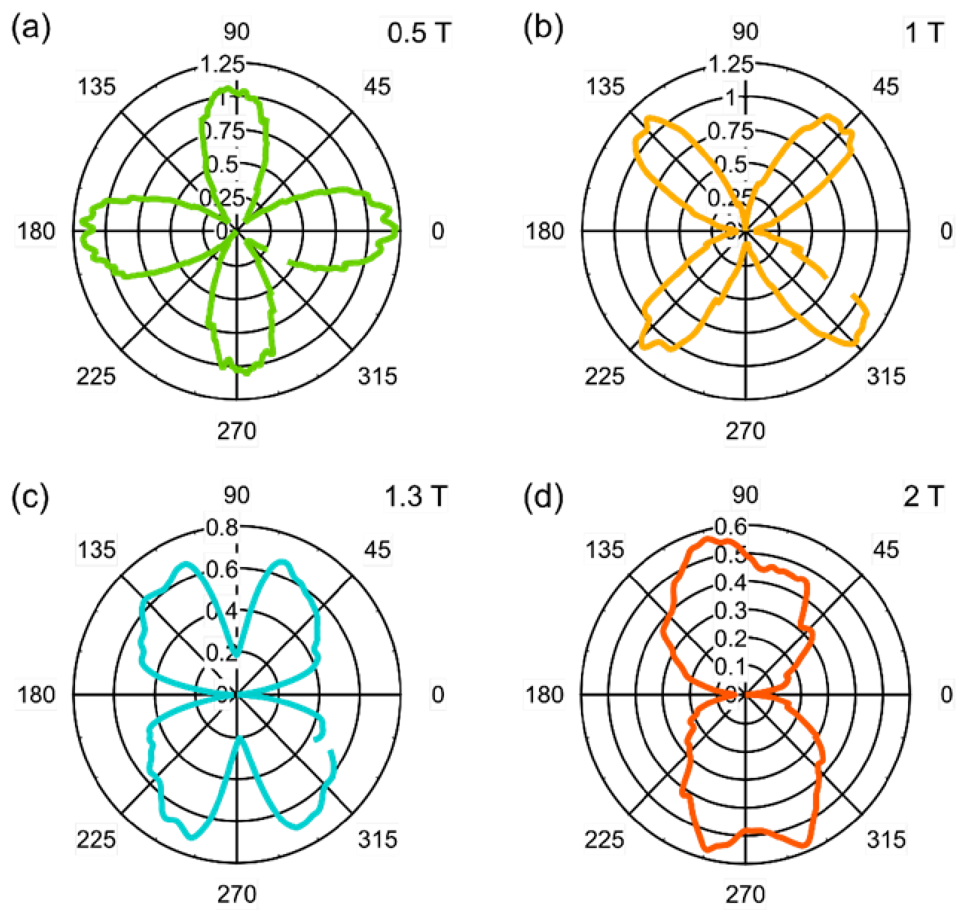

Figure 2.21. Anisotropic magnetoresistance results with polar graphs at (a) 0.5 T, (b) 1 T, (c) 1.3 T, and (d) 2 T with current parallel to [100] crystallographic direction.

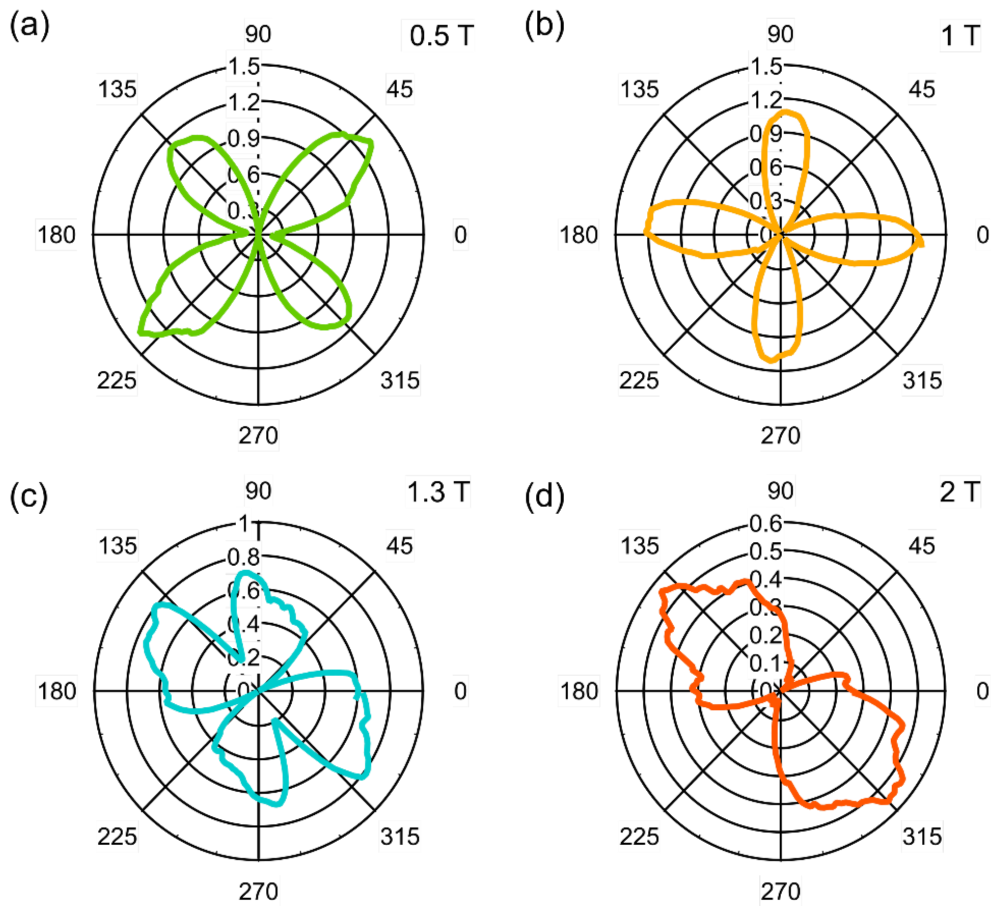

Figure 2.22. Anisotropic magnetoresistance results with polar graphs at (a) 0.5 T, (b) 1 T, (c) 1.3 T, and (d) 2 T with current parallel to [110] crystallographic direction.

Increasing the field, the four-fold AMR weakens and completely disappears at B=0.8 T and reemerges with 45° rotation at higher fields. To further study the disappearance and reappearance of four-fold AMR with 45° rotation, the band structure was investigated using DFT calculations, carried out by X. Lu and J. Rondinelli, with respect to the neighboring Eu spin orientation.

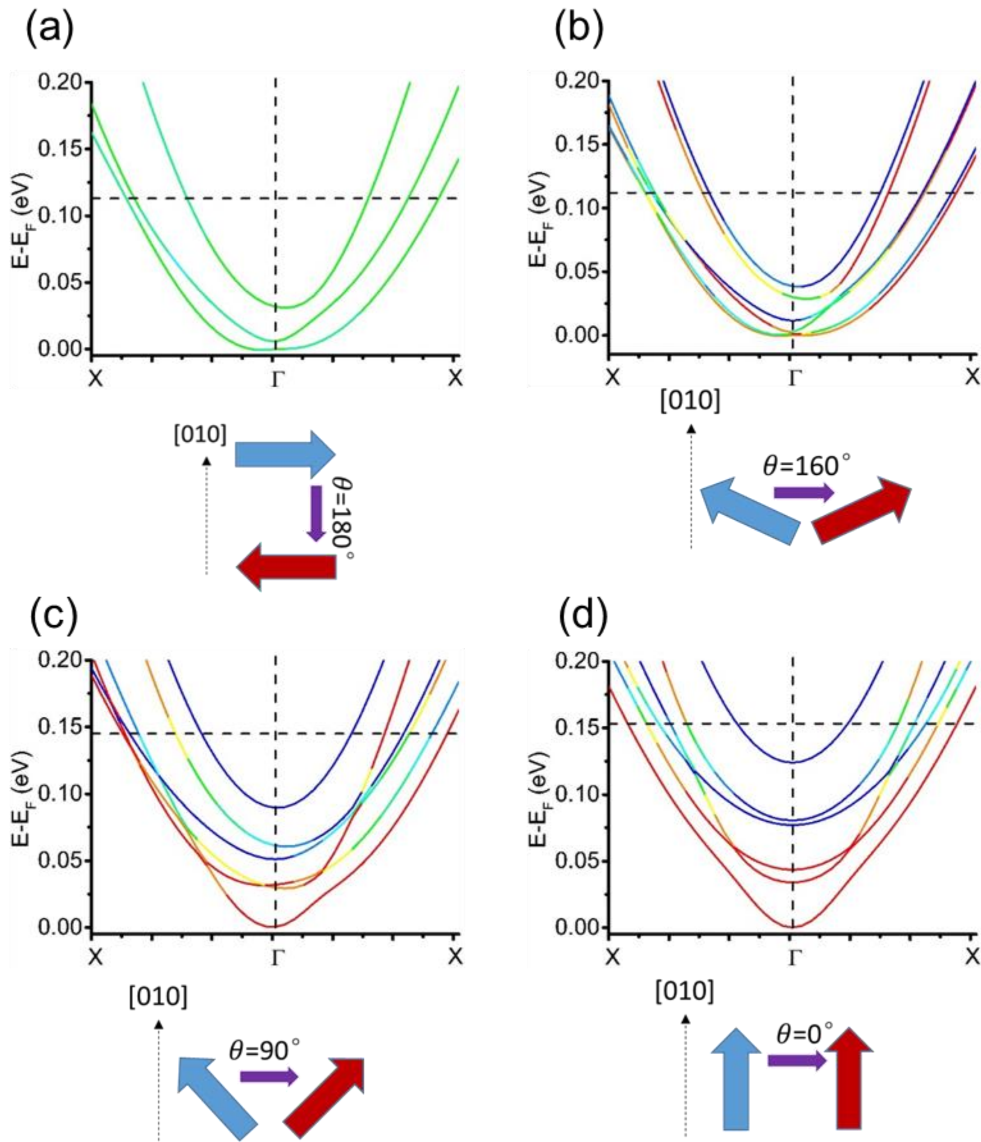

Figure 2.23. Density functional theory resolved band structure of electron doped $EuTiO_3$ with respect to neighboring Eu spin alignment (Courtesy of Xuezeng Lu and James Rondinelli).

A perfect antiferromagnetic ordering, i.e. θ=180°, shows no sign of Weyl crossing (Fig. 2.23(a)) because of symmetry considerations (time-reversal and

inversion symmetries). A Weyl node appears near the center Brillouin zone with small canting and deviation from antiferromagnetic ordering (Fig. 2.23(b)). The crossing moves systematically toward higher energies and the edge of the Brillouin zone with larger canting angles (enhancing ferromagnetic order parameter).

Rotating the current from parallel to the [100] (Fig. 2.21) and from parallel to the [110] (Fig. 2.22), the AMR rotates 45°. The fact that AMR also rotates with the current direction (Fig. 2.21 and Fig. 2.22) and keeps the same symmetry and magnitude regardless of current direction confirms the crystalline nature of AMR. Comparing crystalline and non-crystalline AMRs, only crystalline AMR reflects the crystalline and eventually electronic state symmetry. Here evolution of the AMR symmetry with applied magnetic field reflects the evolution of electronic state symmetry with magnetic field direction and magnitude.

The emergence of two-fold AMR coincides with the transition from positive to negative magnetoresistance, which resembles a metamagnetic transition where magnetic polarization enhances through a spin flip or spin flop (Fig. 2.10). Here, the localized spins (7 μB per Eu atom) are on Eu 4*f*, while conduction electrons are from Ti 3*d* orbital. This means that the transition observed in the magnetoresistance is due to the exchange interaction between localized Eu 4*f* and conduction Ti 3*d* electrons. The occurrence of crystalline uniaxial AMR is striking since the AMR symmetry is lower than the lattice itself, suggesting possible violation of Neumann's principle. The change in AMR symmetry can also be explained by a

simple ferromagnetic phase transitions under applied field in $EuTiO_3$, however, crystalline nature of AMR weakens this possibility.

2.5. Spontaneous Hall effects at $SmTiO_3/EuTiO_3$ interface

In contrast to the rest of the rare earth titanates, which are well known prototypical Mott insulators with d^1 electron configurations, $EuTiO_3$ is a band insulator with d^0 electron configuration and non-polar planes of $Eu^{2+}O^{2-}$ and $Ti^{4+}O_2^{4-}$ stacked alternatively in the (001) surface normal [19]. Thus, $EuTiO_3$ is a possible candidate to replace $SrTiO_3$ in $LaAlO_3/SrTiO_3$ and $R$$TiO_3/SrTiO_3$ heterostructures. Using electrostatic doping eliminates doping atoms and their associated defects. Additionally, effective confinement of electronic states in a magnetic host brings possibility of new physics and a potential means to generate new functionalities. Here, $SmTiO_3/EuTiO_3$ heterostructures grown by molecular beam epitaxy (MBE) are investigated. Formation of a two-dimensional electron system and its magnetotransport properties at low temperature are studied.

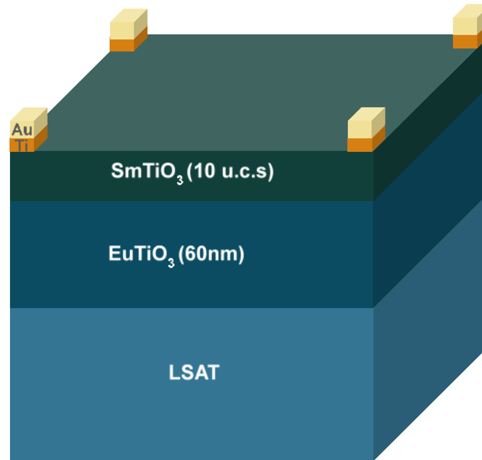

Figure 2.24. Schematic illustration of the $SmTiO_3$(10 u.c.s)/$EuTiO_3$(60 nm) heterostructure with Van der Pauw contact structure grown on LSAT substrate.

Figure 2.25(a) shows the sheet resistance (R_s) as a function of temperature for undoped $EuTiO_3$ (60 nm) film and $SmTiO_3$(10 u.c.s)/$EuTiO_3$(60 nm) heterostructure. While the $EuTiO_3$ film is highly resistive and quickly exceeds the measurement limit around room temperature, the $SmTiO_3$(10 u.c.s)/$EuTiO_3$(60 nm) heterostructure shows metallic behavior down to 2 K. An upturn in sheet resistance emerges at ~30 K and is followed by a relatively sharp peak at ~ 6 K due to a magnetic transition similar to uniformly doped samples. Figure 2.25(b) shows the temperature dependence of two-dimensional carrier concentration for the $SmTiO_3$(10 u.c.s)/$EuTiO_3$(60 nm) heterostructure using the ordinary Hall effect. The room temperature carrier concentration (3.9×10^{14} cm^{-2}) closely matches the expected value from theory (3.4×10^{14} cm^{-2}). These results show a weak temperature dependence, which may be due to Hall scattering rate temperature

dependence that were discussed previously [50,184], or carrier trapping with temperature.

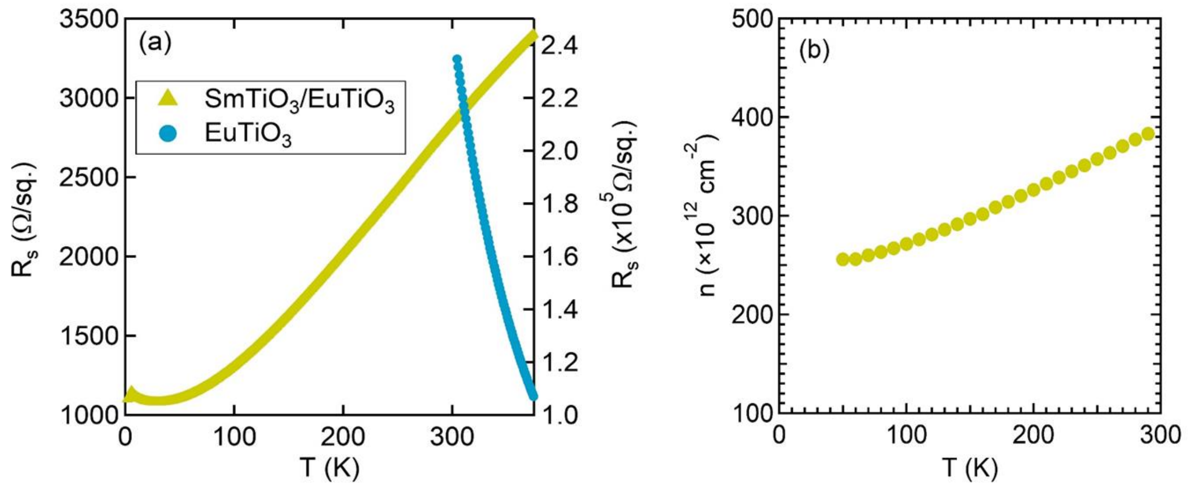

Figure 2.25. (a) Temperature dependence of sheet resistance of $EuTiO_3$(60 nm) with and without of the $SmTiO_3$(10 u.c.s). (b) Temperature dependence of the two-dimensional Hall carrier concentration of the $SmTiO_3$(10 u.c.s)/$EuTiO_3$(60 nm) heterostructure.

Figure 2.26 shows the magnetization measurements of the $SmTiO_3$(10 u.c.s)/$EuTiO_3$(60 nm) heterostructure with in-plane applied magnetic field. Magnetometry as a function of temperature with field cooling (100 Oe) showed the magnetization started to increase at ~6 K, which is consistent with the magnetic transition of the undoped $EuTiO_3$ and the observed peak in sheet resistance. Fig. 2.26(b) shows a very small remnant magnetization. A spuerlinear increase in magnetization can be noticed roughly at 0.3 T, suggesting a magnetic transition to a more magnetic state.

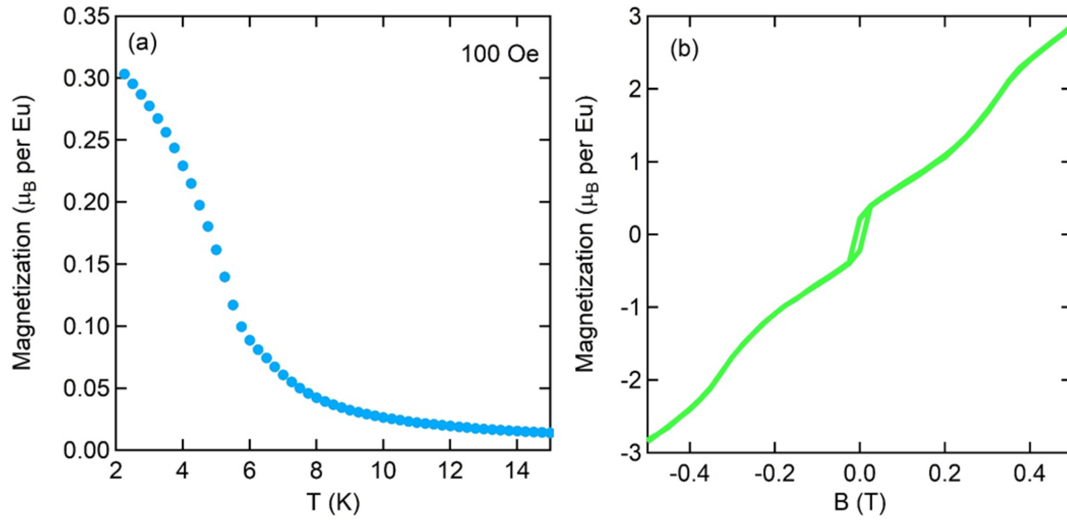

Figure 2.26. Magnetization measurements of the $SmTiO_3$(10 u.c.s)/$EuTiO_3$(60 nm) heterostructure at 2 K. (a) Magnetization as a function of temperature under field cooling (100 Oe, in-plane). (b) Magnetization as a function of in-plane applied magnetic field.

Figure 2.27(a) shows the longitudinal magnetoresistance as a function of out-of-plane applied magnetic field at 2 K, 5 K, 15 K, and 30 K. Here, the out-of-plane magnetic field was swept from +9 T to -9 T and back. The heterostructure shows negative magnetoresistance at all temperatures. A small hysteresis can only be noticed at 2 K, in-line with magnetization result in Fig. 2.26(b). While the data at 2 K shows a sharp inflection at ~3 T, the higher temperature results show a smooth cross-over.

Figure 2.27(b) shows the AHE and THE contributions to Hall resistance at 2 K, 5 K, 15 K, and 30 K. R_{xy} is given by: $R_{xy} = R_0 H + R_{AHE} + R_{THE}$, where R_{AHE} and R_{THE} are the AHE and the THE contributions, respectively [20,23,49]. After

antisymmetrizing the raw Hall data, a linear fit (6-9 T) is used to extract the ordinary Hall component (R_0B). The monotonic increase in resistance with magnetic field (B) extrapolated to zero is characteristic of a conventional AHE. While a pure AHE is observed at 30 K, additional features can be noticed at lower temperatures. Here, the peak at ~ 1.4 T and 2 K is associated with the THE.

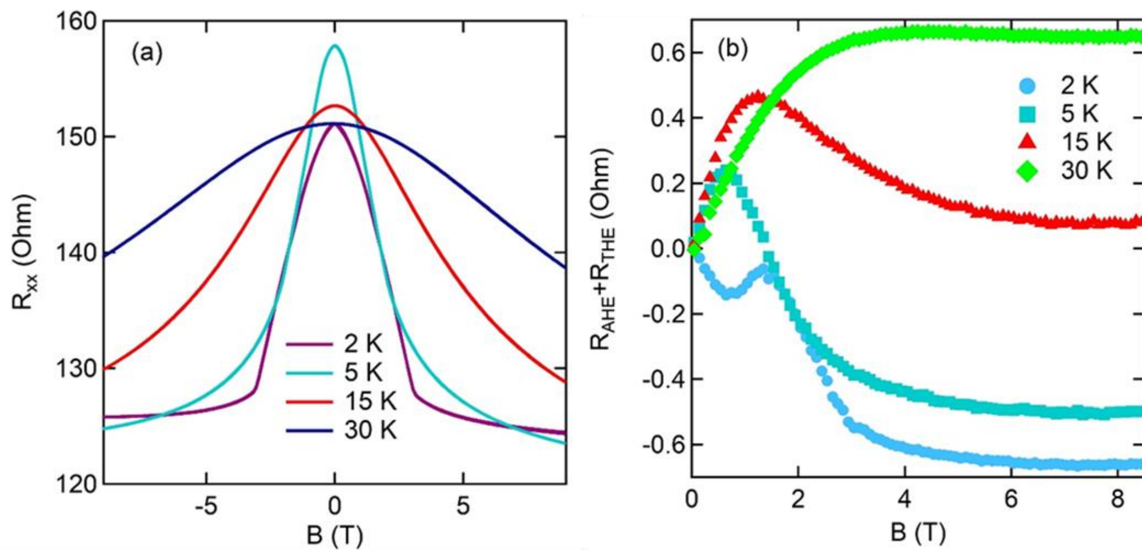

Figure 2.27. (a) Longitudinal magnetoresistance of the $SmTiO_3$(10 u.c.s)/$EuTiO_3$(60 nm) heterostructure at 2 K, 5 K, 15 K and 30 K. THE and AHE of the $SmTiO_3$(10 u.c.s)/$EuTiO_3$(60 nm) heterostructure at 2 K, 5 K, 15 K and 30 K.

While doped $EuTiO_3$ only shows THE signature at 2 K and a pure AHE at higher temperatures (Fig. 2.12), here a relatively broad THE peak is noticed at 5 K and 15 K. Fig. 2.27(b) also shows a sign change in AHE with temperature while the THE keeps the same sign. Bulk polycrystalline MnGe also shows a similar evolution in AHE with temperature [185]. MnSi thin films also show a thickness

dependent AHE and THE with more prominent sign and magnitude evolution of AHE and THE with temperature in thinner films [186]. Here, while the AHE changes sign with temperature, the THE peak stays positive but becomes broader in applied magnetic field in higher temperatures, highlighting the different fundamental origin for two spontaneous Hall effects. Persistence of the THE peak up to higher temperatures can be due to effective confinement of electron system here. Long range fluctuations can be created with negligible energy cost in two-dimensional electron systems as they increase the entropy [187]. Finally, sign and magnitude of AHE and THE strongly depend on the density of states and spin polarization of the electrons near the Fermi surface and, as a result, are very sensitive to Fermi energy.

Chapter 3. Metal-insulator transitions at $SmTiO_3/SrTiO_3$ interfaces

3.1. Introduction

Two-dimensional electron systems at perovskite oxide interfaces provide novel phenomena and exhibit, for example, strong lattice coupling, subbands arising from *d*-orbitals with large short-range Coulomb interactions, and magnetic and orbital order instabilities [3]. A heavily studied two-dimensional electron system is $SrTiO_3$ interfaced with another insulating perovskite oxide with a polar surface, such as $RTiO_3$ (R is a rare earth ion) [188] or $LaAlO_3$ [189]. The two-dimensional electron systems in $SrTiO_3$ is on the border of multiple electronic, structural and polar instabilities [190,191] and, as a result, external stimuli like temperature or applied electric or magnetic fields can generate a large response. For example, it was shown that using an electric field one can induce an insulator-superconducting transition in two-dimensional electron system at $LaAlO_3/SrTiO_3$ interface [137]. This chapter is divided into two parts. In first part, a reversible metal-insulator transition with large carrier modulation is observed using applied electric field in a top-gated $SmTiO_3/SrTiO_3$ heterostructure. In the second part, heterostructures of $SmTiO_3/SrTiO_3$ are studied below the MIR limit. These samples show a sharp metal-insulator transition in a narrow temperature window which can be tuned up to vicinity of room temperature with $SmTiO_3/SrTiO_3$ thicknesses.

3.2. Gate-induced MIT above the MIR limit

Metal-insulator transitions in 2DEGs are of longstanding interest in solid state physics [192–195]. Gate-induced carrier modulation is the main experimental tool, and of practical importance, to study metal-insulator transitions. Substantial modulation of two-dimensional electron liquids at the $SmTiO_3/SrTiO_3$ interface by electric field effect is challenging due to very large carrier densities, which matches the theoretically predicted density of ~ 3×10^{14} cm^{-2} [135]. Using the large capacitance of $SrTiO_3$, bottom-gated devices have shown record carrier modulation of 10^{14} cm^{-2} [196], which is, however, not sufficient to completely pinch off the channel. Here, we use a top-gated geometry field effect three terminal device, in which $SmTiO_3$ provides both the polar discontinuity needed for 2DEL formation in $SrTiO_3$ and acts as the gate dielectric. Figure 3.1 illustrates the heterostructure and device geometry. The benefits of thinning down the $SmTiO_3$ are twofold; the capacitance density is inversely proportional to dielectric thickness and increases in thinner $SmTiO_3$ layers; the carrier density in the channel decreases significantly. The lower carrier densities in the two-dimensional electron system suppresses the gate leakage and helps with depleting the channel towards complete pinch off. The Schottky barrier formed by the Pt gate metal depletes the two-dimensional electron system further and carrier density falls below the critical value needed for MIT. Finally, applying a gate voltage, the channel conductance can then be modulated effectively through a metal-insulator transition.

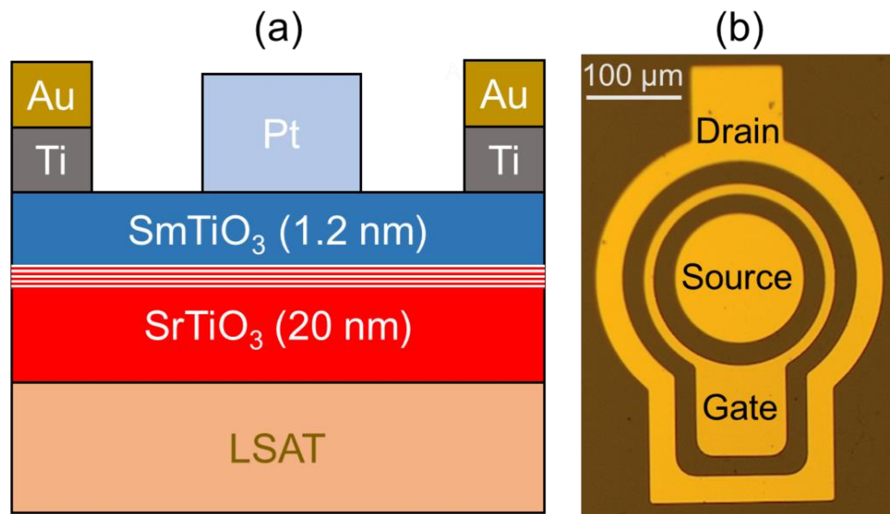

Figure 3.1. (a) Schematic cross-section of the $SrTiO_3/SmTiO_3$ based field effect device. The two-dimensional electron system at the $SrTiO_3/SmTiO_3$ interface are illustrated in shaded region. (b) Optical micrograph, showing top view of the device.

Epitaxial heterostructures containing a 20-nm-thick $SrTiO_3$ layer and three unit cells (u.c.s) of $SmTiO_3$ (~ 1.2 nm) were grown by hybrid molecular beam epitaxy on a (001) single crystal $(La_{0.3}Sr_{0.7})(Al_{0.65}Ta_{0.35})O_3$ (LSAT). Device fabrication was carried out, using a combination of conventional photolithography and electron beam deposition of Pt and Ti/Au and for the gate metal and the Ohmic contacts, respectively. A 100 nm thick Pt was deposited and patterned first, followed by a (40/400nm) deposition and pattering of Ti/Au. The room temperature measurements and device screening were carried out using an Agilent B1500A parameter analyzer. Capacitance-Voltage (CV) measurements were performed at different frequencies (1, 5, 10, 50, 100, 500, 1000, and 5000 KHz) with the same

Agilent B1500A parameter analyzer (signal amplitude 30 mV). Four-terminal electrical measurementrs (Hall and sheet resistance) were carried out using using a Quantum Design Physical Property Measrement (PPMS) in square van der Pauw structures. Finally, temperature dependent three- and two-terminal electrical measurements were done using in the same PPMS.

3.3. Sheet resistance with temperature

Figure 3.2 shows the sheet resistance (R_s) as a function of temperature with and without a Pt gate metal, respectively. Without Pt gate metal, heterostructure shows metallic behavior ($\frac{dR_s}{dT} > 0$) down to ~260 K. Hall measurements reveal a sheet carrier concentration of ~10^{14} cm^{-2}, which is drastically less than the 3×10^{14} cm^{-2} carrier density observed in heterostructures with thick $SmTiO_3$ ($\gtrsim 20\, u.c.s$) [188,197]. Here, the room temperature sheet resistance magnitude (~ 18 kΩ/□) is close to the two-dimensional MIR limit of h/e^2 or ~25 kΩ/□, where the electrons should become strongly localized in the channel at low temperatures (e is the elementary charge and h is Planck's constant) [198]. A 100-nm-thick Pt layer provides the additional depletion of carriers which pushes the system into the insulating ground state even at room temperature.

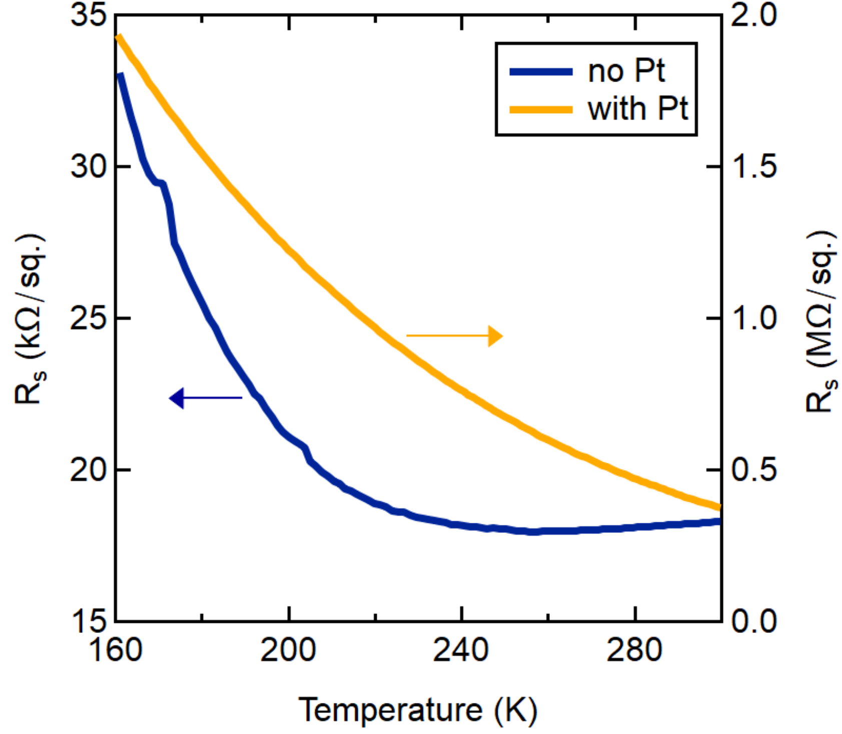

Figure 3.2. Sheet resistance (R_s) with temperature for $SmTiO_3$/$SrTiO_3$ heterostructure with and without the Pt gate metal.

3.4. Gate leakage and gate metal depletion

Figure 3.3(a) shows gate leakage (gate current density I_{GS} vs. gate voltage V_G) at different temperatures. Figure 3.3(b) shows a thermionic fit to data.

$$I_{GS} = A^* T^2 \exp\left(-\frac{e\phi_B}{k_B T}\right)\left[\exp\left(\frac{eV_G}{nk_B T}\right) - 1\right], \quad 3.1$$

where A^* is the Richardson constant, ϕ_B the barrier height, e the elementary charge, n the ideality factor and k_B the Boltzmann constant. Since A^* is not known for $SmTiO_3$, the value for $SrTiO_3$ is used (156 $A.cm^{-2}.K^{-1}$ ([199])). This fit yields n =

16 and $\phi_B = 0.52$ eV. A large value of n hints at a strong contribution by tunneling which is in accordance with low thickness of $SmTiO_3$ dielectric, and/or interfacial layers [198].

Deposition of a 100-nm-thick Pt layer increases sheet resistance dramatically (more than one order of magnitude to about 380 kΩ/□), pushing system deep into the insulating state at and below room temperature. Knowing the height of the Schottky barrier, the gate metal depletion can be estimated to be ~6×10^{13} cm^{-2} for $SmTiO_3$ dielectric constant of ~ 25, which is enough to push sheet resistance above the MIR limit by itself. Furthermore, the dramatic increase in sheet resistance (factor of ~20) is much larger than magnitude of carrier density depletion. This implies that metal-insulator transition here is also accompanied by a significant localization of carriers, as the conduction mechanism in the channel transforms to hopping transport from band transport in proximity to the gate metal.

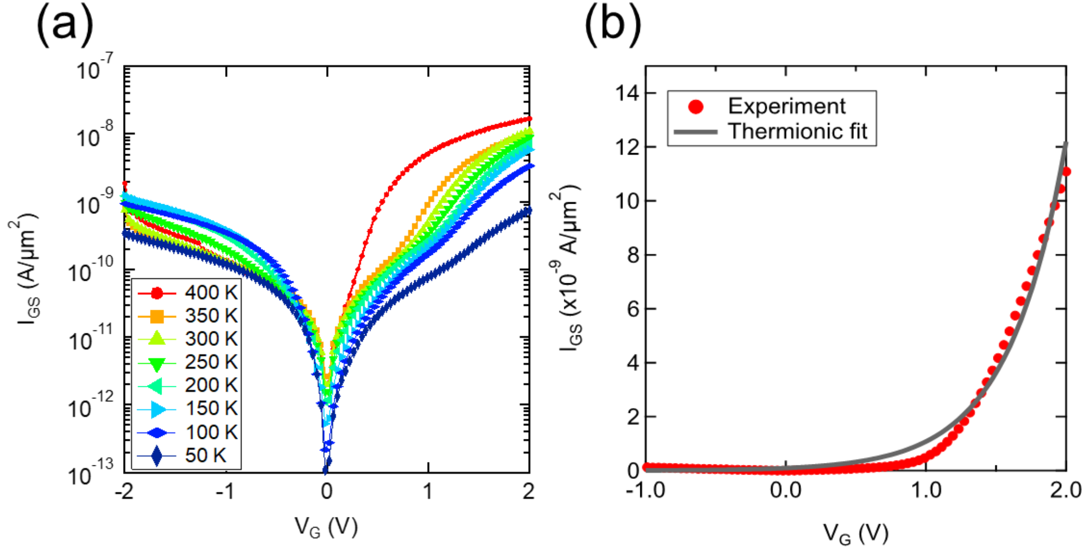

Figure 3.3. (a) Gate current density I_{GS} vs. gate voltage V_G at different temperatures (400 K, 350 K, 300 K, 250 K, 200 K, 150 K, 100 K, and 50 K). (b) Gate leakage at room temperature with thermionic fit.

3.5. Transistor behavior

Figure 3.4 shows the current density with respect to source-drain voltage (I_{DS}-V_{DS}) characteristics of the transistors at different temperatures as a function of gate voltage (V_G). At high temperatures, device shows well-behaved transistor characteristics, with well distinguished cut-off, linear, and saturation regions. At large positive gate voltages (>1.5 V), device characteristics are dominated by gate leakage. At lower temperatures and specifically at negative gate voltages, resistivity of the channel increases drastically, and an upturn emerges in the I_{DS}-V_{DS} characteristics caused by gate leakage. In what follows the discussion is limited

to temperatures and gate voltages where gate leakage is negligible, and the data is not influenced by gate leakage artifacts.

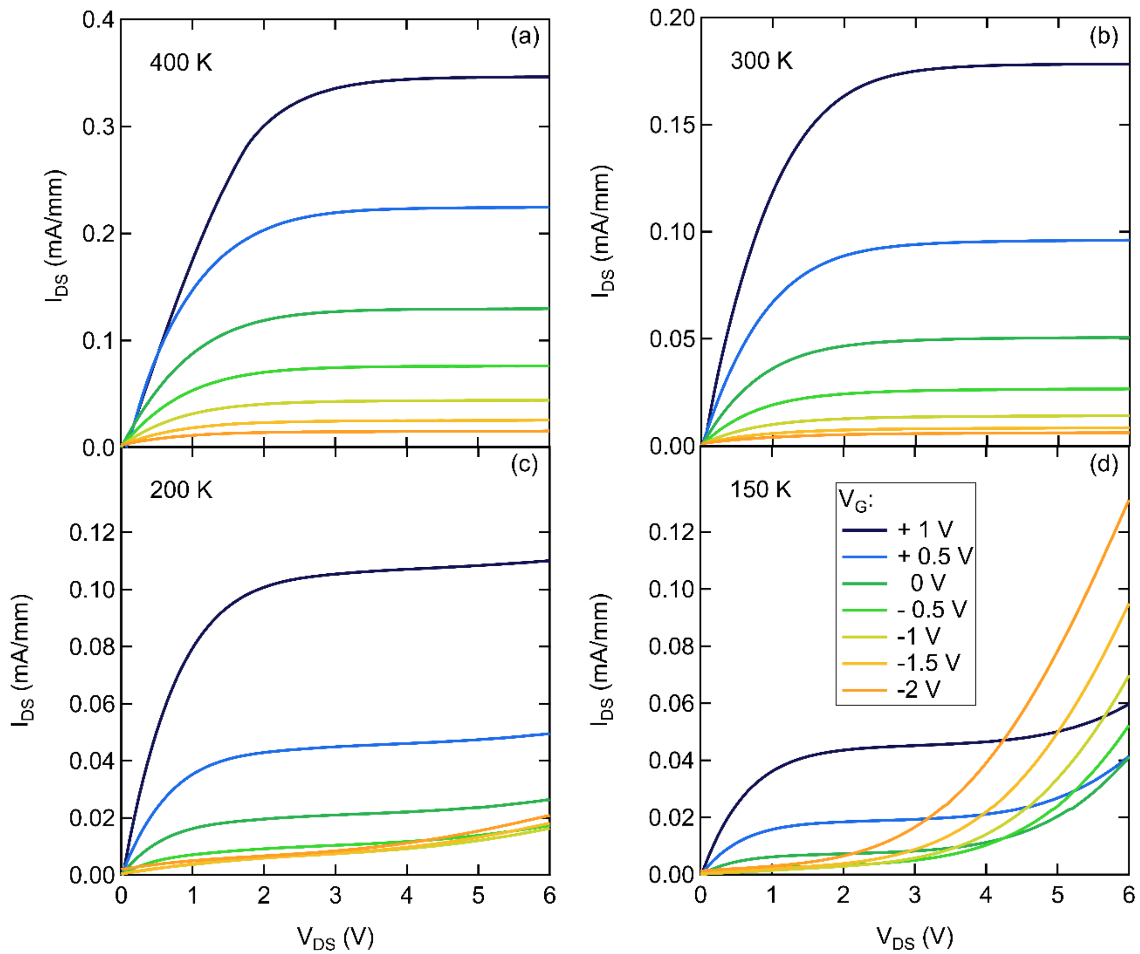

Figure 3.4. I_{DS}-V_{DS} characteristics as a function of gate voltage at (a) 400 K, (b) 300 K, (c) 200 K, and (d) 150 K. Gate voltage was varied from -2 V to 1 V (top curve in each panel) in 0.5 V increments. The current is normalized to drain inner circumference.

3.6. Capacitance voltage and transconductance voltage characteristics

Fig. 3.5(a) shows the frequency-dependent capacitance voltage characteristics at 300 K to approximate the gate modulated carrier density. The capacitance density has a maximum of 3.5 μF.cm^{-2} at ~0.25 V gate voltage at 1 kHz frequency and drops at higher voltages due to gate leakage. The modulated charge density and capacitance density is mostly dominated by the quantum capacitance of the two-dimensional electron system [198]. The roll-off in capacitance with increasing frequency is due to high channel resistance. Here gate voltage sweeps from -1.5 V to +0.5 V yields carrier modulation of ~3.6×10^{13} cm^{-2}. Again, source drain modulation is much larger than carrier modulation seen here. This fact underlines the localizing effect of gate voltage beyond simple carrier modulation. Figure 3.5(b) shows the transconductance (g_m) at room temperature and source-drain voltage of +6 V. Leakage dominates the transport characteristics at large gate voltages ($V_G > 1$ V) and the transconductance drops.

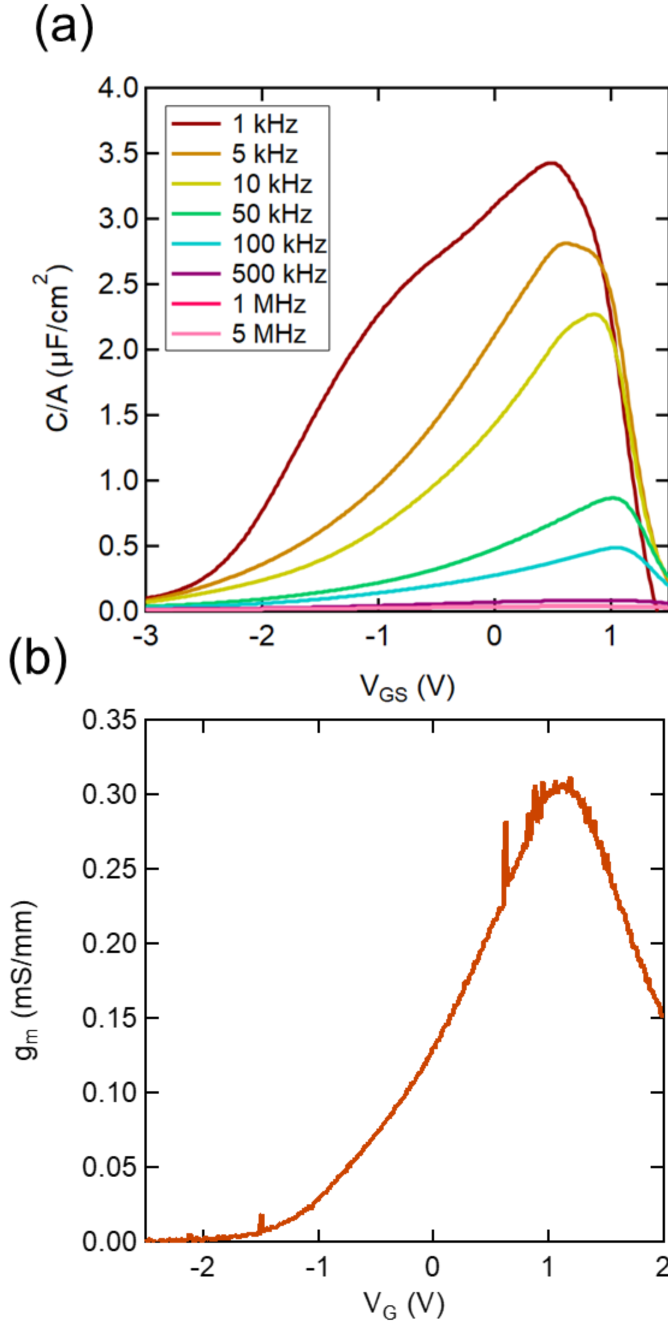

Figure 3.5. (a) Frequency-dependent capacitance voltage characteristics at 300 K. (b) Transconductance as a function of gate voltage at V_{DS}=+6V.

3.7. Metal-insulator transition with gate voltage

Fig. 3.6(a) shows the sheet resistance extracted from a linear fit to low V_{DS} (linear) region of fig. 3.4 as a function of temperature with gate voltage changing between -1.5 V and 1 V. The sheet resistance was calculated by modeling the I_{DS}-V_{DS} characteristics at (V_{DS} < 0.5 V). While the results deviate from four-point measurement shown in Fig. 3.2, the data can reflect the general trend here. From Fig. 3.6(a), one can see a strong insulating behavior for negative gate voltages with a systematic shift towards metallic behavior with increasing gate voltage. At a gate voltage of +0.5 V the system is on the verge of a metallic state and the sheet resistance becomes independent of temperature. The positive gate voltage can reversibly bring back the system to the metallic state. To further drive the system into the metallic state larger positive gate voltages are needed but a combination of large gate leakage and suppressed transconductance prevent a full transition into metallic state.

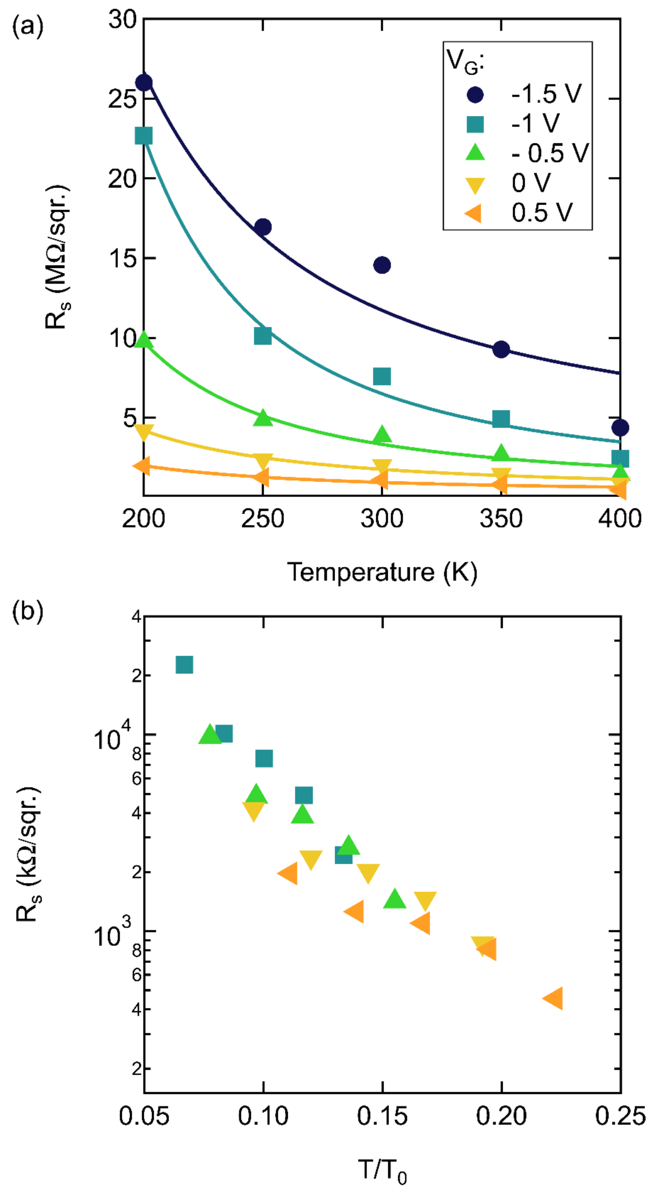

Figure 3.6. (a) I_{DS}-V_{DS} characteristic transistor sheet resistance with temperature at different gate voltages extracted from slope of linear region in Fig. 4.4. The solid lines are a variable range hopping fit. (b) Data in (a) as a function of normalized temp.

To summarize, the data shown here highlights the possibility of tuning an *in-situ* and reversible metal-insulator transition at the two-dimensional electron system in $SrTiO_3$. Here, a two-dimensional electron system deep inside the insulating state (R_s > 380 kΩ/□) is tuned into the proximity to a metallic state. On the border of metal-insulator transition a small change in gate voltage and carrier density brings a very large change in mobility of charge carriers, which is the primary parameter affecting the channel resistance. The behavior is comparable with field effect devices with two-dimensional electron systems in semiconductors and with $LaAlO_3/SrTiO_3$ interface. Electric fields can modulate the mobility of charge carriers at the $LaAlO_3/SrTiO_3$ interface at low temperatures [200]. Surprisingly, the sheet resistance characteristics here is similar to those found on the insulating side of the quantum phase transition for two-dimensional electron systems in Si [201–203]. Particularly, the sheet resistance curves shown in Fig. 3.6(a) can be overlapped temperature axis in Fig. 4.6(b) similar to ref. [204]. In Fig. 3.6(b) the solid line is a fit form $R = R_0 \exp\left[(T/T_0)^{-1/2}\right]$, i.e., the Efros-Shklovskii law the hopping transport resistance with a Coulomb gap [205,206]. Here T_0 contains information about localization length and dielectric constant which systematically enhances from positive to negative gate voltage causing overlap of curves in Fig. 3.6(b). The dielectric constant diverges at metal insulator transition [134,207]. Accordingly, the systematic scaling of T_0 with gate voltage suggests electric field tuning of the systems towards the metal-insulator transition.

Finally, increasing the $SrTiO_3$ thickness enhances the mobility of charge carriers in metallic state which pushes sheet resistance, at the same carrier density, well below the MIR limit. Metal-insulator transition in these two-dimensional electron systems are the subject of next part this chapter.

4.8. Temperature-triggered MIT below the MIR limit

$SmTiO_3/SrTiO_3$ interfaces with sheet resistances well below the MIR limit are studied. A novel metal-insulator transition emerges in this interfacial electron system at low temperatures in which metal-insulator transition temperature scales systematically with the $SmTiO_3$ thickness (i.e. carrier density) [208]. The epitaxial growth of $SrTiO_3$ films (thicknesses of 20, 60 and 80 nm) on (001) LSAT single crystals was followed by *in-situ* epitaxial growth of $SmTiO_3$ layers with thicknesses of 3, 5, 7, and 20 u.c.s, respectively (thicknesses refer to the pseudocubic unit cell parameter of $SmTiO_3$ ~ 3.91 Å). Sheet resistance and Hall measurements are carried out in square Van der Pauw geometry.

Figure 3.7(a) shows the temperature dependence of the sheet resistance for several different heterostructure geometries with a variety of $SrTiO_3$ (20, 60 and 80 nm) and $SmTiO_3$ (3, 5, 7, and 20 u.c.s) thicknesses. These heterostructures show metallic behavior at room temperature with all, except the structure with 20 nm $SrTiO_3$, sheet resistances below MIR limit. Furthermore, all heterostructures, except the sample with 20 u.c.s of $SmTiO_3$, exhibit sharp metal-insulator

transitions, with a significant enhancement in resistance. In most cases, the insulating state resistance exceeds the measurement limit. Measurements carried out during cooling and heating resulted in the same characteristics (no hysteresis was observed), confirming reproducible metal-insulator transitions.

The metal-insulator transition temperature (T_{MIT}) heavily depends on the heterostructure geometry and varies from near room temperature (~260 K for the 3 u.c.s $SmTiO_3$/20 nm $SrTiO_3$ structure) down to ~40 K (7 u.c.s $SmTiO_3$/60 nm $SrTiO_3$ structure). Moreover, all samples with metallic state at 110 K show a resistance hump at that temperature. This resistance anomaly is more noticeable in the sheet resistance derivative, dR_s/dT vs. T, shown in Fig. 3.7(b) (see arrow). From Fig. 3.7(b) it is evident that the anomaly occurs at ~ 110 K, irrespective of sample geometry, carrier density, or T_{MIT}. Accordingly, the two features could be independent phenomena. Bulk $SrTiO_3$ shows antiferrodistortive transition at ~110 K and resistance anomalies have been reported corresponding to this structural transition [209–211]. On the other hand, it is reported recently that antiferrodistortive transition in $SrTiO_3$ films coherently strained to LSAT shifts above the room temperature [126]. It is known that $SrTiO_3$ grown epitaxially on LSAT goes through a ferroelectric phase transition below room temperature [61,93,125,126]. It is therefore possible that ferroelectric transition is the cause for this anomaly, but its exact origin needs further study.

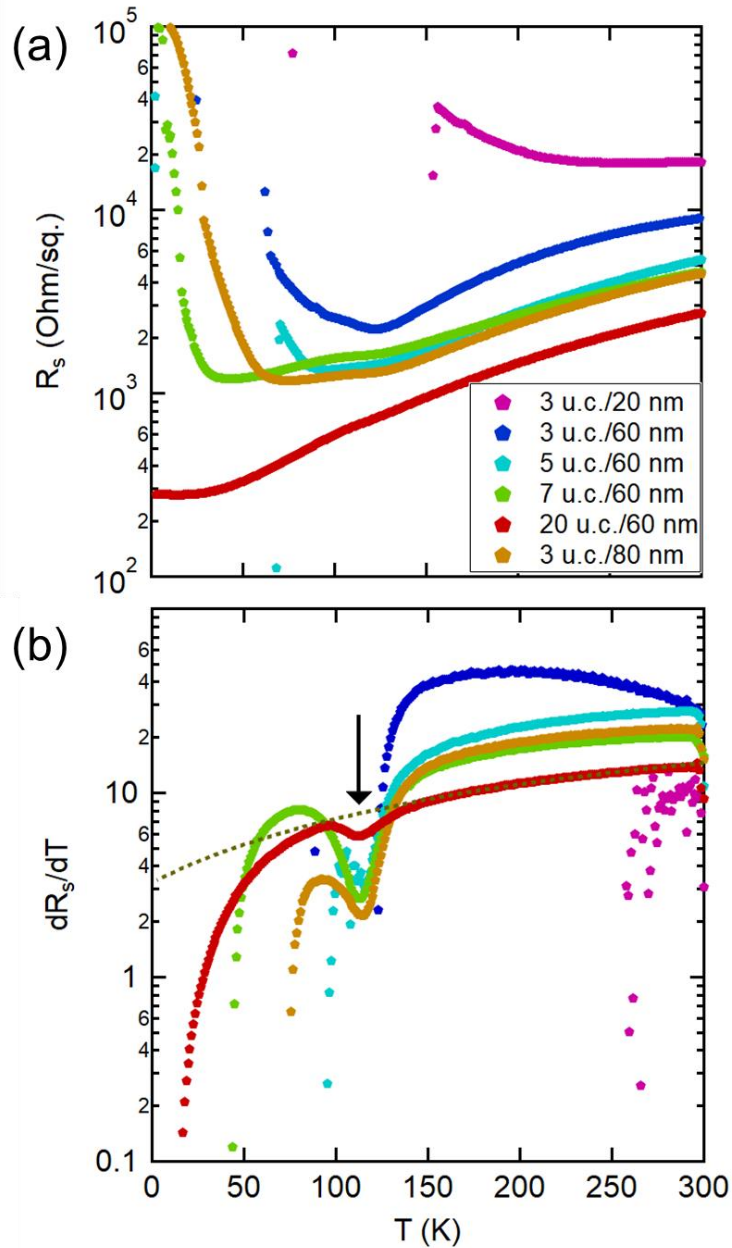

Figure 3.7. (a) Sheet resistance (R_s) as a function of the temperature for heterostructures with various $SrTiO_3$ (20, 60, and 80 nm) and $SmTiO_3$ (3, 5, 7, and 20 u.c.) thicknesses, respectively, as indicated in the legend. (b) Calculated sheet resistance derivative as a function of the temperature. The arrow signifies the resistance anomaly at ~110 K. The dashed line is a power law fit, T^n, to sheet resistance behavior of the 20 u.c. $SmTiO_3$ sample, which is determined n ~ 5/3.

Figure 3.8 shows metal-insulator transition temperature as a function of the Hall sheet carrier density (n_s), measured at room temperature (shown in Fig. 3.9). Here, the metal-insulator transition is defined as the local minimum of resistance with temperature ($dR_s/dT \sim 0$). The room temperature sheet carrier density values are systematically tuned with the $SmTiO_3$ thicknes [59]. They are 1.4×10^{14}, 2×10^{14}, 2.1×10^{14} cm^{-2}, and 2.7×10^{14} cm^{-2} for the samples with 3, 5, 7 and 20 u.c.s of $SmTiO_3$, respectively, and 60 nm $SrTiO_3$. Primarily, Fig. 3.8 shows that metal-insulator transition temperature strongly and systematically depends on the sheet carrier density. Heterostructures with different $SrTiO_3$ thicknesses and slightly different carrier densities and/or mobilities, compared to those with 60 nm $SrTiO_3$, show similar metal-insulator transition. Thus, the primary factor that determines the metal-insulator transition temperature is the charge carrier density.

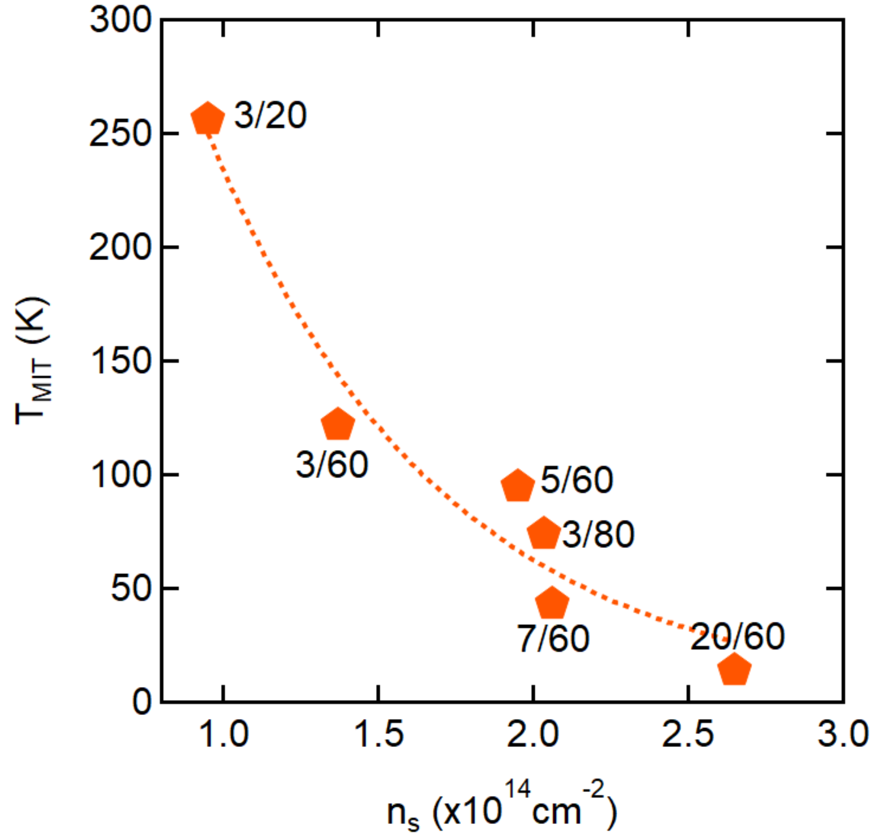

Figure 3.8. Metal-insulator transition temperature (T_{MIT}) as a function of carrier density (n_s) for the samples shown in Fig. 4.7. The dotted line is a guide for the eye. The labels specify samples, with the first and second numbers indicating $SmTiO_3$ thickness in number of unit cells and $SrTiO_3$ thickness in nanometers. Here the sample with 20 u.c. thick $SmTiO_3$, does not show a sharp metal-insulator transition and the temperature for the weak upturn in the sheet resistance is illustrated.

Figure 3.9 shows the Hall measurement results (300-50 K). Figure 3.9(a) illustrates $(eR_H)^{-1}$, where e is the electron charge and R_H the Hall coefficient, with temperature. The $(eR_H)^{-1}$ signifies the sheet carrier density in a single band metallic transport. The sheet carrier density error bar increases drastically below the metal-insulator transition, making the resolved sheet carrier density from Hall measurement unreliable. $(eR_H)^{-1}$ shows a very weak carrier density dependence and does not change with temperature above the metal-insulator transition. While $(eR_H)^{-1}$ depends weakly to temperature above the transition, the sheet resistance shows a power law scaling with temperature (n=5/3). This is due to the different temperature dependencies of the scattering rates that affect Hall angle $H\cot(\theta_H) = R_s/R_H$ (see Fig. 3.9(b)) and sheet resistance. Fig. 3.9(b) highlights a parabolic power law scaling of Hall angle with temperature (n=2) in contrast to sheet resistance. The discrepancy between scaling behavior of Hall angle and sheet resistance causes a weak temperature dependence in R_H even without any change in carrier density [212]. The separation of scattering rates cannot be easily explained using Fermi liquid theory [184,213] and has been observed in many systems like cuprates near quantum critical phase transition [214,215].

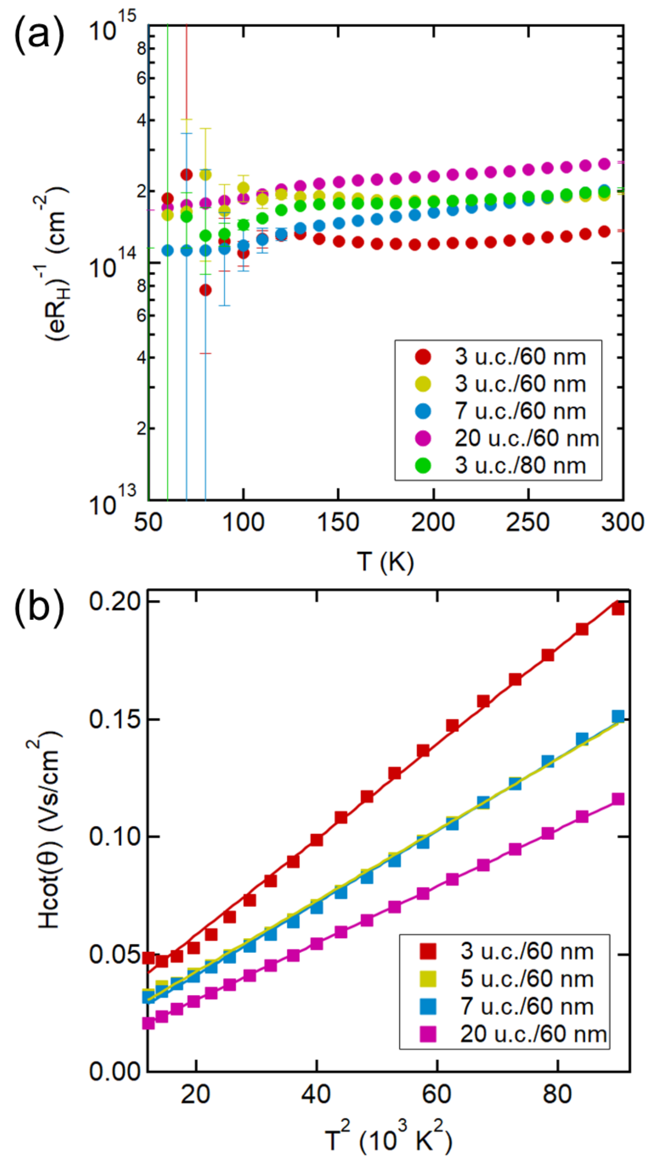

Figure 3.9. (a) $(eR_{\mathrm{H}})^{-1}$ vs. temperature. Low temperature data is not shown here due very large resistance which makes the measurement unreliable. (b) Hall angle as a function of T^2. The solid lines are the T^2 fit to Hall angle data.

We note that Hall angle is inversely proportional to the Hall mobility and follows a T^2 scaling up to room temperature as described by:

$$H\cot\theta_{\mathrm{H}} = H(C + \alpha T^2), \qquad (4.2)$$

where α and C are the residual and is the Hall scattering amplitudes.

Next, the results are discussed. First, the metal-insulator transition observed here should be distinguished from previously reported ones at the verge of the Mott-Ioffe-Regel limit (or quantum resistance) [137,201,216]. In those cases, a sheet resistance near Mott-Ioffe-Regel limit (R_s ~ 25 kΩ/□) corresponds to mean free path of charge carriers becoming comparable to lattice constant and charge carriers essentially are localized at low temperature (the microscopic origins of short mean free path and large resistance are complex) [217]. Subsequently, an insulating (or weakly metallic) state is expected near MIR limit without any sharp transition between metallic and insulating states at a critical temperature. Here, the metal-insulator transition in one sample (3 u.c. $SmTiO_3$/20 nm $SrTiO_3$ sample with R_s ~ 18 KΩ/□) might fit this description. In this case combination of low mobility and carrier density increases sheet resistance near the Mott-Ioffe-Regel limit. The other samples show a sharp metal-insulator transition, while the sheet resistance is an order of magnitude below the Mott-Ioffe-Regel limit. In these samples a deep insulating state emerges from a metal - note the T^2 behavior of the Hall angle – in a very narrow window of temperature. Therefore, the origin of the metal-insulator transition shown here does not lie in conventional physics.

The metal-insulator transition shows similarities with correlated materials like rare earth nickelates [218] and vanadium oxide [219]. These materials also show an abrupt change in resistivity in a very narrow window of temperature, but the transition is typically accompanied with a hysteresis, highlighting the first order nature of their metal-insulator transition. Here, the metal-insulator transition does not show any sign of hysteresis and carrier densities are very dilute compared to strongly correlated materials. We have a half-electron per lateral unit cell which spread over the $SrTiO_3$ thickness which makes carrier concentration a small fraction of the 1 electron/u.c. essential for a Mott insulator. Furthermore, the metal-insulator transition temperature decreases with increasing carrier concentration, showing the opposite trend of what would be anticipated in Mott-type physics. Mott physics predicts an enhanced metal-insulator transition as the carrier concentration approaches half-filling. Consequently, it is unlikely that on-site Coulomb repulsion govern the metal-insulator transitions found here. Also, the Hall effect can be measured in a typical charge ordered or charge density wave system [220] while a meaningful Hall experiment cannot be carried out in insulating state here.

The key observation is that metal-insulator transition temperature and $H\alpha$ both increase with decreasing sheet carrier density. $H\alpha$ is directly proportional to effective mass of charge carriers and its increase signifies larger correlations in samples with lower carrier concentration. Long range Coulomb interactions could play a role here since both these two independent quantities vary inversely with carrier concertation. The significance of long-range Coulomb interactions can be

evaluated using the ratio of the electron-electron interaction energy ($E_{e\text{-}e}$) and the kinetic energy (chemical potential, μ or Fermi energy, E_F). This ratio frequently expressed in terms of the Wigner-Seitz radius, r_s, and larger values highlight stronger long-range interaction. This term for a two-dimensional electron gas is expressed as:

$$r_s = \frac{E_{e-e}}{E_F} = \frac{e^2 m^*}{\hbar^2 \varepsilon} \frac{1}{\sqrt{\pi n_s}}, \qquad 3.2$$

where m^* is the effective mass, $\hbar$ the reduced Planck's constant, e the elementary charge, and ε the dielectric constant. Using $\varepsilon = 300$ (undoped $SrTiO_3$ at room temperature [221]), $m^* = 10$, shown for electrons in the $d_{yz,xz}$-derived bands [222], and $n_s = 1\times10^{14}$ cm^{-2}, we obtain $r_s \sim 5$. This is particularly small since for an electron system to be considered strongly correlated larger value is needed ($r_s \sim 10$). Additionally, a value of 37 is needed for the Wigner crystal to emerge in two dimensions [223]. However, this ratio can enhance significantly. First, presence of multiple occupied subbands can increase r_s proportional to the subband degeneracy. Secondly, $SrTiO_3$ grown on LSAT is believed to be ferroelectric and dielectric constant can change considerably near this transition and modify r_s, which is inversely proportional to dielectric constant. Thirdly, a large interface charge stays unscreened with carrier concentration depleted below full value of $\times10^{14}$ cm^{-2}. The fixed unscreened charge at the polar interface can play a major role is the microscopic origins of this metal-insulator transition, since no temperature triggered sharp metal insulator transition have been reported in bulk doped

$SrTiO_3$ [83] or in other interfacial systems $SrTiO_3$ based systems like $LaAlO_3/SrTiO_3$ [224], at comparable carrier concentrations. Here, charge carriers at the polar interface cause asymmetric electric fields, and hence Rashba-type of spin-orbit coupling [148], which can trigger localization [225]. Ferroelectric localization of charge carriers could also explain the MIT seen here [226]. Finally, should be mentioned, samples are not completely free of defects which may motivate an unconventional insulating state.

In conclusion, combination of non-Fermi liquid behavior, effective mass enhancement, metal-insulator transition below the Mott-Ioffe-Regel limit and correlation of carrier concentration with metal-insulator transition temperature point to unconventional nature of insulating state here. Furthermore, unscreened interfacial charges, Rashba-type spin orbit coupling, and electron correlations can play a crucial role in localizing charge carriers. Finally, the relatively low charge carrier concentration here provides the unique opportunity for a gate induced metal-insulator transition.

Chapter 4. Superconductivity intertwined with ferroelectricity in $SrTiO_3$

4.1. Introduction

$SrTiO_3$ is the first oxide superconductor to be discovered, but the nature of its superconducting state is still heavily debated, reflecting in many ways the elusiveness of other families of unconventional superconductors. A striking feature is that superconductivity in $SrTiO_3$ appears in the very dilute regime where the Fermi temperature is lower than the Debye temperature, which is at odds with a simple Bardeen-Cooper-Schrieffer (BCS) description. Superconductivity in $SrTiO_3$ occurs near ferroelectric instability. It is not uncommon for superconductivity to emerge in the vicinity of another electronic order in unconventional superconductors like cuprates [118] and heavy fermions [227,228]. Several recent proposals have suggested a connection between superconductivity and ferroelectricity in $SrTiO_3$ [14,100,101,103]. Deciphering the relationship between superconductivity and ferroelectricity in $SrTiO_3$ could pave the way towards understanding the nature of the superconducting state in this material.

Noncentrosymmetric superconductors show various exotic quantum phenomena like odd parity Cooper pairs [229], helical superconducting state under field [230–232], and above Pauli-Chandrasekhar-Clogston limit ($\mu_B H_{c2}/K_B T_c \sim 1.84$) upper critical field [233–235]. It is predicted that combination of ferroelectric state and large spin-orbit coupling (i.e. antisymmetric spin-orbit coupling) is a good place to look for odd-parity superconductivity in candidates like $LiOsO_3$, $Cd_2Re_2O_7$ and $SrTiO_3$ [236,237] with possibility of hosting anyons with non-abelian excitations (e.g. Majorana Fermions) [238,239]

which are center of a groundbreaking proposal for fault-tolerant topological quantum computation [239]. More specifically, it is predicted that the intersection of ferroelectricity and superconductivity hosts exciting quantum phenomena in $SrTiO_3$ like mixed parity superconductivity [240,241], topological Weyl superconducting state [242], and upper critical field exceeding Pauli-Chandrasekhar-Clogston limit [108].

4.2. $SrTiO_3$ thin films epitaxially strained to LSAT

Using epitaxial stress, it was shown that $SrTiO_3$ thin films strained to (001) $(La_{0.3}Sr_{0.7})(Al_{0.65}Ta_{0.35})O_3$ (LSAT) single crystal substrate (~1% compressive in-plane strain) display a ferroelectric ground state below room temperature [60,93,125,126]. It was previously reported that $SrTiO_3$ thin films grown heteroepitaxially on LSAT substrate have critical thickness of ~200 nm above which lattice constant relaxes gradually [127]. The in-plane strain ($\varepsilon = \frac{a_{\parallel}-a_0}{a_0}$) can be estimated as -0.947%, where $a_{\parallel}$ is the in-plane lattice constant of strained $SrTiO_3$ (3.868 Å) and a_0 is the lattice constant of relaxed single-crystal $SrTiO_3$ (3.905 Å). Fig. 4.1. compares crystal structure of pristine and epitaxially strained $SrTiO_3$.

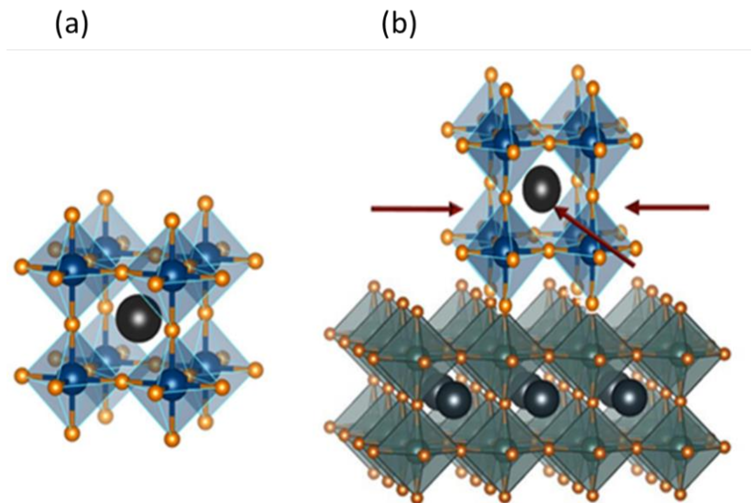

Figure 4.1. Effect of epitaxial strain of crystal structure and symmetry of $SrTiO_3$. An exaggerated comparison between unstrained (a) and epitaxially strained to LSAT (b) $SrTiO_3$.

4.3. Growth and characterization

In this study, high quality Sm-doped $SrTiO_3$ films were grown utilizing hybrid molecular beam epitaxy (MBE). It was previously shown that $SrTiO_3$ films grown by this method surpass the maximum mobility of the bulk single crystals and Shubnikov-de Haas oscillations were successfully observed in these samples [78,243]. Epitaxial Sm-doped $SrTiO_3$ films were grown at 900 °C (thermocouple temperature) on (001) LSAT or $SrTiO_3$ single-crystal substrates in an MBE system (GEN 930, Veeco instruments) with base pressure of $\sim 10^{-10}$ Torr. The growth process is summarized and details are reported elsewhere [47,48]. Elemental Sr and Sm were evaporated from effusion cells using high purity source materials. Titanium and oxygen were supplied from titanium tetra-isopropoxide.

The Sm cell temperature was varied to obtain the desired carrier concentration at a constant growth rate of ~130 nm/h. Reflection high-energy electron diffraction (Staib Instruments, Germany) was used to monitor the growth *in-situ*. Fig. 4.2. shows the reflection high-energy electron diffraction (RHEED) of $SrTiO_3$ film along [100] and [110] azimuths. The surface reconstruction shown here matches the previously reported c(4×4) reconstruction for stoichiometric $SrTiO_3$ [173].

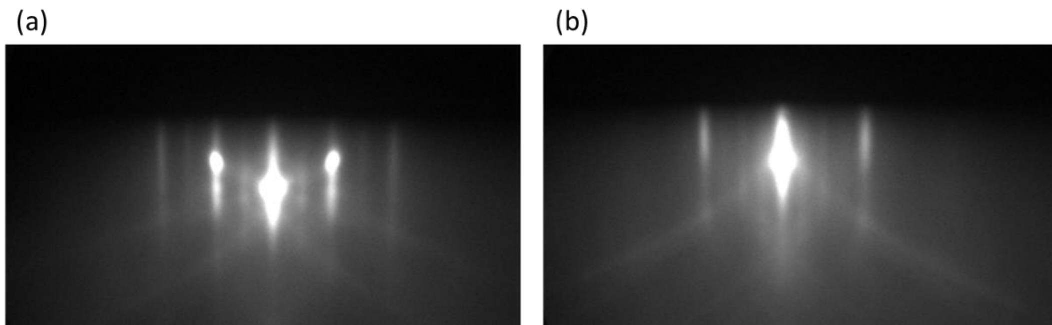

Figure 4.2. *In-situ* characterization of the $SrTiO_3$ during growth. Reflection high-energy electron diffraction of $SrTiO_3$ film in [100] (a) and [110] (b) azimuths.

High-resolution Philips Panalytical X'Pert thin-film diffractometer using Cu K^{α} radiation was used for *ex-situ* characterization of the films. The thickness of the films was fixed at ~200 nm. The 2θ-ω scan of an $SrTiO_3$ film around the (001) reflection peak is shown in Fig. 4.3. A sharp 001 film peak and clear Laue fringes can be seen, highlighting smooth surfaces with high structural quality. The out-of-plane lattice constant is calculated as 3.93±0.001 Å, in accordance with a fully strained $SrTiO_3$ film grown on LSAT substrate [127].

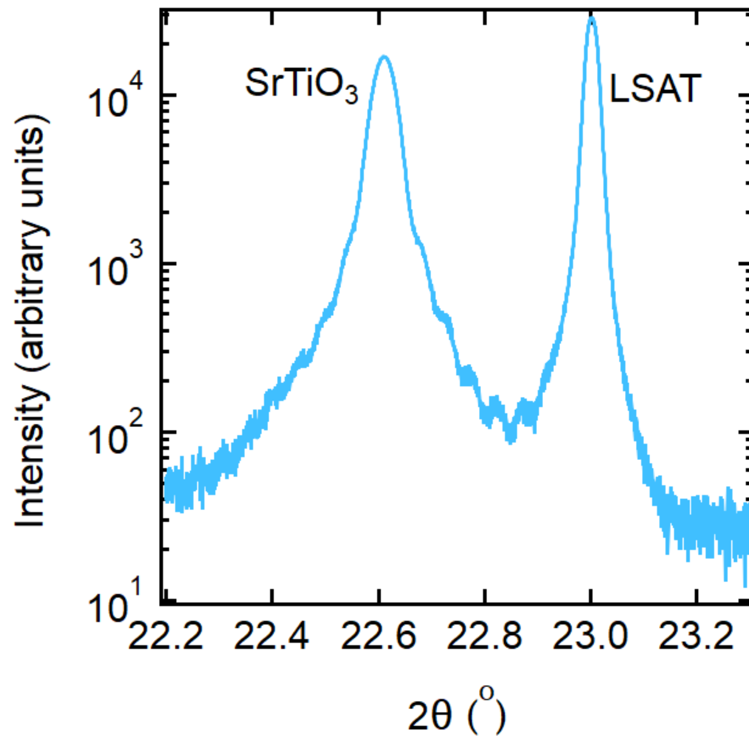

Figure 4.3. 2θ-ω scan of an $SrTiO_3$ film around the 001 peak of LSAT/$SrTiO_3$ heterostructure.

A combination of x-ray diffraction and reflection high-energy electron diffraction oscillations was used to calculate the thickness and growth rate of the films. The final thickness was also verified by the Laue's thickness fringes from x-ray diffraction and cross section scanning transmission electron microscopy imaging. Reciprocal space mapping (RSM) is carried out at near the 113_{pc} reflection for $SrTiO_3$ films on LSAT and used to determine the in- and out-of-plane lattice parameters of the substrate and film. Fig. 4.4 shows the RSM of a LSAT/$SrTiO_3$ heterostructure. The axes denote the in-plane (q_x) vectors and out-

of-plane (q_z) lattice vectors, scaled as $2\pi/a$, where a is the real-space lattice constant of the respective planes. The reciprocal space mapping confirms that the in-plane lattice of the $SrTiO_3$ film is coherently strained to LSAT substrate (a= 0.3868 nm).

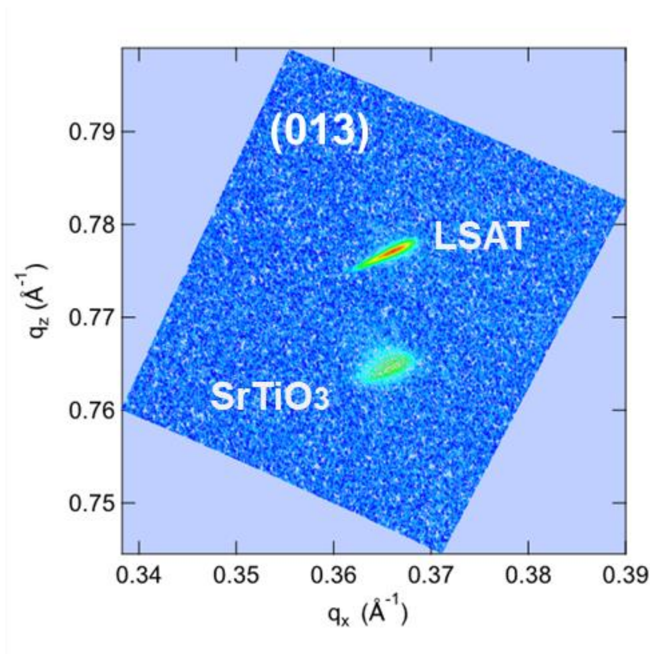

Figure 4.4. Reciprocal space mapping of LSAT/$SrTiO_3$ heterostructure carried out at near 113_{pc} reflection for a $SrTiO_3$ film.

Cross section samples were used for high angle annular dark-field (HAADF) imaging in scanning transmission electron microscopy (STEM) and were prepared by focused ion beam (FEI Helios Dualbeam Nanolab 650) and imaged using a FEI TitanS/TEM operated at 300 kV, with a convergence angle of 9.6 mrad. Fig. 4.5 shows HAADF-STEM cross section of LSAT/Sm:$SrTiO_3$

structure, carried out by Salva Salmani-Rezaie. The interface between LSAT substrate and Sm: $SrTiO_3$ film to be atomically abrupt. Low magnification image shows no extended defects. HAADF-STEM images reveal the film to have high structural perfection with an atomically sharp interface.

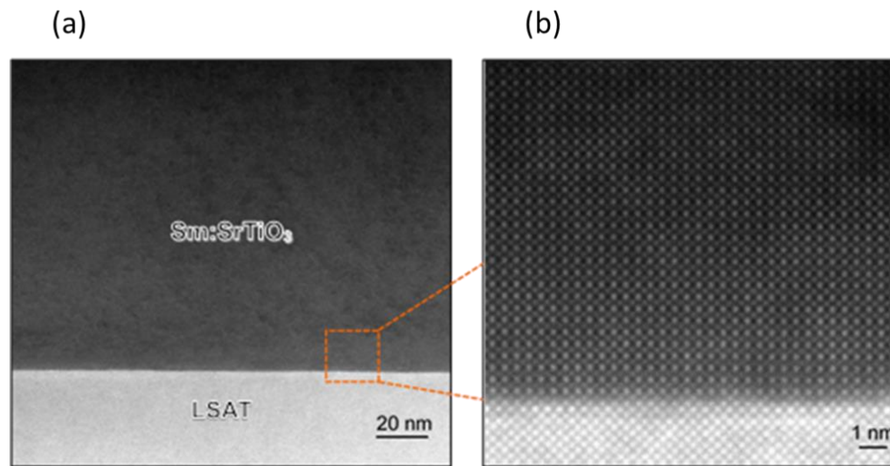

Figure 4.5. Cross-section HAADF-STEM image of Sm: $SrTiO_3$ film grown on LSAT. (a) Low magnification image, showing no extended defect. (b) High magnification image, confirming an atomically sharp and uniform interface between film and substrate (Courtesy of Salva Salmani-Rezaie).

4.4. Magnetoelectric characterization of normal state

Temperature (*T*) dependent sheet resistance and Hall measurements were carried out using a Quantum Design Physical Property Measurement System (300-1.8 K). Transport measurements were carried out in van der Pauw geometry with square shaped samples (5 mm×5 mm). Ohmic contacts (Ti 40nm/Au 400 nm) were deposited on the sample corners (<0.5 mm×0.5 mm) through a shadow mask using

an electron beam evaporation with base pressure of 3×10^{-7} Torr. Figure 5.6 shows carrier densities extracted from the Hall measurements, $n = -1/(teR_H)$ where e is the elementary charge, t is the thickness of the films, and R_H is the Hall coefficient $R_H = dR_{xy}/dB$, resolved from linear fits to the transverse resistance $R_H(B)$ with applied magnetic field (B). The carrier density of electron doped $SrTiO_3$ films grown on LSAT and $SrTiO_3$ scale differently with temperature. While, films grown on $SrTiO_3$ do not show any carrier freezeout down helium liquid temperature, films grown on LSAT show a similar magnitude of mobile carrier loss ($2 - 6 \times 10^{19}\text{cm}^{-3}$) regardless of doping concentration. The temperature in which the carrier freezeout initiates roughly matches the Curie temperature of ferroelectric transition in $SrTiO_3$ films stained to LSAT substrate [93,125,126]. Screening of the spontaneous polarization can localize mobile charge carriers, decreasing density and mobility of electrons.

The carrier concentrations are slightly underestimated, due to the surface depletion in $SrTiO_3$ [244]. All samples show a sharp drop in carrier concentration starting at ~ 110 K. Roughly the same magnitude of mobile carriers ($4 - 7 \times 10^{19}\text{cm}^{-3}$) is lost between 110 K and 1.8 K for all samples in Hall experiment.

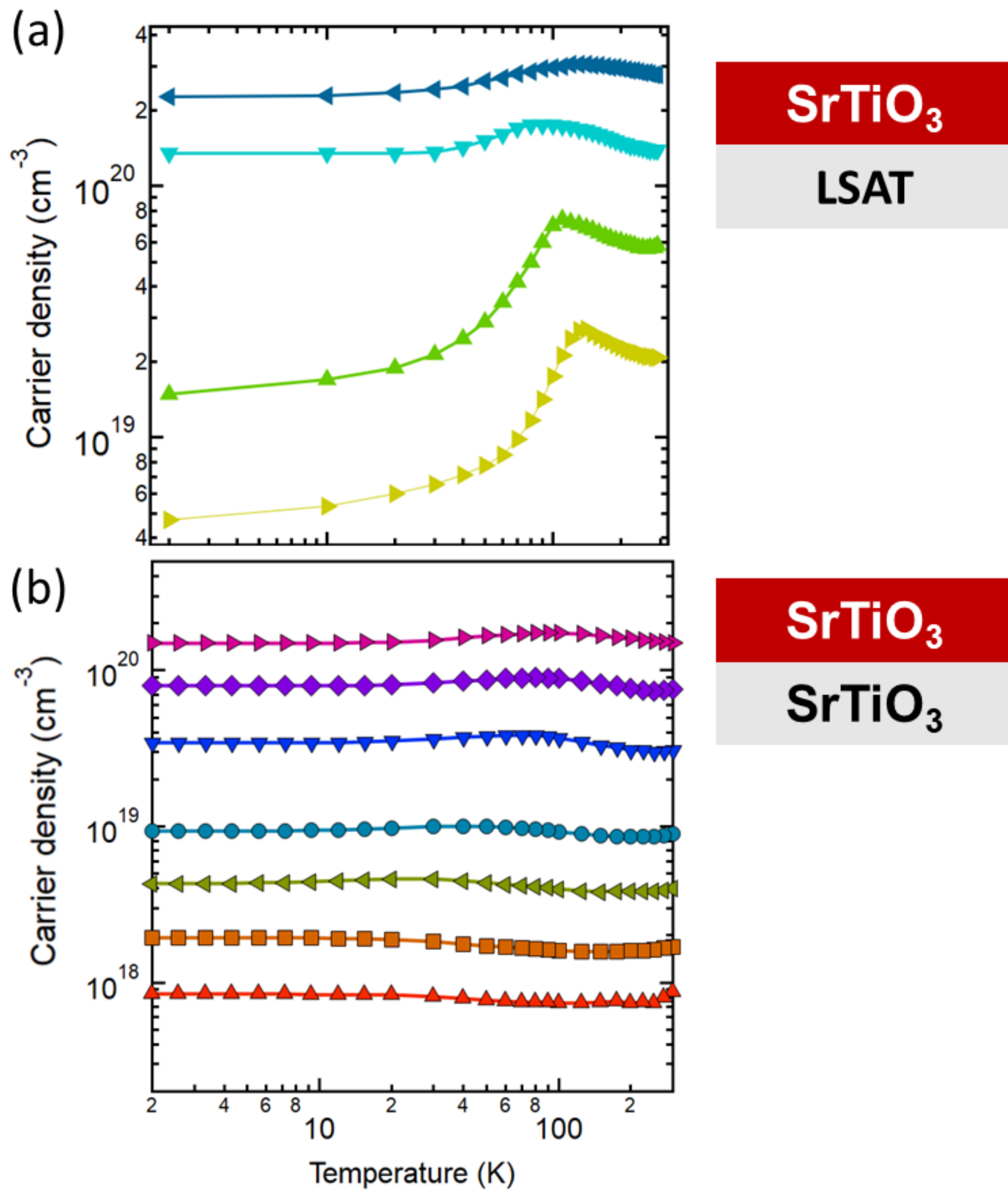

Figure 4.6. Effect epitaxial strain on Hall carrier density. Temperature dependent carrier density of electron doped $SrTiO_3$ grown on (a) LSAT [48] and (b) $SrTiO_3$ [21]. Only strained films show a carrier loss (n_{loss}=2-6×10^{19} cm^{-3}).

Figure 4.7 shows the resistivity with temperature for electron doped $SrTiO_3$ grown on (a) LSAT. While the highest doped sample ($n_H^{300K} = 2.8 \times 10^{20}$cm^{-3}) shows metallic behavior ($\frac{dR_s}{dT} > 0$) down to 1.8 K the lighter doped $SrTiO_3$ films ($n_H^{300K} = 1.4 \times 10^{20}\text{cm}^{-3}$, $6 \times 10^{19}\text{cm}^{-3}$ and $2 \times 10^{19}\text{cm}^{-3}$) show metal-to-insulator transitions ($\frac{dR_s}{dT} \approx 0$) at ~60 K and ~110 K, and 140 K, respectively. The metal-to-insulator transition temperature (T_{MIT}) enhances with decreasing carrier concentration. Near the metal-insulator transition, an apparent loss of carrier density and is seen for all films grown on LSAT (Fig. 4.6(a)). $SrTiO_3$ is well-known for maintaining metallic state even in very dilute samples ($\sim 10^{15}\ cm^{-3}$) [83]. Figure 4.7 (b) shows the resistivity with temperature for electron-doped $SrTiO_3$ grown on $SrTiO_3$. All samples, regardless of carrier concentration, stay metallic down to helium liquid temperature. While, the metallic state survives the carrier loss in highest doped sample, two lower doped samples show a metal-to-insulator transition. Since the Hall coefficient is not be well defined in the insulating state, the room temperature values are reported in Fig. 4.7 (a).

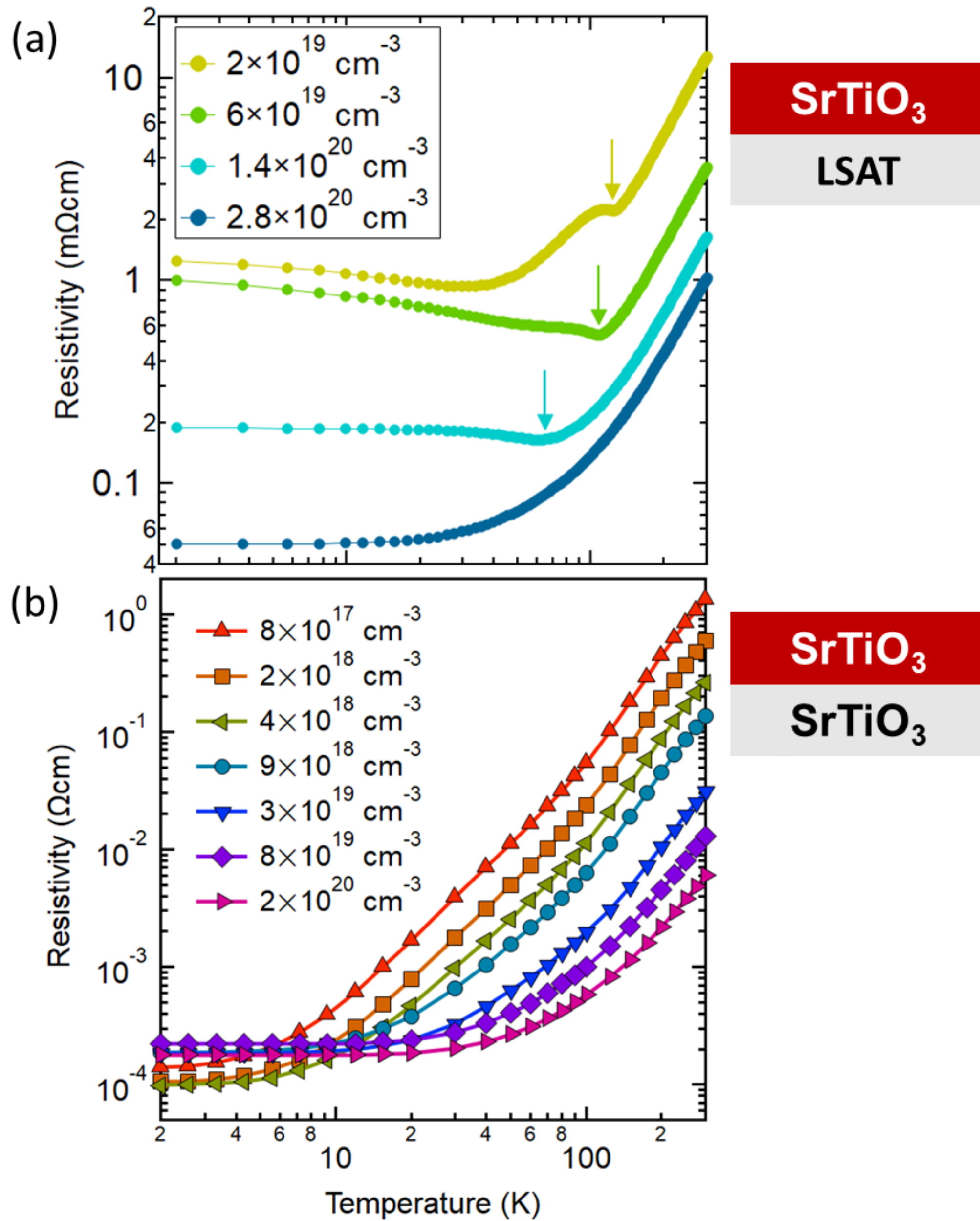

Figure 4.7. Effect epitaxial strain on resistivity. Temperature dependent resistivity of electron doped $SrTiO_3$ grown on (a) LSAT [48] and (b) $SrTiO_3$ [21]. Only strained films show a carrier density dependent metal-to-insulator transition.

4.5. Critical temperature of superconductivity

Magnetotransport measurements below 1 K were done using a dilution refrigerator (Triton™, Oxford Instruments Group). The superconductivity measurements were carried out using a lock-in amplifier (SR 830, Stanford Research systems) in AC mode with excitation current and frequency of 1 μA and 33.33 Hz, respectively. Figure 4.8 shows resistivity with temperature (1 K-15 mK) at zero applied magnetic field. All samples show superconducting transitions. While being commonly considered as a instability of a metallic state, here superconductivity emerges from an insulating state in optimally and under-doped samples. The superconducting critical temperatures are 0.37 K, 0.60 K, 0.67 K, and 0.16K for $n_H^{300K} = 2 \times 10^{19}\text{cm}^{-3}, 6 \times 10^{19}\text{cm}^{-3}, 1.4 \times 10^{20}\text{cm}^{-3}$, and $2.8 \times 10^{20}\text{cm}^{-3}$ carrier concentrations, respectively. Here, the corresponding temperature to $R_S = \frac{R_n}{e}$ is used as T_C, where R_n is the normal state sheet resistance and e is the Euler's number.

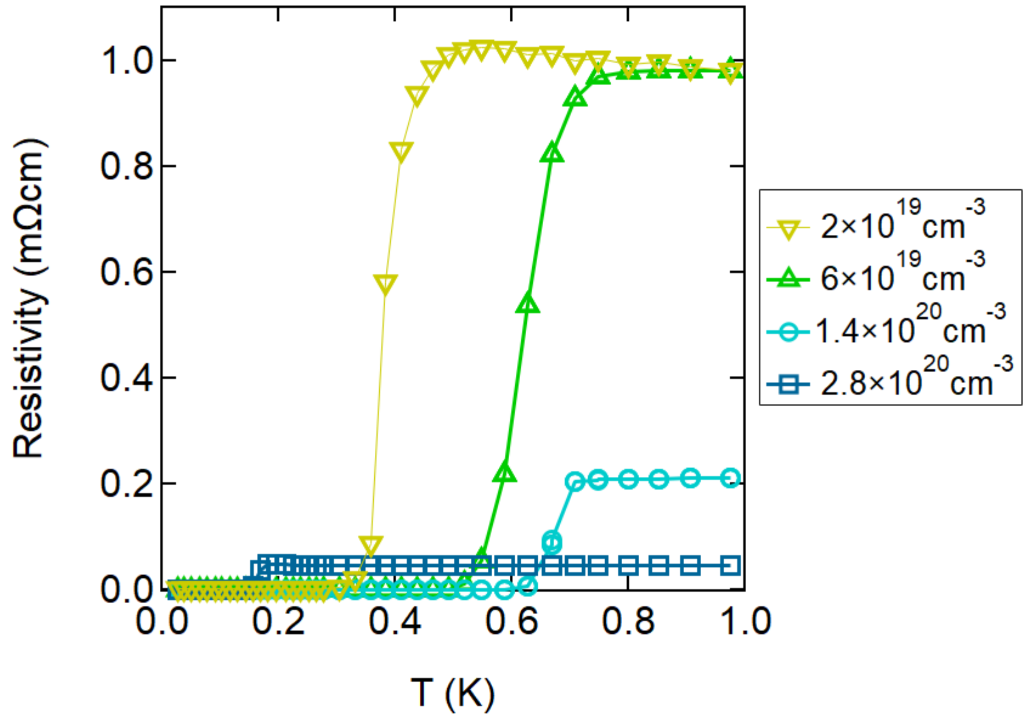

Figure 4.8. Superconducting transitions for Sm-doped $SrTiO_3$ films grown on LSAT with different carrier densities. The resistivity as a function of temperature (1 K-15 mK) at different carrier densities ($n_H^{300K} = 2 \times 10^{19} cm^{-3}, 6 \times 10^{19} cm^{-3}, 1.4 \times 10^{20} cm^{-3}, and\ 2.8 \times 10^{20} cm^{-3}$) . Lines are a guide for the eye.

Figure 4.9 shows the longitudinal resistance with temperature (400 - 15 mK) for Sm- and La-doped samples with $n_H^{2K} = 7.1 \times 10^{20} \mathrm{cm}^{-3}$ and $8.4 \times 10^{20} \mathrm{cm}^{-3}$, respectively, grown on a $SrTiO_3$ single crystal substrate. Both films show a similar T_C and in accordance with previous report on La-doped single crystal $SrTiO_3$ [79].

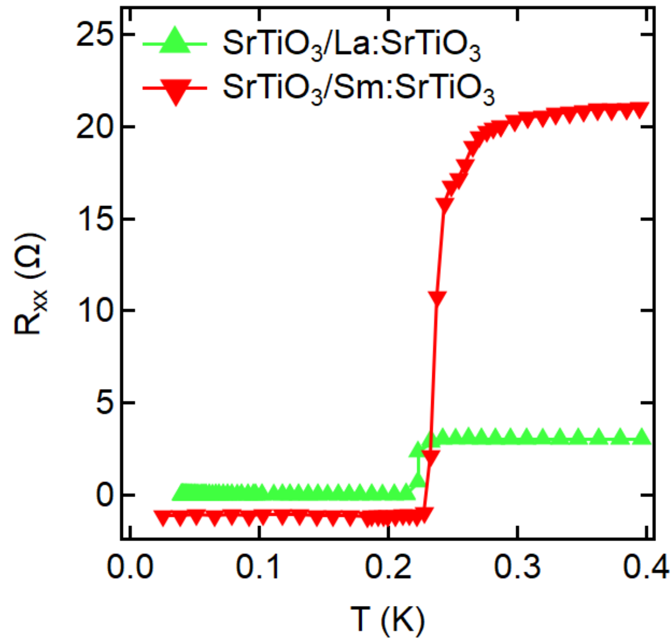

Figure 4.9. Superconducting transition in La- and Sm-doped $SrTiO_3$ grown on $SrTiO_3$ substrate. Longitudinal resistance with temperature for La- and Sm-doped $SrTiO_3$ grown on $SrTiO_3$ single crystal substrate. The lines are guidance to the eye.

4.6. Interplay between superconductivity and ferroelectricity

Electron-doped $SrTiO_3$ films grown epitaxially on LSAT (001) show carrier density dependent ferroelectric transition which matched closely the metal-insulator transition shown in Fig. 4.7. Figure 4.10 shows temperature dependent second harmonic generator (SHG) intensity, carried out by R. Russel, N. Ratcliff and J. Harter, and sheet resistance for Sm-doped $SrTiO_3$ films with room temperature carrier concentrations of $n =$ (a) $6 \times 10^{19} \mathrm{cm}^{-3}$, (b) $1.4 \times 10^{20} \mathrm{cm}^{-3}$ and (c) $2.8 \times 10^{20} \mathrm{cm}^{-3}$ [61]. The sudden enhancement in SHG signal marks the onset of ferroelectric transition. A corresponding resistance upturn matches the loss of inversion center.

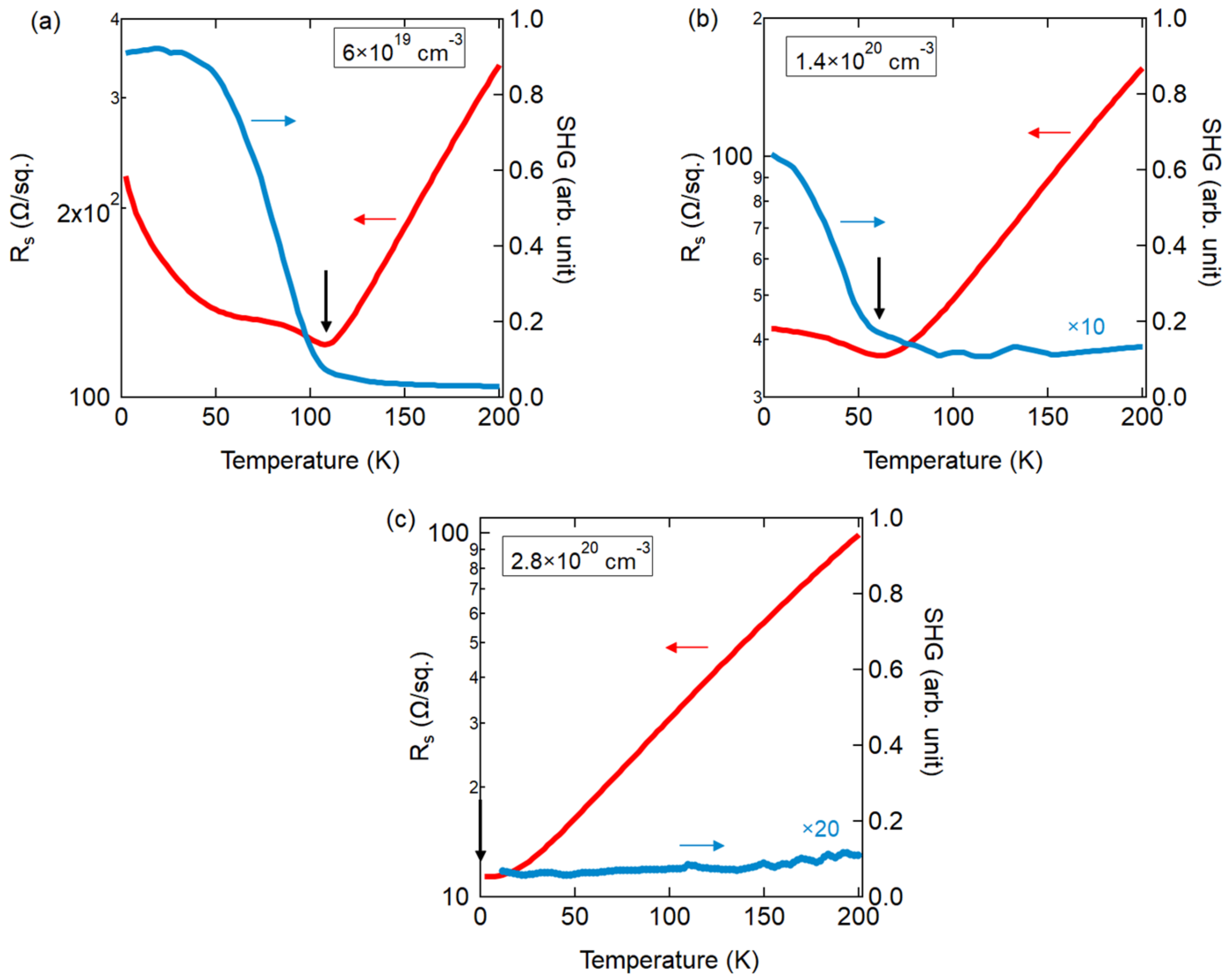

Figure 4.10. Connection between the resistance upturn and onset of ferroelectric transition. Temperature dependence of electrical sheet resistance (left axis) and SHG intensity (right axis) for epitaxially strained $SrTiO_3$ films with Hall resolved room temperature carrier concentrations of n_{3D} = (a) $0.6 \times 10^{20}\text{cm}^{-3}$, (b) $1.4 \times 10^{20}\text{cm}^{-3}$ and (c) $2.8 \times 10^{20}\text{cm}^{-3}$. Black arrows mark onset of ferroelectric transition which is associated with minima is sheet resistance.

Electron density and mobility decrease in Hall measurements. In the over-doped sample, charge carriers can sufficiently screen out dipolar interaction essential for ferroelectric transition, suppressing the ferroelectric ordering of dipoles. A long-range mean-field Ising model can capture the ferroelectric transition in epitaxially strained $SrTiO_3$ [61]. The in-plane epitaxial compressive strain stabilizes an easy polarization axis, i.e. [001] or $[00\bar{1}]$, which is reflected in the bistable Ising order parameter. An extrinsic polarization field, breaking degeneracy of "up" and "down" configurations, is included to account for asymmetric boundary condition since the film is sandwiched between vacuum and substrate. The Hamiltonian model is

$$\mathcal{H} = -\frac{1}{2}\sum_{i,j} U\left(\mathbf{r}_i - \mathbf{r}_j\right)P_i P_j - E\sum_i P_i, \qquad 4.1$$

where i and j are label unit cells, Pi is the order parameter, E preexisting polarization field, and $U(\mathbf{r})$ is the dipolar interaction energy. The space-averaged order parameter $\langle P \rangle$ satisfies mean-field self-consistency equation, $\langle P \rangle = \tanh((\bar{U} + E)/K_B T)$, where $\bar{U} = K_B T_C$. The solutions of self-consistency equation fitted into SHG results from Fig. 4.10 yields ferroelectric phase transition temperature of T_c=92 K for $n_{3D}=0.6\times10^{20}$ cm^{-3} and T_c=39 K for $n_{3D}=1.4\times10^{20}$ cm^{-3}. Polarizing field energies are roughly E/K_B~2 K. The mobile charges can suppress ferroelectricity if Thomas-Fermi screening length, $d_{TF} = \sqrt{\pi a_B^*/4K_F}$, becomes comparable to interdipolar distance, i.e. lattice constant. The solution for $n_{3D}=2.8\times10^{20}$, assuming an isotopic Fermi surface $(K_F = (3\pi^2 n)^{1/3})$, yields

dielectric constant of ~30 which is comparable to previous reports [125]. More recently, a model based on dipolar analogue to RKKY interaction [245] was considered to explain suppression of ferroelectricity in $SrTiO_3$ [246]. In this model opposite charges of a dipole each generate Friedel oscillations as the origin for dipolar interaction. A ferroelectric alignment of dipoles becomes energetically unfavorable for $cos(2K_F l_{dd})$ or $2K_F l_{dd} = \pi$. Here, assuming an isotropic Fermi surface, the interdipolar distance, l_{dd}, equals ~1nm which is larger than expected lattice constant (~0.39 nm) and suggests only a fraction of Ti atoms are displaced in ferroelectric state.

Figure 4.11 illustrates the phase diagram of strained $SrTiO_3$ film with both superconducting and ferroelectric phase boundaries. Here, samples deep into ferroelectric state ($n_{3\mathrm{D}} = 0.6 \times 10^{20}\ \mathrm{cm}^{-3}$ and $1.4 \times 10^{20}\ \mathrm{cm}^{-3}$) show a factor of two enhancement in critical temperature of superconductivity while over-doped sample behaves very similar to unstrained samples. The superconducting enhancement cannot be a simple strain effect, e.g. strain modification of phonon modes, since all the samples have similar strain and enhancement only occurs in specific carrier density range. Furthermore, the sharp decrease in superconducting critical temperature on the over-doped side coincides with demise of ferroelectric state, where screening by electrons overcomes any tendency toward long-rang ordering of dipoles.

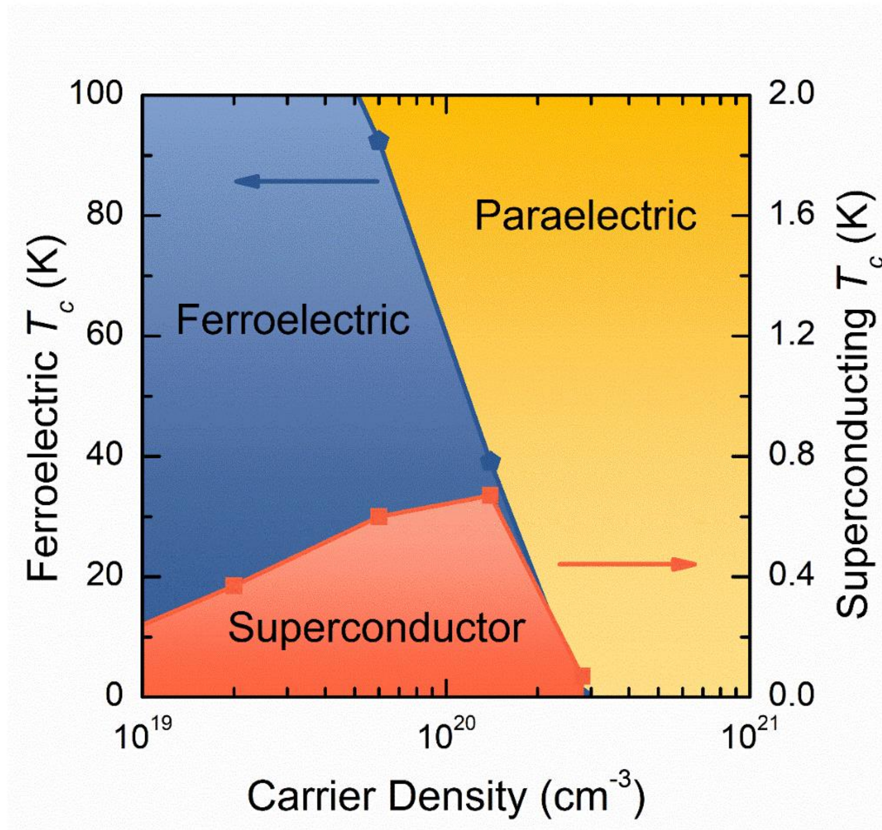

Figure 4.11. Doping-temperature phase diagram of epitaxially strained Sm-doped $SrTiO_3$. An enhanced superconducting dome appears deep inside the ferroelectric state, highlighting a deep connection between ferroelectric and superconducting orders. The superconductivity diminishes abruptly where ferroelectric order is screened by doped electrons in over-doped samples.

Figure 4.12 compares the T_c for tuned and pristine electron doped $SrTiO_3$. Tuning electron doped $SrTiO_3$ towards ferroelectricity enhances the T_c for optimally and under-doped samples while over-doped samples (uniaxial and epitaxial stress) show similar T_c compared to pristine samples.

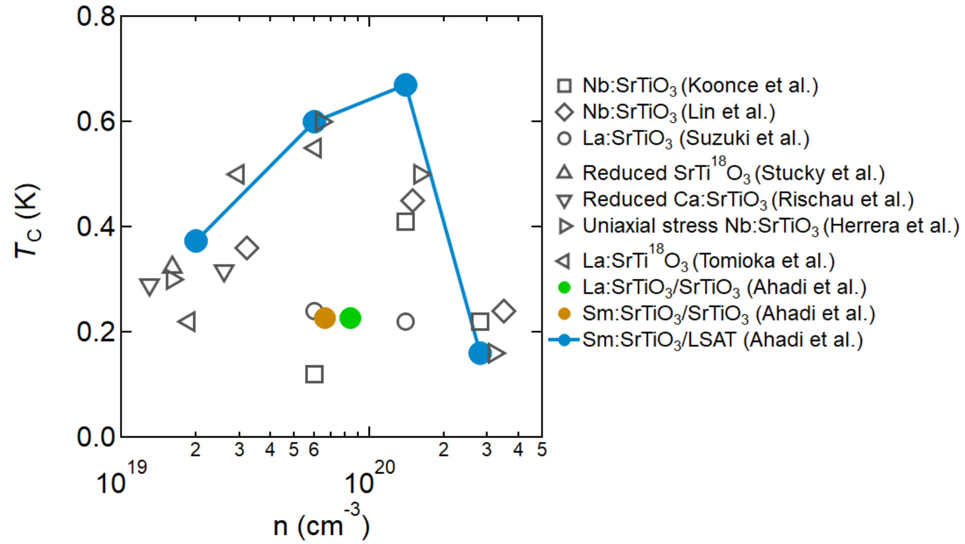

Figure 4.12. Superconducting critical temperature (T_C) with carrier density for electron doped $SrTiO_3$ from literature (Koonce *et al*. [81], Lin *et al.* [12], Suzuki *et al*. [79], Stucky *et al*. [104], and Rischau *et al*. [82], Herrera *et al*. [105], Tomioka *et al*. [128] and Ahadi *et al*. [60]). A significant enhancement of T_C is observed for tuned $SrTiO_3$ towards ferroelectricity at optimally and under-doped $SrTiO_3$, emphasizing importance of long-range ferroelectric order for pairing. Over-doped tuned $SrTiO_3$ samples, where long-range ferroelectric order is screened by charge carriers perform like pristine $SrTiO_3$.

Experimental results in Fig. 4.12 show up to 100% enhancement in critical temperature of superconductivity in $SrTiO_3$ tuned towards the ferroelectric ground state using epitaxial stress [60], uniaxial stress [105], chemical substitution [82] and isotope substitution [104,106,120]. Ferroelectric enhancement of superconductivity in tuned $SrTiO_3$ suggests the critical role of proximity to ferroelectric order in pairing and impacts theoretical proposals of superconductivity in $SrTiO_3$.

Similar to cuprates [118,119] and heavy fermions [227,228] where low

energy spin excitations in the vicinity of a magnetic quantum criticality are invoked to explain superconductivity, recently, quantum fluctuations of the ferroelectric mode have been proposed to explain superconductivity in $SrTiO_3$ [100,101]. In this model soft mode fluctuations are introduced as the origin for pairing interactions in $SrTiO_3$. It is emphasized recently that coupling to soft transverse mode is negligible, especially in dilute regime [14]. Also, tuning the system away from ferroelectric quantum criticality must suppress the superconducting order parameter. Here, combination of enhanced superconductivity deep inside ferroelectric state, i.e. far from quantum critical point, and premature termination of superconducting dome at the ferroelectric phase boundary (Fig. 4.11) suggests importance of ferroelectricity for enhancing superconductivity but do not support quantum fluctuations of the ferroelectric mode as a pairing mechanism.

4.7. Critical field of superconductivity

Longitudinal resistance was measured under sweeping applied out-of-plane magnetic field at different temperatures (Fig. 4.13) to calculate the superconducting upper critical magnetic field (H_{C2}). The H_{C2} at 50 mK for $n_H^{300K} = 2 \times 10^{19}\mathrm{cm}^{-3}, 6 \times 10^{19}\mathrm{cm}^{-3}, 1.4 \times 10^{20}\mathrm{cm}^{-3}$, and $2.8 \times 10^{20}\mathrm{cm}^{-3}$ carrier density, are 0.83 T, 1.75 T, 0.91 T, and 0.07 T, respectively. H_{C2} is calculated as the crossing point of the linear extrapolations of the slope of transition and the normal state. Here a drastic variation of H_{C2}, far larger than T_C variation, is reported with carrier density.

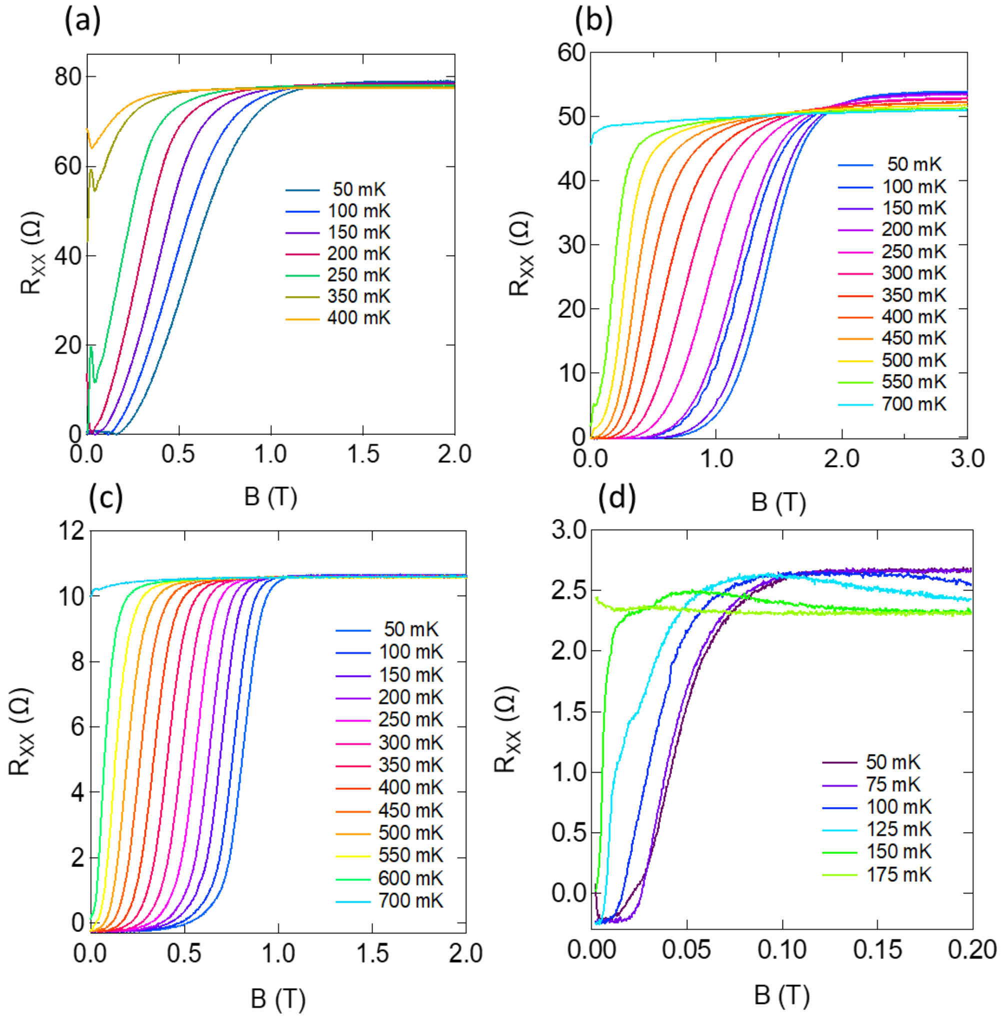

Figure 4.13. Longitudinal magnetoresistance at different temperatures and carrier concentrations. The longitudinal magnetoresistance for Sm-doped $SrTiO_3$ grown epitaxially on LSAT with $n_H^{300K} = (a)\ 2 \times 10^{19} cm^{-3}, (b)\ 6 \times 10^{19} cm^{-3}, (c)\ 1.4 \times 10^{20} cm^{-3}$, and $(d)\ 2.8 \times 10^{20} cm^{-3}$ carrier concentrations.

Figure 4.14 shows H_{C2} at different temperatures and carrier densities Here H_{C2} shows a drastically large value for under-doped sample ($n_H^{300K} = 6 \times 10^{19} \mathrm{cm}^{-3}$) and over one order of magnitude larger than previous reports for

$SrTiO_3$ [79,104]. The over-doped sample shows H_{C2} value like pristine $SrTiO_3$ previously reported in the literature [79]. The relation $H_{C2} = H_{C2}(0)\frac{1-t^2}{1+t^2}$, where $t = T/T_C$, is shown in dashed line. Similar behavior is also previously reported for La-doped $SrTiO_3$ [247].

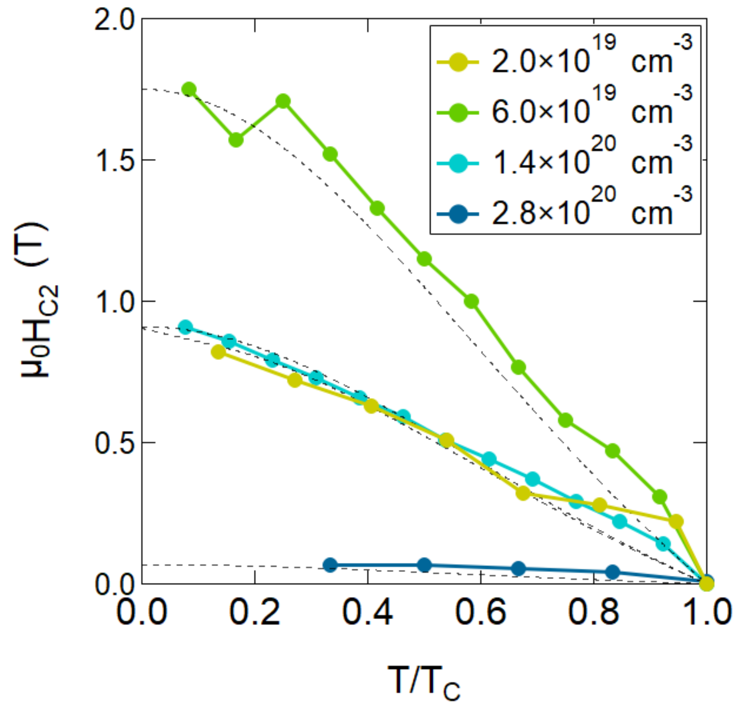

Figure 4.14. Upper critical magnetic field (H_{C2}) with normalized temperature and carrier concentration. The H_{C2} for Sm-doped $SrTiO_3$ grown epitaxially on LSAT with $n_H^{300K} = 2\times10^{19}\text{cm}^{-3}, 6\times10^{19}\text{cm}^{-3}, 1.4\times10^{20}\text{cm}^{-3}$, and $2.8\times10^{20}\text{cm}^{-3}$ carrier concentrations.

Furthermore, the scaling behavior of upper critical field does not follow the quadratic BCS prediction ($H_{C2}\sim {T_C}^2$). Table 4.1 compares the values derived for the T_C, H_{C2}, superconducting gap ($\Delta = 1.75\ k_BT_C$, where k_B is Boltzman's constant)

and superconducting coherence length ($\xi_0 = \sqrt{\phi_0/2\pi H_{C2}}$, where ϕ_0 is the magnetic quantum flux). The extracted coherence length is smaller than film thickness, confirming 3D superconducting states for all samples. Here, both Bohr radius and average size of Cooper pairs are much larger than Sm-Sm (~1-3 nm) distance.

Table 4.1. Values for T_C, H_{C2}, Δ, and ξ extracted for the three Sm-doped $SrTiO_3$ films on LSAT with different carrier densities.

$n_{3D}^{300K} \times 10^{19}(cm^{-3})$	T_C (K)	H_{C2} at 50 mK (T)	Δ (μeV)	ξ_0 (nm)
2	0.37	0.83	56	18
6	0.60	1.75	90	42
14	0.67	0.91	100	67
28	0.16	0.07	20	149

The first conclusion from these results is that tuning $SrTiO_3$ towards ferroelectricity, regardless of the tuning method, enhances superconductivity. Also, the increase in T_c by mentioned tuning methods is not simply strain, chemical or isotope substitution effects like modification of phonon modes. If this was the case over-doped samples also should exhibit enhanced T_c. Furthermore, BCS weak coupling limit predicts slight suppression of superconductivity with ^{18}O substitution. SHG results for epitaxially strained films clearly show that only samples deep into ferroelectric state display significant enhancement of superconductivity. Hitherto, quantum fluctuations of ferroelectric mode were

invoked to explain superconductivity in $SrTiO_3$ [100]. Accordingly, an exponential suppression of superconducting order parameter is expected with system tuned deeper inside ferroelectric state. Here, conversely, epitaxially strained $SrTiO_3$ films deep into ferroelectric state (ferroelectric T_c>40 K) show enhanced pairing which is at odds with theory of quantum criticality [9]. Seems that the interactions responsible for pairing are screened with increasing charge carriers suppressing superconducting order parameter in heavily doped samples. The results shown here strongly support the major role played by ferroelectric order in enhancing $SrTiO_3$ superconductivity.

4.8. Superconductivity emerging from ferroelectric state: possibility of unconventional parity and topological superconductivity

Finally, I discuss the possibility of unconventional parity and topological superconductivity in $SrTiO_3$. A nonzero Chern number is predicted in 2D Rashba superconductors under perpendicular magnetic field [248,249]. While the ferroelectric superconducting state in $SrTiO_3$ satisfies the symmetry conditions for topological superconductivity, i.e. broken inversion and time reversal symmetries, the condition for a nonzero Chern number ($\sqrt{(4t+\mu)^2+|\Delta|^2} < \mu_B H_z < \sqrt{\mu^2+|\Delta|^2}$) may fall outside the superconducting region, i.e. above H_{C2} [108]. A more recent theoretical study predicts Weyl topological superconductivity in applied magnetic fields exceeding Pauli-Chandrasekhar-Clogston limit [242]. Superconductivity above this limit is observed experimentally in $SrTiO_3$ [80]. Here, the sample with n_{3D}=0.6×10^{20} cm^{-3} exceeds this limit (Fig. 4.15).

Superconductivity emerging from ferroelectricity in $SrTiO_3$ is a promising candidate for topological superconductivity and anyons with non-abelian excitations.

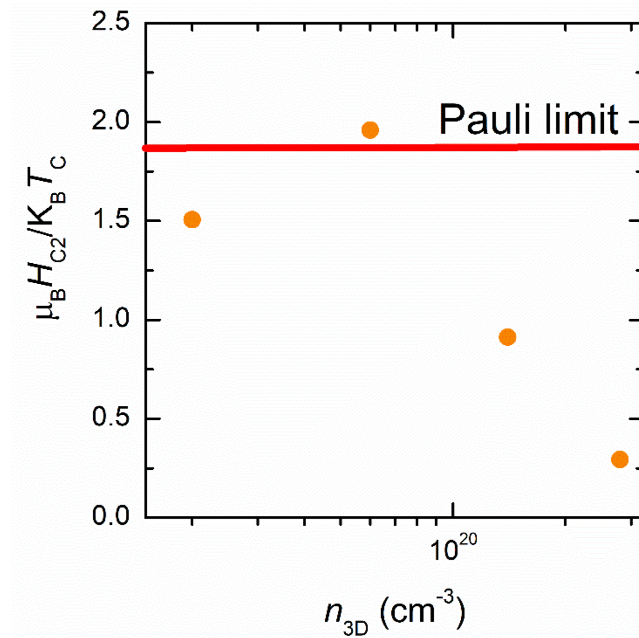

Figure 4.15. Exceeding the Pauli-Chandrasekhar-Clogston limit, $\mu_B H_{C2}/K_B T_C$=1.84. The under-doped sample with n_{3D}=0.6×10^{20} cm^{-3} exceeds the Pauli-Chandrasekhar-Clogston limit with out-of-plane applied magnetic field.

Chapter 5. Conclusions and future directions

5.1. Carrier density control of Berry phases and magnetism in $EuTiO_3$

Chapter 2 establishes the importance of antiferromagnetic order as a unique test-bed for topological phases of matter. A strong anomalous and topological Hall effects are observed in Sm-doped $EuTiO_3$ films epitaxially strained to LSAT substrate. An antiferromagnetic order is observed in these heterostructures, regardless of carrier density, using neutron diffraction. The effect of carrier density, i.e. Fermi energy, is studied extensively. At a critical carrier density ($\sim 5 \times 10^{20}$ cm^{-3}) both intrinsic anomalous and topological Hall signals go through a sign change. The intrinsic anomalous and topological Hall effects are originated by momentum space and spin texture Berry phases, respectively, and similar carrier density dependence highlights an intertwined relationship between band structure and spin texture topologies. The magnetization of these samples also shows a carrier density dependence with a significant enhancement around the critical carrier density ($\sim 5 \times 10^{20}$ cm^{-3}). A sign change in intrinsic anomalous Hall effect hints Fermi surface passing a Weyl node which is confirmed by DFT calculations. It is also shown that a magnetic field can systematically control the electronic state symmetry in anisotropic magnetoresistance. AMR shows a symmetry lowering, from four-fold to two-fold, with increasing magnetic field, highlighting significance of magnetic field in tuning electronic states. A two-dimensional electron system is shown to form at interface of $SmTiO_3$/$EuTiO_3$. In these heterostructures intrinsic anomalous and topological Hall effects are completely decoupled and behave differently with temperature.

An *in-situ* and reversible control of anomalous and topological Hall effects has possible applications in spintronics. Topologically nontrivial materials with large Berry curvatures are typically semimetals with very large carrier densities ($\sim 10^{22}$ cm^{-3}) beyond gate dielectric control. Combination of relatively low carrier densities ($\sim 10^{20}$ cm^{-3}) and strong carrier concentration dependence of Berry curvatures and magnetization provides a rare opportunity for a field effect control of intrinsic anomalous and topological Hall effects and magnetism in $EuTiO_3$. Two-dimensional electron systems at the interface of $R$$TiO_3$/$EuTiO_3$ also show both intrinsic anomalous and topological Hall effects. A top, side or even bottom-gated geometries can change chemical potential significantly, controlling intrinsic anomalous and topological Hall effects. $R$$TiO_3$ can be used as both gate dielectric and electron donor in case of a top-gated structure. A successful implementation of such device provides the unique possibility of an *in-situ* and reversible control of Berry phases using electric field.

5.2. Metal-insulator transitions at $SmTiO_3$/$SrTiO_3$ interface

Chapter 3 establishes the importance of $R$$TiO_3$ thickness for two-dimensional electron liquid transport behavior in $R$$TiO_3$/$SrTiO_3$. Chapter 3 is divided into two parts. In first part, a reversible metal-insulator transition with extremely large carrier modulation is observed using applied electric field in a top-gated $SmTiO_3$/$SrTiO_3$ heterostructure. Gate leakage dominates transport near metallic state, making impossible to have a complete transition. In second part,

heterostructures of $SmTiO_3/SrTiO_3$ are studied below the Mott-Ioffe-Regel limit at low temperatures. These samples show a very sharp metal-insulator transition in a narrow temperature window which is tunable up to vicinity of room temperature with carrier density and $SmTiO_3$ and $SrTiO_3$ thicknesses. Small sheet resistance and large carrier density of metallic state rule out Anderson localization and Wigner crystallization, respectively. One possible explanation could be strain-induced ferroelectric transition in $SrTiO_3$ pushing electrons toward polar interface.

The main barrier for a robust and reversible gate-induced metal-insulator transition is the relatively large gate leakage due to combination of large carrier density and thin gate dielectric. Different device geometries like side or bottom gate structures can be helpful in addressing the gate leakage issue. Fabricating three terminal field effect devices based on $SmTiO_3$(3u.c.s)/$SrTiO_3$ with thicker $SrTiO_3$ can also enhance carrier mobility and shift the balance towards metallic state, making a complete and robust gate-induced metal-insulator transition possible. The important open question is the nature of temperature-triggered metal-insulator transition in $SmTiO_3/SrTiO_3$ heterostructures. Second harmonic generation study can potentially shed light on possible ferroelectric nature of this transition.

5.3. Superconductivity intertwined with ferroelectricity in $SrTiO_3$

Chapter 4 makes the case for ferroelectric enhancement of superconductivity in epitaxially strained $SrTiO_3$ films. Superconductivity emerging

from ferroelectricity in $SrTiO_3$ shows a significant enhancement in critical temperature and critical field. More specifically, samples deep into ferroelectric state (T_c=92 K for $n_{3D}=0.6\times10^{20}$ cm^{-3} and T_c=39 K for $n_{3D}=1.4\times10^{20}$ cm^{-3}) show a factor of two enhancement in critical temperature of superconductivity while over-doped film ($n_{3D}=2.8\times10^{20}$ cm^{-3}) behaves very similar to unstrained samples. The pairing enhancement cannot be a simple strain effect, e.g. strain modification of phonon modes, since all films have similar strain condition. The sharp decrease in superconducting critical temperature on the over-doped side coincides with the demise of ferroelectric state, where screening by electrons overcomes any tendency toward ferroelectric ordering. Combination of enhanced superconductivity far from quantum critical point, i.e. deep inside ferroelectric state, and premature termination of superconducting dome at the ferroelectric phase boundary underlines importance of ferroelectric order in enhancing superconductivity and excludes possibility of quantum fluctuations of the ferroelectric mode as pairing mechanism. Furthermore, the superconducting dome only shifts up with ferroelectric order and keeps its qualitative shape with ferroelectric order.

Many important open questions remain. For example, whether and, if yes, how Sm *f* electrons interact with each other? Why Sm impurities do not suppress superconducting order parameter? Or how other rare earth impurities affect superconducting order parameter? Superconductivity, depending on the carrier density, exceeds Pauli-Chandrasekhar-Clogston limit in these films which could be a signature for unconventional parity of superconducting order parameter. A

topological Weyl superconducting state hosting Majorana Fermions is predicted when superconductivity emerges from ferroelectricity in $SrTiO_3$ [107]. Finally, investigating parity of superconducting order parameter in these heterostructures would be interesting and can answer the longstanding question about nature of superconductivity in $SrTiO_3$ with potential application for topological quantum computation.

Bibliography

[1] H. D. Megaw, C. N. W. Darlington, and IUCr, Acta Crystallogr. Sect. A **31**, 161 (1975).

[2] P. M. Woodward, Acta Crystallogr. Sect. B Struct. Sci. **53**, 32 (1997).

[3] S. Stemmer and S. James Allen, Annu. Rev. Mater. Res. **44**, 151 (2014).

[4] J. H. Ngai, F. J. Walker, and C. H. Ahn, Annu. Rev. Mater. Res. **44**, 1 (2014).

[5] H. Y. Hwang, Y. Iwasa, M. Kawasaki, B. Keimer, N. Nagaosa, and Y. Tokura, Nat. Mater. **11**, 103 (2012).

[6] J. Mannhart, D. H. A. Blank, H. Y. Hwang, A. J. Millis, and J.-M. Triscone, MRS Bull. **33**, 1027 (2008).

[7] S. Stemmer and A. J. Millis, MRS Bull. **38**, 1032 (2013).

[8] K. A. Müller and H. Burkard, Phys. Rev. B **19**, 3593 (1979).

[9] S. E. Rowley, L. J. Spalek, R. P. Smith, M. P. M. Dean, M. Itoh, J. F. Scott, G. G. Lonzarich, and S. S. Saxena, Nat. Phys. **10**, 367 (2014).

[10] K. van Benthem, C. Elsässer, and R. H. French, J. Appl. Phys. **90**, 6156 (2001).

[11] J. F. Schooley, W. R. Hosler, and M. L. Cohen, Phys. Rev. Lett. **12**, 474 (1964).

[12] X. Lin, G. Bridoux, A. Gourgout, G. Seyfarth, S. Krämer, M. Nardone, B. Fauqué, and K. Behnia, Phys. Rev. Lett. **112**, 207002 (2014).

[13] X. Lin, Z. Zhu, B. Fauqué, and K. Behnia, Phys. Rev. X **3**, 021002 (2013).

[14] J. Ruhman and P. A. Lee, Phys. Rev. B **94**, 224515 (2016).

[15] Y. Takada, J. Phys. Soc. Japan **45**, 786 (1978).

[16] T. Katsufuji and H. Takagi, Phys. Rev. B **64**, 054415 (2001).

[17] J. H. Lee, L. Fang, E. Vlahos, X. Ke, Y. W. Jung, L. F. Kourkoutis, J.-W. Kim, P. J. Ryan, T. Heeg, M. Roeckerath, V. Goian, M. Bernhagen, R. Uecker, P. C. Hammel, K. M. Rabe, S. Kamba, J. Schubert, J. W. Freeland, D. A. Muller, C. J. Fennie, P. Schiffer, V. Gopalan, E. Johnston-Halperin, and D. G. Schlom, Nature **466**, 954 (2010).

[18] J. H. Lee, X. Ke, N. J. Podraza, L. F. Kourkoutis, T. Heeg, M. Roeckerath, J. W. Freeland, C. J. Fennie, J. Schubert, D. A. Muller, P. Schiffer, and D. G. Schlom, Appl. Phys. Lett. **94**, 212509 (2009).

[19] T. Katsufuji and Y. Tokura, Phys. Rev. B **60**, R15021 (1999).

[20] Y. Ohuchi, Y. Kozuka, M. Uchida, K. Ueno, A. Tsukazaki, and M. Kawasaki, Phys. Rev. B **91**, 245115 (2015).

[21] T. Katsufuji and Y. Tokura, Phys. Rev. B **60**, R15021 (1999).

[22] K. S. Takahashi, M. Onoda, M. Kawasaki, N. Nagaosa, and Y. Tokura, Phys. Rev. Lett. **103**, 057204 (2009).

[23] K. Ahadi, Z. Gui, Z. Porter, J. W. Lynn, Z. Xu, S. D. Wilson, A. Janotti, and S. Stemmer, APL Mater. **6**, (2018).

[24] Y. Kususe, H. Murakami, K. Fujita, I. Kakeya, M. Suzuki, S. Murai, and K. Tanaka, Jpn. J. Appl. Phys. **53**, 05FJ07 (2014).

[25] E. Pavarini, A. Yamasaki, J. Nuss, and O. K. Andersen, New J. Phys. **7**, 188 (2005).

[26] M. Mochizuki and M. Imada, Phys. Rev. Lett. **91**, 167203 (2003).

[27] H. D. Zhou and J. B. Goodenough, J. Phys. Condens. Matter **17**, 7395 (2005).

[28] D. G. Schlom, APL Mater. **3**, 062403 (2015).

[29] J. Falson, D. Maryenko, Y. Kozuka, A. Tsukazaki, and M. Kawasaki, Appl. Phys. Express **4**, 091101 (2011).

[30] Y. Kozuka, A. Tsukazaki, and M. Kawasaki, Appl. Phys. Rev. **1**, 011303 (2014).

[31] A. Tsukazaki, A. Ohtomo, T. Kita, Y. Ohno, H. Ohno, and M. Kawasaki, Science **315**, 1388 (2007).

[32] T. A. Cain, A. P. Kajdos, and S. Stemmer, Appl. Phys. Lett. **102**, 182101 (2013).

[33] Y. Kozuka, Y. Hikita, C. Bell, and H. Y. Hwang, Appl. Phys. Lett. **97**, 012107 (2010).

[34] H. P. Nair, Y. Liu, J. P. Ruf, N. J. Schreiber, S.-L. Shang, D. J. Baek, B. H. Goodge, L. F. Kourkoutis, Z.-K. Liu, K. M. Shen, and D. G. Schlom, APL Mater. **6**, 046101 (2018).

[35] A. P. Mackenzie, J. W. Reiner, A. W. Tyler, L. M. Galvin, S. R. Julian, M. R. Beasley, T. H. Geballe, and A. Kapitulnik, Phys. Rev. B **58**, R13318 (1998).

[36] L. Klein, Y. Kats, A. F. Marshall, J. W. Reiner, T. H. Geballe, M. R. Beasley, and A. Kapitulnik, Phys. Rev. Lett. **84**, 6090 (2000).

[37] Q. X. Jia, F. Chu, C. D. Adams, X. D. Wu, M. Hawley, J. H. Cho, A. T. Findikoglu, S. R. Foltyn, J. L. Smith, and T. E. Mitchell, J. Mater. Res. **11**, 2263 (1996).

[38] J. A. Moyer, C. Eaton, and R. Engel-Herbert, Adv. Mater. **25**, 3578 (2013).

[39] H. Koinuma, M. Yoshimoto, H. Nagata, and T. Tsukahara, Solid State Commun. **80**, 9 (1991).

[40] W. C. Sheets, B. Mercey, and W. Prellier, Appl. Phys. Lett. **91**, 192102 (2007).

[41] T. Yamasaki, K. Ueno, A. Tsukazaki, T. Fukumura, and M. Kawasaki, Appl. Phys. Lett. **98**, 082116 (2011).

[42] A. Schmehl, V. Vaithyanathan, A. Herrnberger, S. Thiel, C. Richter, M. Liberati, T. Heeg, M. Röckerath, L. F. Kourkoutis, S. Mühlbauer, P. Böni, D. A. Muller, Y. Barash, J. Schubert, Y. Idzerda, J. Mannhart, and D. G. Schlom, Nat. Mater. **6**, 882 (2007).

[43] M. . Herman, W. Richter, and H. Sitter, *Epitaxy* (2003).

[44] J. Y. Tsao, *Materials Fundamentals of Molecular Beam Epitaxy* (Academic Press, 1993).

[45] C. . Theis, J. Yeh, D. . Schlom, M. . Hawley, and G. . Brown, Thin Solid Films **325**, 107 (1998).

[46] E. S. Hellman and E. H. Hartford, J. Vac. Sci. Technol. B Microelectron. Nanom. Struct. **8**, 332 (1990).

[47] B. Jalan, R. Engel-Herbert, N. J. Wright, and S. Stemmer, J. Vac. Sci. Technol. A Vacuum, Surfaces, Film. **27**, 461 (2009).

[48] B. Jalan, P. Moetakef, and S. Stemmer, Appl. Phys. Lett. **95**, 032906 (2009).

[49] K. Ahadi, L. Galletti, and S. Stemmer, Appl. Phys. Lett. **111**, 172403 (2017).

[50] K. Ahadi and S. Stemmer, Phys. Rev. Lett. **118**, 236803 (2017).

[51] K. Ahadi, H. Kim, and S. Stemmer, APL Mater. **6**, 056102 (2018).

[52] A. P. Kajdos, D. G. Ouellette, T. A. Cain, and S. Stemmer, Appl. Phys. Lett. **103**, 082120 (2013).

[53] M. Brahlek, L. Zhang, C. Eaton, H.-T. Zhang, and R. Engel-Herbert, Appl. Phys. Lett. **107**, 143108 (2015).

[54] A. Prakash, P. Xu, X. Wu, G. Haugstad, X. Wang, and B. Jalan, J. Mater.

Chem. C **5**, 5730 (2017).

[55] P. B. Marshall, K. Ahadi, H. Kim, and S. Stemmer, Phys. Rev. B **97**, (2018).

[56] P. B. Marshall, H. Kim, K. Ahadi, and S. Stemmer, APL Mater. **5**, (2017).

[57] K. Ahadi, Z. Gui, Z. Porter, J. W. Lynn, Z. Xu, S. D. Wilson, A. Janotti, and S. Stemmer, APL Mater. **6**, 056105 (2018).

[58] K. Ahadi, X. Lu, S. Salmani-Rezaie, P. B. Marshall, J. M. Rondinelli, and S. Stemmer, Phys. Rev. B **99**, 041106 (2019).

[59] K. Ahadi, O. F. Shoron, P. B. Marshall, E. Mikheev, and S. Stemmer, Appl. Phys. Lett. **110**, 062104 (2017).

[60] K. Ahadi, L. Galletti, Y. Li, S. Salmani-Rezaie, W. Wu, and S. Stemmer, Sci. Adv. **5**, eaaw0120 (2019).

[61] R. Russell, N. Ratcliff, K. Ahadi, L. Dong, S. Stemmer, and J. W. Harter, Phys. Rev. Mater. **3**, 091401 (2019).

[62] N. W. Ashcroft and N. D. Mermin, *Solid State Physics* (n.d.).

[63] J. Bass, W. P. Pratt, and P. A. Schroeder, Rev. Mod. Phys. **62**, 645 (1990).

[64] E. Grüneisen, Ann. Phys. **408**, 530 (1933).

[65] J. . Collins and M. Ziman, Proc. R. Soc. London. Ser. A. Math. Phys. Sci. **264**, 60 (1961).

[66] M. Bailyn, Phys. Rev. **112**, 1587 (1958).

[67] R. Peierls, Ann. Phys. **396**, 121 (1930).

[68] A. Verma, A. P. Kajdos, T. A. Cain, S. Stemmer, and D. Jena, Phys. Rev. Lett. **112**, 216601 (2014).

[69] L. D. Landau and S. I. Pekar, Eksp. Teor. Fiz **18**, 419 (1948).

[70] H. P. R. Frederikse and W. R. Hosler, Phys. Rev. **161**, 822 (1967).

[71] A. J. Schofield, (1998).

[72] X. Lin, B. Fauqué, and K. Behnia, Science (80-.). **349**, (2015).

[73] E. Mikheev, B. Himmetoglu, A. P. Kajdos, P. Moetakef, T. A. Cain, C. G. Van de Walle, and S. Stemmer, Appl. Phys. Lett. **106**, 062102 (2015).

[74] H. v. Löhneysen, A. Rosch, M. Vojta, and P. Wölfle, Rev. Mod. Phys. **79**, 1015 (2007).

[75] P. A. Lee and T. V. Ramakrishnan, Rev. Mod. Phys. **57**, 287 (1985).

[76] D. van der Marel, J. L. M. van Mechelen, and I. I. Mazin, Phys. Rev. B **84**, 205111 (2011).

[77] L. F. Mattheiss, Phys. Rev. B **6**, 4718 (1972).

[78] J. Son, P. Moetakef, B. Jalan, O. Bierwagen, N. J. Wright, R. Engel-Herbert, and S. Stemmer, Nat. Mater. **9**, 482 (2010).

[79] H. Suzuki, H. Bando, Y. Ootuka, I. H. Inoue, T. Yamamoto, K. Takahashi, and Y. Nishihara, J. Phys. Soc. Japan **65**, 1529 (1996).

[80] Y. Ayino, J. Yue, T. Wang, B. Jalan, and V. S. Pribiag, (2018).

[81] C. S. Koonce, M. L. Cohen, J. F. Schooley, W. R. Hosler, and E. R. Pfeiffer, Phys. Rev. **163**, 380 (1967).

[82] C. W. Rischau, X. Lin, C. P. Grams, D. Finck, S. Harms, J. Engelmayer, T. Lorenz, Y. Gallais, B. Fauqué, J. Hemberger, and K. Behnia, Nat. Phys. **13**, 643 (2017).

[83] A. Spinelli, M. A. Torija, C. Liu, C. Jan, and C. Leighton, Phys. Rev. B **81**, 155110 (2010).

[84] H. Kim, P. B. Marshall, K. Ahadi, T. E. Mates, E. Mikheev, and S. Stemmer, Phys. Rev. Lett. **119**, 186803 (2017).

[85] C. C. Hays, J.-S. Zhou, J. T. Markert, and J. B. Goodenough, *Electronic Transition in La 1x Sr x TiO 3* (n.d.).

[86] P. Moetakef and T. A. Cain, Thin Solid Films **583**, 129 (2015).

[87] A. C. Komarek, H. Roth, M. Cwik, W.-D. Stein, J. Baier, M. Kriener, F. Bourée, T. Lorenz, and M. Braden, Phys. Rev. B **75**, 224402 (2007).

[88] E. Mikheev, Tunable Dielectric Response, Resistive Switching, and Unconventional Transport in SrTiO3, UC Santa Barbara, 2016.

[89] M. Itoh, R. Wang, Y. Inaguma, T. Yamaguchi, Y.-J. Shan, and T. Nakamura, Phys. Rev. Lett. **82**, 3540 (1999).

[90] J. G. Bednorz and K. A. Müller, Phys. Rev. Lett. **52**, 2289 (1984).

[91] H. Wu and W. Z. Shen, Phys. Rev. B **73**, 094115 (2006).

[92] N. A. Pertsev, A. K. Tagantsev, and N. Setter, Phys. Rev. B **61**, R825 (2000).

[93] J. H. Haeni, P. Irvin, W. Chang, R. Uecker, P. Reiche, Y. L. Li, S. Choudhury, W. Tian, M. E. Hawley, B. Craigo, A. K. Tagantsev, X. Q. Pan, S. K. Streiffer, L. Q. Chen, S. W. Kirchoefer, J. Levy, and D. G. Schlom, Nature **430**, 758 (2004).

[94] H. Uwe and T. Sakudo, Phys. Rev. B **13**, 271 (1976).

[95] J. F. Schooley, W. R. Hosler, and M. L. Cohen, Phys. Rev. Lett. **12**, 474 (1964).

[96] S. Sachdev, Science (80-.). **336**, 1510 (2012).

[97] D. J. Scalapino, Rev. Mod. Phys. **84**, 1383 (2012).

[98] B. Keimer, S. A. Kivelson, M. R. Norman, S. Uchida, and J. Zaanen, Nature **518**, 179 (2015).

[99] J. M. Tranquada, B. J. Sternlieb, J. D. Axe, Y. Nakamura, and S. Uchida, Nature **375**, 561 (1995).

[100] J. M. Edge, Y. Kedem, U. Aschauer, N. A. Spaldin, and A. V. Balatsky, Phys. Rev. Lett. **115**, 247002 (2015).

[101] K. Dunnett, A. Narayan, N. A. Spaldin, and A. V. Balatsky, Phys. Rev. B **97**, 144506 (2018).

[102] P. Wölfle and A. V. Balatsky, Phys. Rev. B **98**, 104505 (2018).

[103] S. E. Rowley, C. Enderlein, J. F. de Oliveira, D. A. Tompsett, E. B. Saitovitch, S. S. Saxena, and G. G. Lonzarich, (2018).

[104] A. Stucky, G. W. Scheerer, Z. Ren, D. Jaccard, J.-M. Poumirol, C. Barreteau, E. Giannini, and D. van der Marel, Sci. Rep. **6**, 37582 (2016).

[105] C. Herrera, J. Cerbin, K. Dunnett, A. V. Balatsky, and I. Sochnikov, (2018).

[106] Y. Tomioka, N. Shirakawa, K. Shibuya, and I. H. Inoue, Nat. Commun. **10**, 738 (2019).

[107] S. Kanasugi and Y. Yanase, (2019).

[108] S. Kanasugi and Y. Yanase, Phys. Rev. B **98**, 024521 (2018).

[109] X. Lin, G. Bridoux, A. Gourgout, G. Seyfarth, S. Krämer, M. Nardone, B. Fauqué, and K. Behnia, Phys. Rev. Lett. **112**, 207002 (2014).

[110] J. Bardeen, L. N. Cooper, and J. R. Schrieffer, Phys. Rev. **108**, 1175 (1957).

[111] M. Tinkham, *Introduction to Superconductivity* (Dover Publications, 2004).

[112] J. Appel, Phys. Rev. **180**, 508 (1969).

[113] L. P. Gor'kov, Proc. Natl. Acad. Sci. U. S. A. **113**, 4646 (2016).

[114] A. Mooradian and G. B. Wright, Phys. Rev. Lett. **16**, 999 (1966).

[115] E. . Steigmeier and G. Harbeke, Solid State Commun. **8**, 1275 (1970).

[116] W. Zhong, R. D. King-Smith, and D. Vanderbilt, Phys. Rev. Lett. **72**, 3618 (1994).

[117] R. E. Cohen, Nature **358**, 136 (1992).

[118] S. Sachdev, Phys. C Supercond. Its Appl. **470**, S4 (2010).

[119] B. Michon, C. Girod, S. Badoux, J. Kačmarčík, Q. Ma, M. Dragomir, H. A. Dabkowska, B. D. Gaulin, J.-S. Zhou, S. Pyon, T. Takayama, H. Takagi, S. Verret, N. Doiron-Leyraud, C. Marcenat, L. Taillefer, and T. Klein, Nature **567**, 218 (2019).

[120] W. Rischau, D. Pulmannova, G. Scheerer, E. Giannini, and D. Van Der Marel, Bull. Am. Phys. Soc. **Volume 64**, **Number 2**, (2019).

[121] R. J. Miller and C. B. Satterthwaite, Phys. Rev. Lett. **34**, 144 (1975).

[122] H. J. Bornemann, D. E. Morris, and H. B. Liu, Phys. C Supercond. **182**, 132 (1991).

[123] H. Uwe and T. Sakudo, Phys. Rev. B **13**, 271 (1976).

[124] U. Aschauer and N. A. Spaldin, J. Phys. Condens. Matter **26**, 122203 (2014).

[125] A. Verma, S. Raghavan, S. Stemmer, and D. Jena, Appl. Phys. Lett. **107**, 192908 (2015).

[126] R. C. Haislmaier, R. Engel-Herbert, and V. Gopalan, Appl. Phys. Lett. **109**, 032901 (2016).

[127] T. Wang, K. Ganguly, P. Marshall, P. Xu, and B. Jalan, Appl. Phys. Lett. **103**, 212904 (2013).

[128] Y. Tomioka, N. Shirakawa, K. Shibuya, and I. H. Inoue, Nat. Commun. **10**, 738 (2019).

[129] A. Ohtomo and H. Y. Hwang, Nature **427**, 423 (2004).

[130] A. F. Santander-Syro, O. Copie, T. Kondo, F. Fortuna, S. Pailhès, R. Weht, X. G. Qiu, F. Bertran, A. Nicolaou, A. Taleb-Ibrahimi, P. Le Fèvre, G. Herranz, M. Bibes, N. Reyren, Y. Apertet, P. Lecoeur, A. Barthélémy, and M. J. Rozenberg, Nature **469**, 189 (2011).

[131] N. Reyren, S. Thiel, A. D. Caviglia, L. F. Kourkoutis, G. Hammerl, C. Richter, C. W. Schneider, T. Kopp, A.-S. Rüetschi, D. Jaccard, M. Gabay, D. A. Muller, J.-M. Triscone, and J. Mannhart, Science **317**, 1196 (2007).

[132] M. Gabay and J.-M. Triscone, Nat. Phys. **13**, 624 (2017).

[133] J. A. Sulpizio, S. Ilani, P. Irvin, and J. Levy, Annu. Rev. Mater. Res. **44**, 117 (2014).

[134] G. Khalsa and A. H. Macdonald, Phys. Rev. B **86**, 125121 (2012).

[135] P. Moetakef, D. G. Ouellette, J. R. Williams, S. J. Allen, L. Balents, D. Goldhaber-Gordon, and S. Stemmer, Cit. Appl. Phys. Lett. Appl. Phys. Lett **101**, (2012).

[136] M. Huijben, A. Brinkman, G. Koster, G. Rijnders, H. Hilgenkamp, and D. H. A. Blank, Adv. Mater. **21**, 1665 (2009).

[137] A. D. Caviglia, S. Gariglio, N. Reyren, D. Jaccard, T. Schneider, M. Gabay, S. Thiel, G. Hammerl, J. Mannhart, and J.-M. Triscone, Nature **456**, 624 (2008).

[138] K. Ahadi, O. F. Shoron, P. B. Marshall, E. Mikheev, and S. Stemmer, Appl. Phys. Lett. **110**, (2017).

[139] N. F. MOTT, Rev. Mod. Phys. **40**, 677 (1968).

[140] M. Imada, A. Fujimori, and Y. Tokura, Rev. Mod. Phys. **70**, 1039 (1998).

[141] N. F. Mott, *The Basis OF the Electron Theory of Metals, with Special Reference to the Transition Metals* (n.d.).

[142] E. Wigner, Phys. Rev. **46**, 1002 (1934).

[143] S.-C. Ho, H.-J. Chang, C.-H. Chang, S.-T. Lo, G. Creeth, S. Kumar, I. Farrer, D. Ritchie, J. Griffiths, G. Jones, M. Pepper, and T.-M. Chen, Phys. Rev. Lett. **121**, 106801 (2018).

[144] J. H. De Boer, E. J. W. Verw'ey, and N. Laboratorium, *SEMI-CONDUCTORS WITH PARTIALLY AND WITH COMPLETELY FILLED 3d-LATTICE BANDS* (n.d.).

[145] E. Wigner, Trans. Faraday Soc. **34**, 678 (1938).

[146] J. Y. Zhang, J. Hwang, S. Raghavan, and S. Stemmer, Phys. Rev. Lett. **110**, 256401 (2013).

[147] J. Y. Zhang, C. A. Jackson, R. Chen, S. Raghavan, P. Moetakef, L. Balents, and S. Stemmer, Phys. Rev. B **89**, 075140 (2014).

[148] A. D. Caviglia, M. Gabay, S. Gariglio, N. Reyren, C. Cancellieri, and J.-M. Triscone, Phys. Rev. Lett. **104**, 126803 (2010).

[149] K. v. Klitzing, G. Dorda, and M. Pepper, Phys. Rev. Lett. **45**, 494 (1980).

[150] M. V. Berry, Proc. R. Soc. A Math. Phys. Eng. Sci. **392**, 45 (1984).

[151] X. Wang, J. R. Yates, I. Souza, and D. Vanderbilt, Phys. Rev. B **74**, 195118 (2006).

[152] D. J. Thouless, M. Kohmoto, M. P. Nightingale, and M. den Nijs, Phys. Rev. Lett. **49**, 405 (1982).

[153] R. Karplus and J. M. Luttinger, Phys. Rev. **95**, 1154 (1954).

[154] F. D. M. Haldane, Phys. Rev. Lett. **93**, 206602 (2004).

[155] S. Onoda, N. Sugimoto, and N. Nagaosa, Phys. Rev. B **77**, 165103 (2008).

[156] N. Nagaosa, J. Sinova, S. Onoda, A. H. MacDonald, and N. P. Ong, Rev. Mod. Phys. **82**, 1539 (2010).

[157] M. Onoda and N. Nagaosa, Phys. Rev. Lett. **90**, 206601 (2003).

[158] P. Bruno, V. K. Dugaev, and M. Taillefumier, Phys. Rev. Lett. **93**, 096806 (2004).

[159] Y. Shiomi, M. Mochizuki, Y. Kaneko, and Y. Tokura, Phys. Rev. Lett. **108**, 056601 (2012).

[160] Y. Shiomi, S. Iguchi, and Y. Tokura, Phys. Rev. B **86**, 180404 (2012).

[161] N. Nagaosa and Y. Tokura, Nat. Nanotechnol. **8**, 899 (2013).

[162] S. Mühlbauer, B. Binz, F. Jonietz, C. Pfleiderer, A. Rosch, A. Neubauer, R. Georgii, and P. Böni, Science (80-.). **323**, (2009).

[163] X. Z. Yu, N. Kanazawa, Y. Onose, K. Kimoto, W. Z. Zhang, S. Ishiwata, Y. Matsui, and Y. Tokura, Nat. Mater. **10**, 106 (2011).

[164] A. Neubauer, C. Pfleiderer, B. Binz, A. Rosch, R. Ritz, P. G. Niklowitz, and P. Böni, Phys. Rev. Lett. **102**, 186602 (2009).

[165] S. Chakraverty, T. Matsuda, H. Wadati, J. Okamoto, Y. Yamasaki, H. Nakao, Y. Murakami, S. Ishiwata, M. Kawasaki, Y. Taguchi, Y. Tokura, and H. Y. Hwang, Phys. Rev. B **88**, 220405 (2013).

[166] Y. Taguchi, Y. Oohara, H. Yoshizawa, N. Nagaosa, and Y. Tokura, Science **291**, 2573 (2001).

[167] A. O. Leonov and M. Mostovoy, Nat. Commun. **6**, 8275 (2015).

[168] J. Matsuno, N. Ogawa, K. Yasuda, F. Kagawa, W. Koshibae, N. Nagaosa, Y. Tokura, and M. Kawasaki, Sci. Adv. **2**, e1600304 (2016).

[169] Y. Ohuchi, J. Matsuno, N. Ogawa, Y. Kozuka, M. Uchida, Y. Tokura, and M. Kawasaki, Nat. Commun. **9**, 213 (2018).

[170] L. Šmejkal, Y. Mokrousov, B. Yan, and A. H. MacDonald, Nat. Phys. **14**, 242 (2018).

[171] L. Šmejkal, T. Jungwirth, and J. Sinova, Phys. Status Solidi - Rapid Res. Lett. **11**, 1700044 (2017).

[172] B. Jalan, R. Engel-Herbert, N. J. Wright, and S. Stemmer, J. Vac. Sci. Technol. A Vacuum, Surfaces, Film. **27**, 461 (2009).

[173] A. P. Kajdos and S. Stemmer, Appl. Phys. Lett. **105**, 191901 (2014).

[174] K. S. Takahashi, M. Onoda, M. Kawasaki, N. Nagaosa, and Y. Tokura, Phys. Rev. Lett. **103**, 057204 (2009).

[175] R. S. Perry, L. M. Galvin, S. A. Grigera, L. Capogna, A. J. Schofield, A. P. Mackenzie, M. Chiao, S. R. Julian, S. I. Ikeda, S. Nakatsuji, Y. Maeno, and C. Pfleiderer, Phys. Rev. Lett. **86**, 2661 (2001).

[176] J. Schiemer, L. J. Spalek, S. S. Saxena, C. Panagopoulos, T. Katsufuji, and M. A. Carpenter, EPL (Europhysics Lett. **109**, 57004 (2015).

[177] A. Shitade and N. Nagaosa, J. Phys. Soc. Japan **81**, 083704 (2012).

[178] W.-L. Lee, S. Watauchi, V. L. Miller, R. J. Cava, and N. P. Ong, *Dissipationless Anomalous Hall Current in the Ferromagnetic Spinel CuCr 2 Se 4-x Br X* (n.d.).

[179] T. Miyasato, N. Abe, T. Fujii, A. Asamitsu, S. Onoda, Y. Onose, N. Nagaosa, and Y. Tokura, Phys. Rev. Lett. **99**, 086602 (2007).

[180] C. Franz, F. Freimuth, A. Bauer, R. Ritz, C. Schnarr, C. Duvinage, T. Adams, S. Blügel, A. Rosch, Y. Mokrousov, and C. Pfleiderer, Phys. Rev. Lett. **112**, 186601 (2014).

[181] Z. Fang, N. Nagaosa, K. S. Takahashi, A. Asamitsu, R. Mathieu, T. Ogasawara, H. Yamada, M. Kawasaki, Y. Tokura, and K. Terakura, Science (80-.). **302**, 92 (2003).

[182] A. A. Burkov, Phys. Rev. Lett. **113**, 187202 (2014).

[183] Z. Porter, K. Ahadi, S. Stemmer, and S. D. Wilson, In-Preparation (n.d.).

[184] E. Mikheev, C. R. Freeze, B. J. Isaac, T. A. Cain, and S. Stemmer, Phys. Rev. B **91**, 165125 (2015).

[185] N. Kanazawa, Y. Onose, T. Arima, D. Okuyama, K. Ohoyama, S. Wakimoto, K. Kakurai, S. Ishiwata, and Y. Tokura, Phys. Rev. Lett. **106**, 156603 (2011).

[186] Y. Li, N. Kanazawa, X. Z. Yu, A. Tsukazaki, M. Kawasaki, M. Ichikawa, X. F. Jin, F. Kagawa, and Y. Tokura, Phys. Rev. Lett. **110**, 117202 (2013).

[187] N. D. Mermin and H. Wagner, Phys. Rev. Lett. **17**, 1133 (1966).

[188] P. Moetakef, T. A. Cain, D. G. Ouellette, J. Y. Zhang, D. O. Klenov, A. Janotti, C. G. Van de Walle, S. Rajan, S. J. Allen, and S. Stemmer, Appl. Phys. Lett. **99**, 232116 (2011).

[189] A. Ohtomo and H. Y. Hwang, Nature **427**, 423 (2004).

[190] S. Stemmer and A. J. Millis, MRS Bull. **38**, 1032 (2013).

[191] P. Zubko, S. Gariglio, M. Gabay, P. Ghosez, and J.-M. Triscone, Annu. Rev. Condens. Matter Phys. **2**, 141 (2011).

[192] P. A. Lee and T. V. Ramakrishnan, Rev. Mod. Phys. **57**, 287 (1985).

[193] T. Ando, A. B. Fowler, and F. Stern, Rev. Mod. Phys. **54**, 437 (1982).

[194] S. V Kravchenko and M. P. Sarachik, Reports Prog. Phys. **67**, 1 (2004).

[195] E. Abrahams, S. V. Kravchenko, and M. P. Sarachik, Rev. Mod. Phys. **73**, 251 (2001).

[196] M. Boucherit, O. Shoron, C. A. Jackson, T. A. Cain, M. L. C. Buffon, C. Polchinski, S. Stemmer, and S. Rajan, Appl. Phys. Lett. **104**, 182904 (2014).

[197] C. A. Jackson, J. Y. Zhang, C. R. Freeze, and S. Stemmer, (2014).

[198] E. Mikheev, S. Raghavan, and S. Stemmer, Appl. Phys. Lett. **107**, 072905 (2015).

[199] T. Shimizu, N. Gotoh, N. Shinozaki, and H. Okushi, Appl. Surf. Sci. **117–118**, 400 (1997).

[200] C. Bell, S. Harashima, Y. Kozuka, M. Kim, B. G. Kim, Y. Hikita, and H. Y. Hwang, (2009).

[201] S. V. Kravchenko, G. V. Kravchenko, J. E. Furneaux, V. M. Pudalov, and M. D'Iorio, Phys. Rev. B **50**, 8039 (1994).

[202] S. V. Kravchenko, W. E. Mason, G. E. Bowker, J. E. Furneaux, V. M. Pudalov, and M. D'Iorio, Phys. Rev. B **51**, 7038 (1995).

[203] S. V. Kravchenko, D. Simonian, M. P. Sarachik, W. Mason, and J. E. Furneaux, Phys. Rev. Lett. **77**, 4938 (1996).

[204] P. Moetakef, J. Y. Zhang, S. Raghavan, A. P. Kajdos, and S. Stemmer, J. Vac. Sci. Technol. A Vacuum, Surfaces, Film. **31**, 041503 (2013).

[205] A. L. Efros and B. I. Shklovskii, J. Phys. C Solid State Phys. **8**, L49 (1975).

[206] M. Lee, J. G. Massey, V. L. Nguyen, and B. I. Shklovskii, *Coulomb Gap in*

a Doped Semiconductor near the Metal-Insulator Transition: Tunneling Experiment and Scaling Ansatz (n.d.).

[207] M. A. Paalanen, T. F. Rosenbaum, ' ", G. A. Thomas, R. N. Bhatt, B. / I. Aboratories, and M. Iiill, *Critical Scaling of the Conductance in a Disordered Insulator* (n.d.).

[208] K. Ahadi and S. Stemmer, Phys. Rev. Lett. **118**, 236803 (2017).

[209] X. Lin, C. W. Rischau, L. Buchauer, A. Jaoui, B. Fauqué, and K. Behnia, Npj Quantum Mater. **2**, 41 (2017).

[210] Q. Tao, B. Loret, B. Xu, X. Yang, C. W. Rischau, X. Lin, B. B. Fauqué, M. J. Verstraete, and K. Behnia, Phys. Rev. B **94**, 35111 (2016).

[211] Y. Segal, K. F. Garrity, C. A. F. Vaz, J. D. Hoffman, F. J. Walker, S. Ismail-Beigi, and C. H. Ahn, (n.d.).

[212] P. Anderson, Phys. Rev. Lett. **67**, 2092 (1991).

[213] M. Blake and A. Donos, Phys. Rev. Lett. **114**, 021601 (2015).

[214] T. Chien, Z. Wang, and N. Ong, Phys. Rev. Lett. **67**, 2088 (1991).

[215] J. A. Clayhold, Z. H. Zhang, and A. J. Schofield, J. Phys. Chem. Solids **59**, 2114 (1998).

[216] J. Son, P. Moetakef, J. M. LeBeau, D. Ouellette, L. Balents, S. J. Allen, and S. Stemmer, Appl. Phys. Lett. **96**, 062114 (2010).

[217] N. F. Mott, Philos. Mag. **26**, 1015 (1972).

[218] J. Torrance, P. Lacorre, A. Nazzal, E. Ansaldo, and C. Niedermayer, Phys. Rev. B **45**, 8209 (1992).

[219] F. J. Morin, Phys. Rev. Lett. **3**, 34 (1959).

[220] A. J. Hauser, E. Mikheev, N. E. Moreno, T. A. Cain, J. Hwang, J. Y. Zhang, and S. Stemmer, Appl. Phys. Lett. **103**, 182105 (2013).

[221] R. C. Neville, B. Hoeneisen, and C. A. Mead, J. Appl. Phys. **43**, 2124 (1972).

[222] S. J. Allen, B. Jalan, S. Lee, D. G. Ouellette, G. Khalsa, J. Jaroszynski, S. Stemmer, and A. H. MacDonald, Phys. Rev. B **88**, 045114 (2013).

[223] B. Tanatar and D. M. Ceperley, Phys. Rev. B **39**, 5005 (1989).

[224] P. Delugas, A. Filippetti, V. Fiorentini, D. I. Bilc, D. Fontaine, and P. Ghosez, Phys. Rev. Lett. **106**, 166807 (2011).

[225] E. Berg, M. S. Rudner, and S. A. Kivelson, Phys. Rev. B **85**, 035116

(2012).

[226] S. Raghavan, J. Y. Zhang, O. F. Shoron, and S. Stemmer, Phys. Rev. Lett. **117**, 037602 (2016).

[227] S. S. Saxena, P. Agarwal, K. Ahilan, F. M. Grosche, R. K. W. Haselwimmer, M. J. Steiner, E. Pugh, I. R. Walker, S. R. Julian, P. Monthoux, G. G. Lonzarich, A. Huxley, I. Sheikin, D. Braithwaite, and J. Flouquet, Nature **406**, 587 (2000).

[228] S. Ran, C. Eckberg, Q.-P. Ding, Y. Furukawa, T. Metz, S. R. Saha, I.-L. Liu, M. Zic, H. Kim, J. Paglione, and N. P. Butch, Science **365**, 684 (2019).

[229] E. Bauer and M. Sigrist, editors , *Non-Centrosymmetric Superconductors* (Springer Berlin Heidelberg, Berlin, Heidelberg, 2012).

[230] K. V. Samokhin, Phys. Rev. B **70**, 104521 (2004).

[231] D. F. Agterberg and R. P. Kaur, Phys. Rev. B **75**, 064511 (2007).

[232] T. Sekihara, R. Masutomi, and T. Okamoto, Phys. Rev. Lett. **111**, 057005 (2013).

[233] S. Fujimoto, J. Phys. Soc. Japan **76**, 051008 (2007).

[234] P. A. Frigeri, D. F. Agterberg, A. Koga, and M. Sigrist, Phys. Rev. Lett. **92**, 097001 (2004).

[235] Y. Saito, Y. Nakamura, M. S. Bahramy, Y. Kohama, J. Ye, Y. Kasahara, Y. Nakagawa, M. Onga, M. Tokunaga, T. Nojima, Y. Yanase, and Y. Iwasa, Nat. Phys. **12**, 144 (2016).

[236] V. Kozii and L. Fu, Phys. Rev. Lett. **115**, 207002 (2015).

[237] L. Fu, Phys. Rev. Lett. **115**, 026401 (2015).

[238] L. Fu and C. L. Kane, Phys. Rev. Lett. **100**, 096407 (2008).

[239] A. Y. Kitaev, Ann. Phys. (N. Y). **303**, 2 (2003).

[240] R. Wakatsuki and N. Nagaosa, Phys. Rev. Lett. **121**, 026601 (2018).

[241] S. Hoshino, R. Wakatsuki, K. Hamamoto, and N. Nagaosa, Phys. Rev. B **98**, 054510 (2018).

[242] S. Kanasugi and Y. Yanase, Phys. Rev. B **100**, 094504 (2019).

[243] B. Jalan, S. J. Allen, G. E. Beltz, P. Moetakef, and S. Stemmer, Appl. Phys. Lett. **98**, 132102 (2011).

[244] A. Ohtomo and H. Y. Hwang, Appl. Phys. Lett. **84**, 1716 (2004).

[245] M. D. Glinchuk and I. V. Kondakova, Phys. Status Solidi **174**, 193 (1992).

[246] J. Wang, L. Yang, C. W. Rischau, Z. Xu, Z. Ren, T. Lorenz, J. Hemberger, X. Lin, and K. Behnia, (2019).

[247] D. Olaya, F. Pan, C. T. Rogers, and J. C. Price, Appl. Phys. Lett. **84**, 4020 (2004).

[248] M. Sato, Y. Takahashi, and S. Fujimoto, Phys. Rev. Lett. **103**, 020401 (2009).

[249] M. Sato, Y. Takahashi, and S. Fujimoto, Phys. Rev. B **82**, 134521 (2010).